Departamento de Materia Condensada
Instituto de Ciencia de Materiales de Madrid
Consejo Superior de Investigaciones Científicas

Decoherence phenomena in quantum dot arrays and fractional Josephson effect

Fernando Domínguez Tijero

Departamento de Materia Condensada
Facultad de Ciencias
Universidad Autónoma de Madrid

Departamento de Materia Condensada
Instituto de Ciencia de Materiales de Madrid
Consejo Superior de Investigaciones Científicas

Decoherence phenomena in quantum dot arrays and fractional Josephson effect

Fernando Domínguez Tijero

Director: Prof. Gloria Platero Coello
Tutor: Prof. Juan José Sáenz Guitiérrez

Memoria presentada para acceder al grado de Doctor
Departamento de Materia Condensada
Facultad de Ciencias
Universidad Autónoma de Madrid

Madrid, 2012

Resumen

Esta tesis se encuadra en la rama teórica de la la materia condensada. Se ha estudiado el transporte de carga a través de sistemas mesoscópicos construidos en heteroestructuras semiconductoras a bajas temperaturas. Contiene dos partes claramente diferenciadas. En la primera se estudia el transporte de carga a través de dobles y triples puntos cuánticos influenciado por las interacciones con el entorno. Y en la segunda se ha estudiado la estabilidad del experimento de Shapiro conducido por corriente en presencia de fermiones de Majorana.

A continuación pasamos a describir rápidamente tanto los sistemas estudiados así como los principales resultados de nuestra investigación.

El rápido desarrollo de la tecnología ha permitido reducir el tamaño de los bits hasta el orden de unos pocos nanometros. Cuando se reduce hasta tal punto la escala del sistema y la temperatura del mismo, los efectos cuánticos empiezan a tomar importancia. Los puntos cuánticos son un claro ejemplo de ello. En estos sistemas se ha observado su naturaleza discreta así como la importancia de efectos puramente cuánticos como el de la coherencia.

Desde la fabricación del primer gas de electrones bidimensional en los años 80 hasta nuestros días, se ha llegado a un control de sistemas cada vez mś complejos. Todo ello ha hecho que tengamos el privilegio de asistir a una época donde teorías como la del fermión de Majorana, entre otras, sean investigadas en el laboratorio.

En la primera parte de esta tesis se presentan los resultados del estudio de transporte en dobles (capítulo 5) y triples (capítulos 3 y 4) puntos cuánticos. En general nos interesará estudiar el transporte en sistemas donde existan estados que no conduzcan la corriente o que la interrumpan momentaneamente por efectos coherentes. En esta situación el electrón pasará más tiempo en el los puntos cuánticos, con lo que empezará a interactuar con el entorno. De este modo perderá la coherencia en un fenómeno llamado decoherencia. Este proceso desbloquea la corriente y por lo tanto hace posible el estudio de una forma indirecta de la decoherencia de los sistemas.

En el capítulo 3 se estudia la corriente y el ruido a través de un triple punto cuántico cuando uno de los niveles energéticos está fuera de resonancia. Hemos obtenido que a pesar de no afectar a la corriente, la desviación de esta alrededor de su valor medio es afectada cuadráticamente con la diferencia de energía respecto del nivel sacado fuera de resonancia. Hemos explicado analíticamente este proceso y además hemos conseguido estimar de forma cualitativa los

En el capítulo 4 hemos estudiado la corriente en un triple punto cuántico cuando todos los niveles de los puntos cuánticos están en resonancia. En esta situación los fenómenos de interferencia son relevantes y se llega al llamado estado oscuro, que bloquea la corriente por un fenómeno de interferencia destructiva. En esta situación hemos hecho interaccionar al electrón con un modo fonónico amortiguado. Como resultado se destruye la coherencia y da lugar al paso de corriente. Hemos obtenido el resultado analítico de la corriente y una explicación del mecanismo de decoherencia.

En el capítulo 5 hemos obtenido la probabilidad de volteo de espín mediada por la interacción

hiperfina y por fonones. Esta probabilidad es de gran importancia en el bloqueo de espín ya que da lugar a la corriente, y como en el caso anterior, el conocimiento de este rate permite estudiar la evolución de la corriente. Hemos hecho incapie en la diferencia que supone considerar la interacción hiperfina como un campo magnético efectivo, y por ello mostramos un esquema simple de medida que permite dar una explicación intuitiva.

En la segunda parte de esta tesis, en los capítulos 6 y 7, se trata el análisis numérico de un experimento que prueba la existencia de los fermiones de Majorana, esto es, el experimento de los escalones de Shapiro. La existencia de los fermiones de Majorana cambia la periodicidad de la unión de una tipo 2π a una 4π dando lugar a lo que se conoce con el nombre de efecto Josephson fraccionario. El experimento de Shapiro da una relación entre la fase y la corriente, con lo que permite deducir la periodicidad de la unión. En estos capítulos damos una pequea introducción al tema emergente y dejamos el capítulo 7 para la explicación de nuestros resultados. Demostramos que el experimento es robusto en presencia de niveles normales de Andreev y envenenamiento de cuasipartícula. Y describimos en qué regimenes y el por qué se muestra estable.

Part I

Transport through quantum dots

Chapter 1

Introduction to quantum dots

1.1 Introduction

The beauty of quantum dots lies on the fact that they provide us with a solid platform for experimentally study the physics of few-electron systems with a high degree of control, allowing not only to test fundamental properties of quantum mechanics but also propose applications for future technological devices.

Quantum dots are structures that confine electrons to nano-scale regions in a solid-state material [91, 66].Due to the strong confinement of electrons in all three directions, their energy spectrum is discrete in analogy to real to atoms. As a consequence the underlying physics of quantum dots, also known as "artificial atoms" [82], is very similar to that of the real ones. In contrast to real atoms, in quantum dots it is possible to tune the system parameters by attaching electrical gates and sources/drain contacts to the system, which allows to explore regimes that are not accessible for atoms [53, 145].

By confining single electrons, one naturally defines a two-level system out of the spin-up and spin-down component of the electron spin. It seems logical to extend this analogy to larger systems and couple two or more quantum dots in an array. From a theoretical perspective, molecular wires share many features with quantum dots. In particular, the electronic structure of both systems consists of discrete states. Owing to this fact, coherently coupled quantum dots may be considered as "artificial molecules", despite the fact that their energy scales are several orders of magnitude smaller than those of real molecules.

For roughly one decade, the state of the art has been to couple just two quantum dots coherently [161, 11],while triple quantum dots have been realized only recently [144, 56, 133]. such as superpositions of states or interference can be observed in arranges of more than one QD. Both double quantum dots [61] and triple quantum dots [56, 133] can be constructed such that electrons coming from the source may proceed on two different paths towards the drain. There they interfere constructively or destructively, depending on the setup and a possible flux enclosed by the interfering paths.

As electronic devices have decreased dramatically in size over the last decades and seemingly continue to do so the study of quantum dots has pass from a pure physicist curiosity to a potential technological tool. It is highly likely that quantum dots will form an important building block in future nano-scale electronics with applications in digital and analog circuitry, metrological standards, sensors, light-emitting diodes (LEDs) and also quantum information processing.Understanding the physics of quantum dots is consequently an important scientific task with promising applications in future technolo-

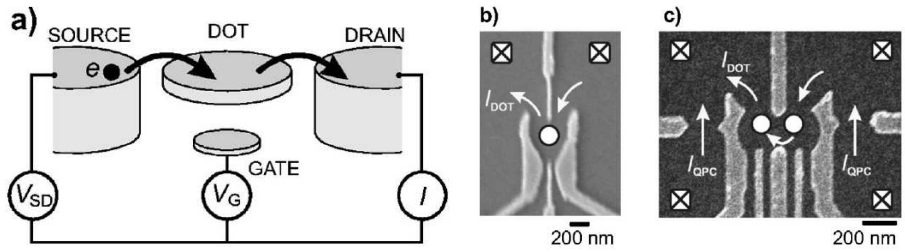

Fig. 1.1: a) Schematic representation of a lateral quantum dot defined in a 2DEG. Depleted region in white, negative voltages applied to metal gate electrodes in dark gray. Ohmic contacts (light gray columns) to the 2DEG reservoirs. Figure taken from ref. [66]. b) and c) Scanning electron micrograph of a lateral few-electron single and double quantum dot respectively. The white dot indicates the location of the QD, and the white squares display Ohmic contact. d) Schematic diagram of a vertical quantum dot, where the dot is located between the two AlGaAs tunnel barriers. The dashed curves indicate that a negative voltage applied to the side gate effectively reduces the diameter of the dot by squeezing it.

gies.

Here I give a general review about the experimental set up of quantum dots and briefly discuss some interesting properties found experimentally, which confirm previous theoretical predictions.

1.2 Quantum dots (QD)

There are different kinds of quantum dots, depending on the size, material and technic used in their fabrication. One can find lateral or vertical gate-defined quantum dots and self-assembled quantum dots. Gate-defined quantum dots consist of a electrostatic, confining potential, created by metallic gate electrodes, in which electrons can be trapped. Typically, the gate electrodes are fabricated using electron-beam lithography on top of a heterostructure with a two-dimensional electron gas (2DEG) trapped at the interface between two semiconductor materials [91, 92, 121, 90, 68], e.g., GaAs and AlGaAs. More recently, quantum dots have been defined along semiconductor nanowires [10, 41, 65, 149] or carbon nanotubes [142, 131] by placing them across grids of metallic gate electrodes.

The typical values of the $2D$ electron density are $n_s \sim (1-5) \times 10^{15} m^{-2}$ [92], this implies that the Fermi energy $\lambda_f = (2\pi/n_s)$ is roughly 100 times larger than in metals. The size of the quantum dot is roughly determined by the spacing between the gate-electrodes, which is typically on the order of a few hundred nanometers, small enough to contain just a few (0,1,2,...) electrons. This length is about three orders of magnitude smaller than the electron mean free path [92]. The quantum dot is connected to two external leads, source and drain, by a tunnel junction. These leads connect the dot to macroscopic voltage and current meters. A third terminal provides an electrostatic or capacitive coupling and can be used as a gate electrode. See Figure 1.1

Since the voltages applied to the gate electrodes are experimentally controllable, gate-defined quantum dots allow for a high degree of tunability of tunnel barriers, occupation numbers, etc. The difference between lateral and vertical quantum dost is that in lateral quantum dots the current through the quantum dot flows in the 2DEG plane to which the electrons are confined. While in vertical quantum dot, the current flows in the direction perpendicular to the plane. The pillar where the vertical quantum dot is confined (see Fig. 1.1 c)), is etched from a semiconductor double-barrier heterostructure.

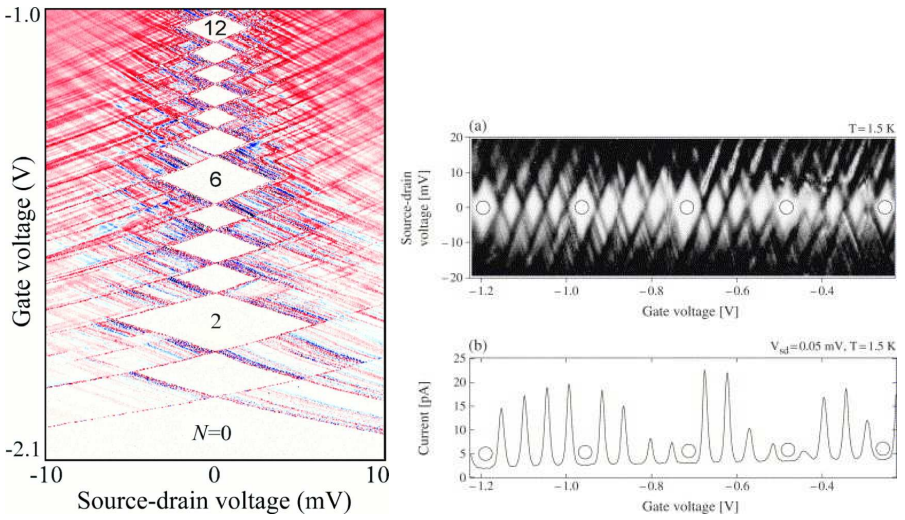

Fig. 1.2: a)Measured Coulomb oscillations as a function of gate voltage for different temperatures. Figure taken from ref. [58]. b)Coulomb Blockade in quantum dots. In the white regions transport is blockated due to intradot Coulomb repulsion, The number inside the diamonds denote the number electrons inside the quantum dot for each configuration. Figure taken form ref [92] c)Coulomb blockade diamonds in a graphene quantum dot.

Self-assembled quantum dots provide a complementary approach to confinement of charges in the solid-state.They form spontaneously in the process of epitaxial growth. They have favorable properties for electronic and optoelectronic device applications, are, however, not so well controllable with regard to placing gate electrodes. All calculations done in this thesis are assumed to be valid for lateral few electron quantum dots. And so we will not describe self-assembled quantum dots in more detail here. For a short introduction, see ref. [120]

1.3 Charge Transport in QD

The small size of the QD implies that the transport through the device is ballistic. This and their large Fermi energy (compared to the one of metals) make these systems suitable for studying quantum transport. Particle exchange in QD can occur with only on of the two leads, it can be either form the source to the dot or from the dot to the drain. If there is no coupling to the source and drain contacts, the quantum dot act as an island for electrons. The number of electrons in this island is and integer number N and the charge is Ne. If now tunneling is allowed the charge of the dot increases by e, associated with the charge increment there is an energy increment in the dot. In a single quantum dot the chemical potential of the dot when the number of electrons is changed by one is

$$\mu N + 1 - \mu N = \Delta E + U, \tag{1.1}$$

where ΔE is the quantum mechanical level spacing and U the charging energy, the energy cost one has to pay in order to overcome the Coulomb repulsion between the electrons on the dot when adding an extra electron. This is true as long as: the tunneling barriers are opaque enough, such that the number of electrons in the dot is well defined. And $K_B T < \Delta E$, the temperature should be small enough such

that the charging energy becomes the relevant energy scale. If for fixed gate voltage the left and right chemical potentials of source (μS) and drain (μD) are such that the chemical potential of the dot is higher in energy than the source, no electron can tunnel through the dot and current is said to be blocked by Coulomb blockade. Increasing the gate voltage lowers the energy levels in the dots, therefore the current measured as a function of the gate voltage for fixed source/drain bias oscillates with a peak spacing that is directly proportional to the addition energy $\Delta E + U$, see Fig. 1.3. The theory of Coulomb blockade oscillations has been studied in detail by Glazman et al. Averin et al. and Beenakker

1.3.1 Spin blockade regime

Due to the quantum nature of the particles inside the dot one can can naturally expect that the spin play an important role in the electron transport. The spin counter part to Coulomb blockade in single quantum dots is the so called "spin blockade" that occurs in double quantum dots. It occurs when transport is blocked due to Pauli's exclusion principle. Consider a double quantum dot in which one electron is confined electrostatically in the dot connected to the drain. A finite current is only measured when an electron can tunnel to the right dot onto a level of double occupation, and subsequently to the drain. Note that this two-electron level has singlet character, i.e. only two electrons with different spin can occupy it. The two-electron excited level with triplet character is much higher in energy and not accessible at this configuration of gate voltages. Tunneling processes in quantum dot arrays conserve the electron spin and hence and electron in the left lead can only tunnel to the right dot, the one connected to the drain if and only if the electron on the right dot has an opposite spin to the one tunneling from the left dot. if the two electrons. If both electrons have the same spin tunneling to the right dot is suppressed. This state blocks the current which then drops to zero. Spin-blockade in quantum dot arrays was theoretically predicted in 1995 by Weinmann et al. and proposed as a spectroscopic tool by Ciorga et al. The first experimental observation of spin blockade in few-electron quantum dots was achieved by Ono et al.

1.3.2 Kondo effect

Under certain conditions a non zero total spin can enhance the transport through the dot. Such is the case of the Kondo effect. For an odd number of electrons trapped in the dot the total spin is non zero and has a minimum value $S = 1/2$. This dot found between large seas of free electrons in the two leads can them take the role of impurity.

When the dot is coupled to a metallic conduction band, at low temperatures the conduction electrons can scatter off the dot via a virtual process, as that observed in Figure (1.3a). The virtual process can take place at low temperatures $T < T_K$ (T_k is the Kondo temperature) where the interaction between the free electrons and the impurity is non perturbative. This effect is completely analogous to the more traditional case of a magnetic impurity in a metal.

The main difference between a quantum dot and a real metal is that, in a metal, the electron states are plane waves, and scattering from impurities in the metal mixes electron waves with different momenta. This momentum transfer increases the resistance. In a quantum dot, however, all the electrons have to travel through the device, as there is no electrical path around it. In this case, the Kondo resonance makes it easier for states belonging to the two opposite electrodes to mix. This mixing increases the conductance (i.e. decreases the resistance). In other words, the Kondo effect produces the opposite behavior in a quantum dot to that of a bulk metal. Kondo effect in quantum dots was first predicted by 1988 More recently the Kondo effect has been observed in quantum dot systems

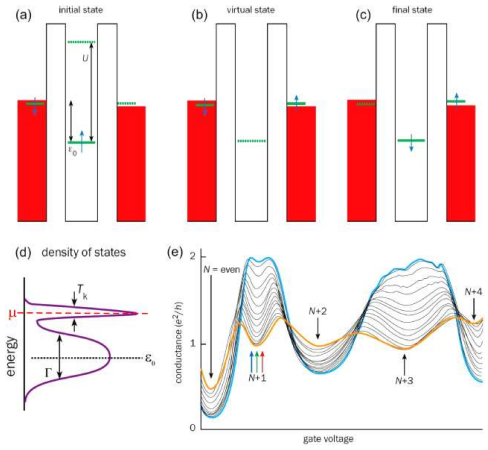

Fig. 1.3: a) schematic representation of a Kondo spin-flip process. b)The conductance (y-axis) as a function of the gate voltage, which changes the number of electrons, N, confined in a quantum dot. When an even number of electrons is trapped, the conductance decreases as the temperature is lowered from 1 K (orange) to 25 mK (light blue). This behaviour illustrates that there is no Kondo effect when N is even. The opposite temperature dependence is observed for an odd number of electrons, i.e. when there is a Kondo effect. c)The conductance for N+1 electrons as a function of temperature divided by the respective Kondo temperature , the Kondo temperature, TK, for the different gate voltages can be calculated by fitting the theory to the data. Figures taken form [91]

From the effects described above one can see that the transport through quantum dots is governed by the electron charge and by the electron's spin in the dots. As mentioned above constructive or destructive interference can be observed in specific set ups in double and triple quantum dots. Moreover it is possible to observe superpositions of states that are decoupled from the drain and, thus, block the electron transport [110, 126] creating dark states. This property is intrinsic to three-level systems, called coherent population trapping. In triple quantum dots it can be seen in a triangular configuration. The device is biased from left to right, and the Coulomb blockade regime is assumed, such that only one excess electron can be in the triple-dot-system at any one time Essentially, interference between electron paths through the upper and lower dots leads to a state in which the electron wave function destructively interferes at the dot coupled to the collector. They can also be achieve in double QD driving three-level double dots with bichromatic ac electric fields. Such blockade may be resolved by excitations with proper ac fields which also create spin correlations between transported electrons This state is analogous to the dark state observed in quantum optics in three-level atoms excited by two resonant laser fields In these systems, the electronic wave function evolves towards an eigenstate superposition, a so-called dark state, which is decoupled from the laser fields and therefore manifests as an antiresonance in the emission spectrum.

From a theoretical perspective, molecular wires share many features with quantum dots. In particular, the electronic structure of both systems consists of discrete states. Owing to this fact, coherently coupled quantum dots may be considered as "artificial molecules", despite the fact that their energy scales are several orders of magnitude smaller than those of real molecules. For roughly one decade, the state of the art has been to couple just two quantum dots coherently [161, 11, 162], while triple quantum dots have been realized only recently [144, 56, 133]. Both double quantum dots [61] and triple

quantum dots [56, 133] can be constructed such that electrons coming from the source may proceed on two different paths towards the drain. There they interfere constructively or destructively, depending on the setup and a possible flux enclosed by the interfering paths. Moreover, there exist dark states which are superpositions of states that are decoupled from the drain and, thus, block the electron transport [110, 126]. Such blockade may be resolved by excitations with proper ac fields [140, 19] which also create spin correlations between transported electrons [141].

Chapter 2

Mathematical background

Summary

In this chapter we introduce the physical and mathematical background used in the first part of this thesis, which consists on the study of electron transport through double and triple quantum dots. In essence, we introduce the density matrix formalism to describe the evolution of an open quantum system, that is a quantum system coupled to (a) system(s) of several degrees of freedom, which we shall call the baths We introduce also current, shot-noise and higher order correlation functions.

2.1 Density matrix formalism and the Born-Markov master equation

In order to study the evolution of complex systems, physicists use simple models to capture the essential features of their behavior. Loosely speaking, these models represent the evolution of quantum systems with few degrees of freedom, coupled to systems with many degrees of freedom, so-called "baths". Due to the impossible mission of describing and solving the dynamics of the coupled system in an exact quantum mechanical way, one can imagine how convenient is the introducion of statistical methods. For this reason we abandom the description of the whole system by means of a wave function and introduce the density matrix of the system. This formalism can describe the effects of the bath in the evolution of the reduced quantum system under several approximations. Here we give a brief description of the formalism and we explain the approximations used implicitely in our equations.

The equation which describes the evolution of the density matrix is given by the Liouville-von Neumann equation

$$\frac{d}{dt}\rho(t) = -i\,[H, \rho(t)] \tag{2.1}$$

beeing $H = H_0 + H_B + V$ the Hamiltonian of the subsystems and interaction respectively. We can always write the interaction Hamiltonian as $V = A \otimes B$, being A and B the Hamiltonians acting on the system and the bath spaces respectively. In the interaction picture yields

$$\frac{d}{dt}\tilde{\rho}(t) = -i\,[V(t), \tilde{\rho}(t)] \tag{2.2}$$

being $\tilde{\rho}$ and $V(t)$, the respective operators in the interaction picture. This equation can be written in an integral form as

$$\tilde{\rho}(t) = \tilde{\rho}(0) - i\int_0^t ds\,[V(s), \tilde{\rho}(s)]\,. \tag{2.3}$$

Then insterting eq. (2.3) into eq. (2.2) and taking the trace of the bath, we then obtain

$$\frac{d}{dt}\tilde{\rho}(t) = -\int_0^t ds tr_B\,[V(t), [V(s), \tilde{\rho}(s)]]\,. \tag{2.4}$$

where tr_B indicates the trace over the bath degrees of freedom, and we have assumed that the average of the interaction $\langle B\rangle = 0$. This assumption can be always forced by redefining $H_0' = H_0 + \langle V\rangle$ and $\langle V\rangle$. Until this moment the equation describing the evolution of the system is still exact and therefore numerically intractable. We now perform some approximations. In first place we will assume that the interaction of the system and the bath is weak, so that its effect on the bath density matrix is negligible, and thus we can write the density matrix as a direct product $\rho(t) \approx \rho_S(t) \otimes \rho_B$. This approximation is known as **Born approximation** and is the responsible for the irreversible dynamics. It is worthy to note that ρ_B contains, in principle, excitations of the bath provoked by the interaction with the system. However, these excitations decay in a timescale much shorter than the considered in the approximation presented below.

Although the equation is now simplified, we still have an integro-differential equation, and therefore we need to simplify further the equation. One can consider the fact that the evolution of $\tilde{\rho}_S(t)$, just depends on the present state, and therefore one makes the replacement $\tilde{\rho}_S(s) \to \tilde{\rho}_S(t)$ and extend the upper limit integral up to infinity. This is justified when τ_R, the timescale over which the th eseate of the system varies appreciablyis large compared to the time scale τ_B over which the state of the reservoir correlation functions decay. This approximation is known as the **Markov approximation** and yields

$$\frac{d}{dt}\tilde{\rho}(t) = -\int_0^\infty ds tr_B\,[V(t), [V(s), \tilde{\rho}_S(t) \otimes \rho_B]]\,. \tag{2.5}$$

This equation will be of capital importance in the development of this thesis. Inserting the Hamiltonians of the leads and dots, one arrives easily to the Markovian master equation, see the result below.

2.1.1 Master equation used in this thesis

2.1.2 Dot-lead Hamiltonian

We consider a triple quantum dot with a ring-shaped geometry as depicted in Fig. 4.2, which is described by the Hamiltonian

$$H_{\mathrm{TQD}} = \sum_i \epsilon_i c_i^\dagger c_i + \tau \sum_{i,j<i} (c_i^\dagger c_j + c_j c_i^\dagger) + U \sum_{i,j<i} c_i^\dagger c_i c_j^\dagger c_j, \tag{2.6}$$

where $i, j = 1, 2, 3$ label the dots, while $c_i^\dagger$ and c_i denote the corresponding creation and annihilation operator of a spinless electron. The first term refers to the onsite energy ϵ_i of an electron on dot i, for which we assume that $\epsilon_1 = \epsilon_3 = 0$, while $\epsilon_2 = eV_{\mathrm{gate}}$ can be tuned by a gate voltage. The second termdescribes electron tunneling between the dots, for which we assume that the tunnel matrix element τ is the same for all three possible transitions. The last contribution models inter-dot Coulomb repulsion with strength U. In the present case, this term can be written in the form $\frac{1}{2}UN(N-1)$, where N denotes

the total number of electrons on the three dots. We assume that the intra-dot interaction is practically infinite, which corresponds to modeling each dot by a spinless single level.

Dots 1 and 3 are attached to electron reservoirs with chemical potentials $\mu_{\rm L}$ and $\mu_{\rm R}$ such that the bias voltage fulfills $eV = \mu_{\rm L} - \mu_{\rm R}$. They are described by the lead Hamiltonian

$$H_{\rm leads} = \sum_{\ell,q} \epsilon_q c^\dagger_{\ell q} c_{\ell q}, \tag{2.7}$$

where $\ell = {\rm L}, {\rm R}$, and the expectation value $\langle c^\dagger_{\ell q} c_{\ell' q'}\rangle = f(\epsilon_q - \mu_\ell)\delta_{\ell\ell'}\delta_{qq'} \equiv f_\ell(\epsilon_q)\delta_{\ell\ell'}\delta_{qq'}$ with chemical potential μ_ℓ and the Fermi function $f(x) = [\exp(x/k_BT)+1]^{-1}$. The dot-lead contact is established by the tunnel Hamiltonian

$$H_{\rm tun} = \sum_q (V_{{\rm L}q} c^\dagger_{{\rm L}q} c_1 + V_{{\rm R}q} c^\dagger_{{\rm R}q} c_3) + {\rm h.c.} \tag{2.8}$$

We assume within a wide-band limit that all effective coupling strengths $\Gamma_\ell(\epsilon) = 2\pi \sum_q |V_{\ell q}|^2 \delta(\epsilon - \epsilon_q)$ are energy independent and that the setup is symmetric such that $\Gamma_{\rm L} = \Gamma_{\rm R} = \Gamma$.

The derivation of a master equation starts from the Liouville-von Neumann equation for the full density operator, ${\rm i}\hbar\dot{R} = [H_{\rm TQD} + H_{\rm tun} + H_{\rm leads}, R]$. By standard techniques [12], one obtains for the reduced density operator of the central system, $\rho = {\rm tr}_{\rm leads} R$, within second-order perturbation theory the Bloch-Redfield equation

$$\begin{aligned}\dot\rho &= -\frac{\rm i}{\hbar}[H_{\rm TQD}, \rho] - \frac{1}{\hbar^2}{\rm tr}_{\rm leads}\int_0^\infty dt' [H_{\rm tun}, [\tilde H_{\rm tun}(-t'), R]] \\ &\equiv \mathcal{L}\rho,\end{aligned} \tag{2.9}$$

which can be evaluated under the factorization assumption $R = \rho_{\rm leads,0} \otimes \rho$. The tilde denotes the interaction picture with respect to the uncoupled Hamiltonian, $\tilde X(t) = U_0^\dagger(t) X U_0(t)$, where $U_0(t) = \exp\{-{\rm i}(H_{\rm TQD} + H_{\rm leads})t/\hbar\}$. We proceed by inserting the dot-lead tunnel Hamiltonian (2.8) and evaluate the trace over the lead states. In order to cope with the interaction picture, we decompose the resulting master equation into the eigenstates $|\alpha\rangle$ of $H_{\rm TQD}$, where E_α denotes the corresponding eigenenergy. This allows us to evaluate the τ-integration, which yields a delta function and a principal value term. Neglecting the latter, we obtain for the density matrix elements the equation of motion

$$\dot\rho_{\alpha\beta} = -\frac{\rm i}{\hbar}(E_\alpha - E_\beta)\rho_{\alpha\beta} + \sum_{\alpha',\beta'} \mathcal{L}_{\alpha\beta,\alpha'\beta'}\rho_{\alpha'\beta'} \tag{2.10}$$

with the incoherent dot-lead tunneling given by

$$\begin{aligned}\mathcal{L}_{\alpha\beta,\alpha'\beta'} \quad &= \sum_{\ell=1,3}\frac{\Gamma_\ell}{2}\Big\{\langle\alpha|c^\dagger_\ell|\alpha'\rangle\langle\beta'|c_\ell|\beta\rangle f_\ell(E_\alpha - E_{\alpha'}) + \langle\alpha|c^\dagger_\ell|\alpha'\rangle\langle\beta'|c_\ell|\beta\rangle f_\ell(E_\beta - E_{\beta'}) \\ &\quad - \sum_\gamma \langle\beta'|c_\ell|\gamma\rangle\langle\gamma|c^\dagger_\ell|\beta\rangle f_\ell(E_\gamma - E_{\beta'})\delta_{\alpha\alpha'} - \sum_\gamma \langle\alpha|c_\ell|\gamma\rangle\langle\gamma|c^\dagger_\ell|\alpha'\rangle f_\ell(E_\gamma - E_{\alpha'})\delta_{\beta\beta'}\Big\} \\ &\quad + (c_\ell, c^\dagger_\ell, f_\ell) \to (c^\dagger_\ell, c_\ell, 1 - f_\ell),\end{aligned} \tag{2.11}$$

where the leads now are labeled by the number ℓ of the dot to which they are attached. Electron tunneling from the leads to the dots is described by the explicitly written terms, while the replacement in the last line yields the terms for tunneling from the dots to the leads.

The solution of the master equation (2.10) contains the full information about the state of the central system and provides all corresponding expectation values. However, we are interested in the

statistics of the charge transported after the initial preparation, which is an expectation value of lead operators. Therefore we have to generalize the master equation formalism by introducing a counting variable which allows one to keep track of this information.

2.1.3 Full-counting statistics

The counting variable χ is defined via the moment generating function

$$\phi(\chi,t) = \langle \exp(i\chi N_{\mathrm{R}})\rangle_t \,, \tag{2.12}$$

where $N_{\mathrm{R}} = \sum_q c_{3q}^\dagger c_{3q}$ is the electron number operator of the right lead, while the angular brackets refer to the expectation value at time t. The kth derivative of $\phi(\chi,t)$ with respect to iχ at $\chi = 0$ obviously is the moment $\langle N_{\mathrm{R}}^k\rangle$ of the electron distribution in the right lead. The cumulants of the distribution are defined as the corresponding derivatives of $\ln\phi(\chi,t)$. For a Markov process, they eventually become linear in time. Their time-derivatives at large times,

$$C_k = \frac{\partial}{\partial t}\frac{\partial^k}{\partial(i\chi)^k}\ln\phi(\chi,t)\Big|_{\chi=0,t\to\infty} \tag{2.13}$$

are the stationary current cumulants and characterize the transport. The first and the second cumulant, C_1 and C_2, are essentially the current $I = eC_1$ and its zero-frequency noise $S = e^2C_2$, respectively. Their ratio, the Fano factor $F = C_2/C_1$, represents a dimensionless measure for the noise of the transport process [40]. It is defined such that for a Poissonian process $F = 1$.

Our goal is now to find a reduced master equation that allows one to compute $\phi(\chi,t)$. We start again from the full density operator R, but now multiply it with the operator $\exp(i\chi N_{\mathrm{R}})$ before tracing out the leads. This yields the generalized reduced density operator $P(\chi,t) = \mathrm{tr}_{\mathrm{leads}}\{\exp(i\chi N_{\mathrm{R}})R\}$ which contains information about the electron distribution of the drain and fulfills the trace condition $\mathrm{tr}P = \phi$. Using the commutation relations $[N_{\mathrm{R}},\Lambda] = \Lambda$ and $[N_{\mathrm{R}},\Lambda^\dagger] = -\Lambda^\dagger$, where $\Lambda = \sum_q V_q c_3^\dagger c_{3q}$, we obtain the master equation

$$\dot P(\chi,t) = \mathcal{L}_\chi P(\chi,t) \tag{2.14}$$

with the augmented Liouvillian

$$\mathcal{L}_\chi = \mathcal{L} + (\mathrm{e}^{i\chi}-1)\mathcal{J}^+ + (\mathrm{e}^{-i\chi}-1)\mathcal{J}^- \tag{2.15}$$

and the particle current superoperators $\mathcal{J}^\pm$. After some algebra, we find for the latter the expression [81]

$$\mathcal{J}^-\rho = \frac{e\Gamma_\ell}{2\pi}\int_0^\infty dt' \int d\epsilon\, \mathrm{e}^{-i\epsilon t'}\tilde c_3^\dagger(-t')\rho c_3 f_\ell(\epsilon) + \mathrm{h.c.}, \tag{2.16}$$

and $\mathcal{J}^+$ is formally obtained from $\mathcal{J}^-$ by the replacement $(c_3^\dagger, c_3, f_{\mathrm{R}}) \to (c_3, c_3^\dagger, 1-f_{\mathrm{R}})$. The superoperator $\mathcal{J}^+$ describes tunneling from dot 3 to the right lead, while $\mathcal{J}^-$ corresponds to the reversed process. We proceed as for the derivation of the master equation (2.10) and decompose the current superoperators into the eigenstates of H_{TQD} which yields

$$\begin{aligned}
\mathcal{J}^+_{\alpha\beta,\alpha'\beta'} &= \frac{\Gamma_{\mathrm{R}}}{2}\langle\alpha|c_3|\alpha'\rangle\langle\alpha'|c_3^\dagger|\beta\rangle\big\{2 - f_{\mathrm{R}}(E_\alpha - E_{\alpha'}) - f_{\mathrm{R}}(E_\beta - E_{\beta'})\big\}, \\
\mathcal{J}^-_{\alpha\beta,\alpha'\beta'} &= \frac{\Gamma_{\mathrm{R}}}{2}\langle\alpha|c_3^\dagger|\alpha'\rangle\langle\alpha'|c_3|\beta\rangle\big\{f_{\mathrm{R}}(E_\alpha - E_{\alpha'}) + f_{\mathrm{R}}(E_\beta - E_{\beta'})\big\}.
\end{aligned} \tag{2.17}$$

In the long-time limit, the dynamics of $P(\chi,t)$ is governed by the eigenvalue of $\mathcal{L}_\chi$ with the largest real part, denoted as $\lambda(\chi)$. We assume that $\lambda(\chi)$ can be uniquely identified by its limit $\lim_{\chi\to 0}\lambda(\chi)=0$, i.e., it corresponds to the stationary solution of the Liouvillian $\mathcal{L}=\mathcal{L}_{\chi\to 0}$. Then, $P=A(\chi)\exp[\lambda(\chi)t]$, with $A(\chi)$ be the corresponding "eigenoperator" of $\mathcal{L}_\chi$. It is straightforward to see that $\ln\phi(\chi,t)=\ln\mathrm{tr}A(\chi)+\lambda(\chi)t$. In the long-time limit, the contribution of the normalization factor is not relevant and, thus, we can conclude that $\lambda(\chi)$ is the current cumulant generating function [5]. It can be written as the series

$$\lambda(\chi)=\sum_{k=1}^{\infty}\frac{C_k}{k!}(\mathrm{i}\chi)^k. \tag{2.18}$$

The remaining task is now to compute the proper eigenvalue of $\mathcal{L}_\chi$ and its derivatives with respect to χ. In many cases, the reduced density matrix has a sufficiently small dimension or possesses symmetries, such that one can continue with analytical calculations. As soon as one has to resort to a numerical treatment, however, one faces the difficulty of numerically computing derivatives. This can be avoided with the recursive scheme developed in Ref. [48] even for non-Markovian master equations. Here we restrict ourselves to the Markovian limit.

Since we are interested in the derivatives of the cumulant generating function at $\chi=0$, we can treat χ as small parameter and employ perturbation theory. Then the series (2.18) for the eigenvalue $\lambda(\chi)$ corresponds to the usual ansatz for the eigenvalue. It can be computed by the recursion derived in Appendix A.1, see Eqs. (A.6) and (A.7). Upon setting in these expressions $E_k=C_k/k!$, $V_k=[\mathcal{J}^+ +(-1)^k\mathcal{J}^-]/k!$, and $P_k=|\phi_k\rangle/k!$, we find

$$C_k=\sum_{k'=0}^{k-1}\binom{k}{k'}\mathrm{tr}\{\mathcal{J}^+ +(-1)^{k-k'}\mathcal{J}^-\}P_{k'}, \tag{2.19}$$

$$P_k=\frac{\mathcal{Q}}{\mathcal{L}}\sum_{k'=0}^{k-1}\binom{k}{k'}\Big\{C_{k-k'}-[\mathcal{J}^+ +(-1)^{k-k'}\mathcal{J}^-]\Big\}P_{k'}. \tag{2.20}$$

The iteration starts from the stationary solution of the Liouvillian, $P_0=|\phi_0\rangle=\rho_\infty$, which implies $E_0=C_0=0$. Multiplication with the corresponding left eigenvector $\langle\phi_0|$ must correspond to computing the trace. This becomes clear when one notes that the Liouvillian is trace conserving, i.e. $\mathrm{tr}\mathcal{L}X=0$ for any operator X. Consequently, $\mathcal{Q}=(\mathbf{1}-\rho_\infty\mathrm{tr})$ is the projector on the subspace perpendicular to ρ_∞. In this subspace, the Liouvillian possesses the pseudo-inverse $\mathcal{Q}/\mathcal{L}$. Applying it to any operator, i.e. computing $(\mathcal{Q}/\mathcal{L})B\equiv X$, is equivalent to solving the linear equation $\mathcal{L}X=B$ under the constraint $\mathrm{tr}X=0$.

In particular, we obtain for the first two cumulants, which are the current and the zero-frequency noise, the known expressions [49]

$$I=e\mathrm{tr}(\mathcal{J}^+ -\mathcal{J}^-)\rho_\infty \tag{2.21}$$

$$S=e^2\mathrm{tr}(\mathcal{J}^+ +\mathcal{J}^-)\rho_\infty-2e^2\mathrm{tr}(\mathcal{J}^+ -\mathcal{J}^-)\frac{\mathcal{Q}}{\mathcal{L}}(\mathcal{J}^+ -\mathcal{J}^-)\rho_\infty. \tag{2.22}$$

Chapter 3

Electron bunching in triple quantum dot

Summary

In this chapter we investigate the conduction properties of a triple quantum dot in ring configuration as sketched in Fig. 4.2. Along this chapter we will focus on the influence of a gate voltage that allows shifting of the levels of dot 2 out of resonance and we leave the resonant regime for the next chapter. The intuitive expectation is that for strong detuning, the two other dots govern the transport process, such that the triple quantum dot behaves like a double quantum dot. While this is indeed the case for the current, electrons temporarily trapped in dot 2 may cause Coulomb blockade and, thus, interrupt the transport such that the electron flow becomes avalanche-like. This is reflected in the zero-frequency component of the current-current correlation function which significantly exceeds the value for a Poisson process. With this criterion, avalanche-like transport has been predicted for quantum dots coupled to a harmonic mode [49, 88], multi-level quantum dots [8], triple quantum dots in the Kondo regime [165], and also when destructive interference effects strongly suppress the current [160, 159, 103, 143].

3.1 Introduction

During the last decade, a huge effort has been made to understand the conduction properties of quantum systems that consist of only a few discrete levels. Spurred by Feynman's vision of "plenty of room at the bottom" [44], it has e.g. been proposed to use single molecules as elements of future electronic circuits [36]. Although this task is far from being accomplished, molecular electronics already became an established field [63, 28]. Apart from their technological promises, conducting molecules may also serve as tools for the implementation of fundamental physical phenomena. One example is the intriguing effect of tunnel suppression by the purely coherent influence of an ac field [59], which is stable even in the presence of Coulomb repulsion [27]. Coherent destruction of tunneling leaves its fingerprints in the transport characteristics of laser-driven molecular wires, where an ac field may suppress the current and its fluctuations [98, 22, 125, 89].

An established theoretical tool for characterizing such correlated transport is full counting statistics [8, 100, 5] which provides the complete information about the distribution of the transported charge

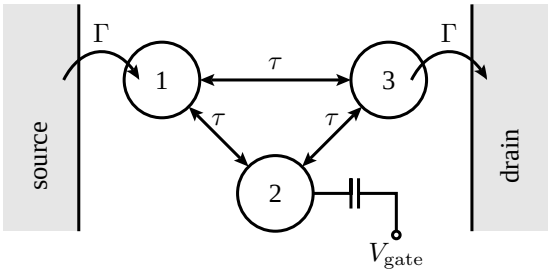

Fig. 3.1: Triple quantum dot in ring configuration coupled to electron source and drain. The onsite energies of dots 1 and 3 are $\epsilon_{1,3} = 0$, while the onsite energy of dot 2 can be tuned by a gate voltage such that $\epsilon_2 = eV_{\mathrm{gate}}$. The bias voltage V is assumed to shift the chemical potentials symmetrically, such that $\mu_{\mathrm{L}} = eV/2 = -\mu_{\mathrm{R}}$.

in terms of the corresponding cumulants. For a Markovian master equation as employed below, it is possible to express these cumulants as derivatives of a particular eigenvalue of the Liouville operator augmented by a counting variable [5]. Generally, this requires the computation of derivatives of high order. As soon as one has to rely on a numerical treatment, practical calculations may represent a formidable task. Recently, Flindt *et al.* have found a way to circumvent this difficulty [48, 47]. Based on Rayleigh-Schrödinger perturbation theory, they derived a scheme that allows one to recursively compute the full counting statistics. We use this approach for our numerical solution.

This chapter is organized as follows. In Section 4.2 we introduce a system-lead Hamiltonian and derive a master equation formalism for the computation of the full counting statistics. The numerical results for the current and the zero-frequency noise, presented in Section 4.3, provide information about the super-Poissonian nature of the transport process. In Section 4.4, we derive for the cumulants up to fourth order analytical expressions valid in the low-bias regime.

3.2 Model and master equation approach

3.3 Numerical observations

An intuitive picture for the transport properties as a function of the gate voltage can be provided for the limiting cases in which the detuning of dot 2 is either much larger or much smaller than the inter-dot tunneling: In the limit $|eV_{\mathrm{gate}}| \ll T$, all three dots are in resonance and, thus, the electrons may take with similar probability two different routes, namely $|1\rangle \to |3\rangle$ and $|1\rangle \to |2\rangle \to |3\rangle$. Therefore one expects interference to be relevant, such that the current can be modified by a magnetic flux penetrating the ring. If the gate voltage is large, by contrast, i.e. for $|eV_{\mathrm{gate}}| \gg T$, dot 2 is off-resonant and, thus, should be of minor relevance. Therefore, the transport properties of the setup are expected to be essentially those of a double quantum dot formed by dots 1 and 3. Our numerical results, however, will demonstrate that this is only true for the average current, while the current noise is significantly altered by the presence of dot 2 even when far detuned.

As a first step, we solve the master equation numerically. In doing so, we identify parameter regimes in which the stationary state of the triple dot is dominated by a few eigenstates. This allows us to reduce the complexity of the master equation, such that we can achieve an analytical treatment that

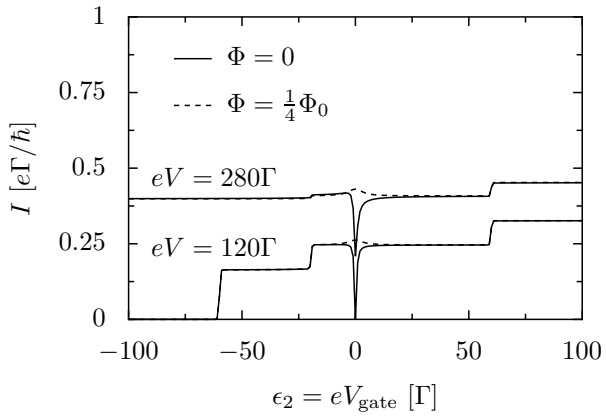

Fig. 3.2: Current as a function of the gate voltage $V_{\rm gate} = \epsilon_2/e$ for different magnetic fluxes Φ and bias voltages. The inter-dot tunnel coupling and interaction are $\tau = 2\Gamma$ and $U = 80\Gamma$, respectively. Inset: Corresponding visibility for $eV = 120\Gamma$.

provides insight to the transport mechanism. For the numerical solution, we use the dot-lead coupling Γ as energy unit. For the typical value $\Gamma = 10\mu$eV, the corresponding current unit reads $e\Gamma/\hbar = 2.43$nA.

3.3.1 Stationary current and occupation probabilities

We focus on the region *without* interference effects. There a main feature of the current is that it exhibits plateaus, see Fig. 3.3(a). This is consistent with the usual Coulomb blockade scenario in which the bias and the gate voltage, determine the maximal number of electrons that can reside on the dots. Accordingly, the probability for having a particular dot occupation changes at the steps, as can be appreciated from Fig. 3.3(b). Moreover, an electron can tunnel from a left lead to the dots only if it has sufficient energy to compensate the Coulomb repulsion of the electrons that are already in the triple quantum dot. Thus the occupation with N electrons ($N = 1, 2, 3$) is possible only if one chemical potential is larger than $(N-1)U$. For the symmetric positive voltage drop assumed herein, the larger chemical potential is $\mu_{\rm L} = eV/2$. This implies that the occupation probability p_N vanishes if $eV < 2(N-1)U$, which is consistent with the occurrence of the steps shown in Fig. 3.3(b). In particular, for $e|V| < 2U$, only single occupation plays a role. Below we will use this fact for establishing an analytical treatment in the low-bias regime.

3.3.2 Shot noise and Fano factor

So far we have seen that unless the bias voltage is extremely low, the current is always of the order $e\Gamma/\hbar$, i.e. changing the gate voltage or the bias voltage modifies the current typically by a factor of the order unity. Figure 3.4 demonstrates that the noise, characterized by the Fano factor $F = S/e|I|$, generally exhibits a more significant dependence on both the bias and the gate voltage.

In the three-electron regime, i.e. for $eV > 4U$, the Fano factor is of order unity and almost independent of ϵ_2. This indicates that the transport process is Poissonian. In the two-electron regime, i.e. for $U < eV/2 < 2U$, the Fano factor [Fig. 3.4(c)] exhibits a quadratic dependence on ϵ_2 as well, but the absolute values are now significantly smaller.

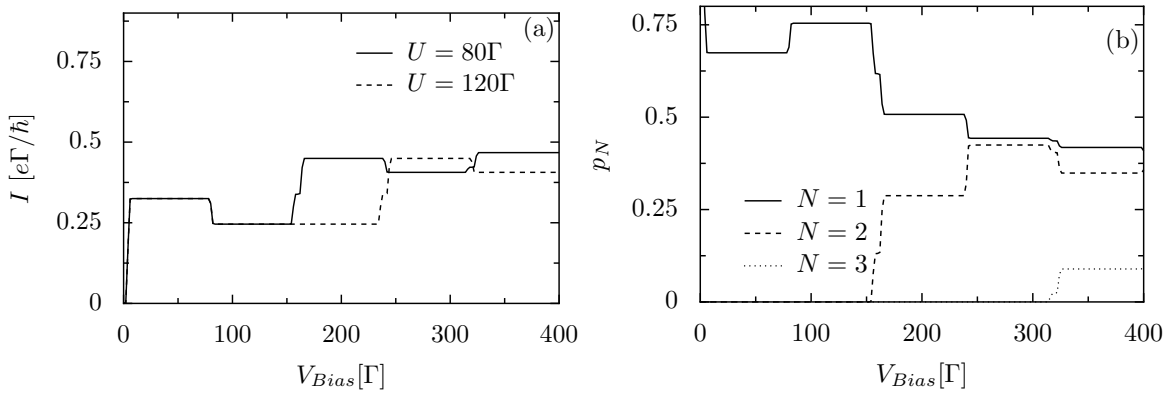

Fig. 3.3: (a) Current as a function of the bias voltage $eV = \mu_{\rm L} - \mu_{\rm R}$ for various interaction strengths. The inter-dot tunnel coupling and the gate voltage are $\tau = 2\Gamma$ and $V_{\rm gate} = \epsilon_2/e = 40\Gamma/e$, respectively. (b) Probability that for $U = 80\Gamma$, the asymptotic state of the triple quantum dot contains N electrons.

A rather pronounced dependence on the gate voltage $V_{\rm gate} = \epsilon_2/e$ is found in that part of the single-electron regime in which the left chemical potential is so large that all single particle levels lie within the voltage window, i.e. for $\epsilon_2 < eV/2 < U$; see Fig. 3.4(b). In particular, we observe a quadratic growth of the Fano factor, $F \propto \epsilon_2^2$, with highly super-Poissonian values. This already indicates electron bunching, where each bunch consists of roughly F electrons [102].

3.3.3 Full counting statistics

A more complete picture can be drawn by considering the distribution function of the transported electrons or equivalently all cumulants, i.e., the full counting statistics. Here we restrict ourselves to the corresponding long-time limit which characterizes the low-frequency fluctuations. For avalanche-like transport, higher-order cumulants were computed [49, 8, 160, 159, 103] and recently also measured [54].

In a simplified picture, one may consider the electron avalanches as particles with charge $q = eF$ that are transported in an uncorrelated manner. For this Poisson process, the cumulants (2.13) grow exponentially fast with their index according to the relation [164]

$$C_k = \left(\frac{q}{e}\right)^{k-1} C_1 = F^{k-1} C_1. \tag{3.1}$$

Closer theoretical investigations of avalanches with finite duration [8, 47], however, indicate that this picture deserves some refinement. In fact there it was found that the cumulants grow even faster. In avalanche diodes, by contrast, the opposite was measured, namely that the cumulants do not grow as fast [54]. But so far the underlying mechanism has not been revealed.

Figure 3.5 depicts the super exponential growth of the C_k in both the one-electron regime and the two-electron regime. The solid line demonstrates that only the cumulants of very low order follow the behavior of the Poisson process underlying Eq. (3.1). Thus, we also in our case observe that already the third cumulant slightly exceeds the value $F^2 C_1$, while higher-order cumulants even assume significantly larger absolute values. It is also interesting to notice that the sign of the cumulants changes periodically with the index k. This hints on the recently conjectured "universal cumulant oscillations" [46].

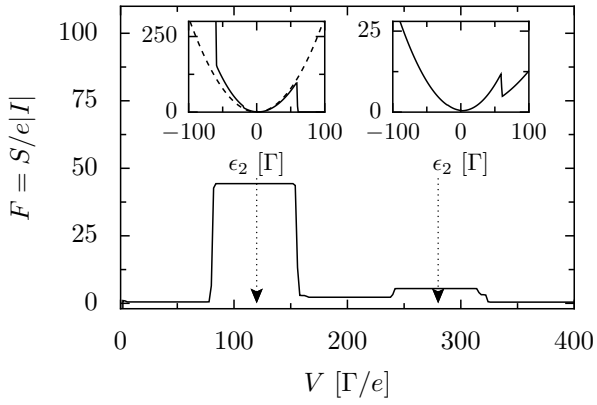

Fig. 3.4: (a) Fano factor of the current shown in Fig. 3.3(a) for the interaction strength $U = 80\Gamma$. (b,c) Fano factor as a function of the detuning $\epsilon_2 = eV_{\rm gate}$ for the bias voltages (b) $V = 120\Gamma/e$ and (c) $V = 280\Gamma/e$. The dashed line in panel (b) represents the analytical result (3.8) valid in the one-electron regime.

3.4 Analytical solution in the one-electron regime

If the bias voltage is so small that only one electron can reside on the triple dot, i.e. for $eV < 2U$, all relevant eigenstates of $H_{\rm TQD}$ are the empty state $|0\rangle$ and the one-electron states. To lowest order in T/ϵ_2, the latter are given in the basis of the localized states $|j\rangle = c_j^\dagger|0\rangle$ by the expressions

$$|\phi_1\rangle = \frac{1}{\sqrt{2}}\left(|1\rangle - |3\rangle\right), \tag{3.2}$$

$$|\phi_2\rangle = \frac{1}{\sqrt{2+4(\tau/\epsilon_2)^2}}\left(|1\rangle - \frac{2\tau}{\epsilon_2}|2\rangle + |3\rangle\right), \tag{3.3}$$

$$|\phi_3\rangle = \frac{1}{\sqrt{1+2(\tau/\epsilon_2)^2}}\left(\frac{\tau}{\epsilon_2}|1\rangle + |2\rangle + \frac{\tau}{\epsilon_2}|3\rangle\right). \tag{3.4}$$

For symmetry reasons, each of these states couples with equal strength to the left and to the right lead, such that the corresponding incoherent transition rates from and to the leads are given by

$$\Gamma_{{\rm L},n} = \Gamma_{{\rm R},n} = \Gamma|\langle\phi_n|3\rangle|^2 \equiv \Gamma_n. \tag{3.5}$$

For the approximate eigenstates (3.2)–(3.4) the coupling constants read $\Gamma_1 = \Gamma_2 = \Gamma/2$ and $\Gamma_3 = \Gamma\tau^2/\epsilon_2^2$.

If the dot-lead coupling Γ is sufficiently small, one can neglect within a rotating-wave approximation off-diagonal elements of the reduced density operator [89], such that the system is well described by the occupation probabilities (P_0, P_1, P_2, P_3) for the eigenstates $|0\rangle$ and $|\phi_n\rangle$, $n = 1, 2, 3$. The corresponding Liouville operator is

$$\mathcal{L}_{1e} = \begin{pmatrix} -\Gamma & \Gamma_1 & \Gamma_2 & \Gamma_3 \\ \Gamma_1 & -\Gamma_1 & 0 & 0 \\ \Gamma_2 & 0 & -\Gamma_2 & 0 \\ \Gamma_3 & 0 & 0 & -\Gamma_3 \end{pmatrix}, \tag{3.6}$$

where the index "1e" refers to the restriction to single occupation. We have assumed that the chemical potentials are such that all three one-electron states lie within the voltage window. Moreover, we have

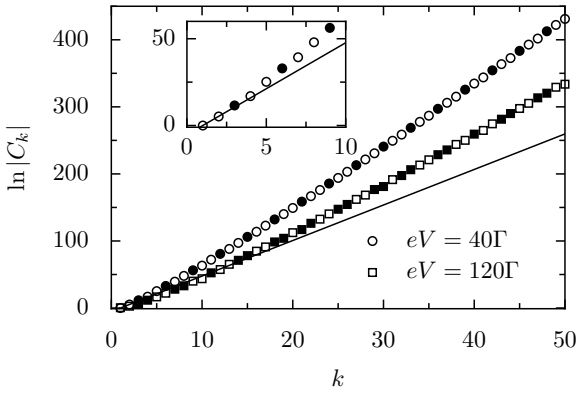

Fig. 3.5: Full counting statistics of the current for $\epsilon_2 = 40\Gamma$ and the bias voltages $V = 120\Gamma/e$ (one-electron regime) and $V = 280\Gamma/e$ (two-electron regime) expressed by the cumulants C_k. All other parameters are as in Fig. 3.4. Open symbols mark positive values while filled symbols correspond to negative values. The line marks the behavior for uncorrelated tunneling of charges $q = eF$ in the one-electron regime (circles), cf. Eq. (3.1). Inset: Enlargement of the lower left corner.

employed the sum rule $\Gamma = \sum_{n=1}^{3} \Gamma_n$ which follows from the completeness relation for the eigenstates $|\phi_n\rangle$ in the one-electron subspace. The corresponding particle current operators are $\mathcal{J}^- = 0$, while $\mathcal{J}^+$ is obtained from $\mathcal{L}_{1e}$ by keeping only the elements placed above the diagonal.

The stationary state of the Liouville operator can now be readily computed and reads $P_0 = 1/4 = P_n$ for all n. Inserting this into the current formula (2.21), yields $I = e\Gamma/4\hbar$. Interestingly enough, the current does not depend on the structure of the eigenstates, which is a consequence of the mentioned sum rule for the Γ_n.

For the Liouville operator (3.6), not only the stationary current, but also the zero-frequency noise (2.22) can be evaluated exactly. Starting from the latter expression, one obtains after some lines of straightforward calculation the result

$$S = \frac{e^2}{32\hbar} \sum_{n,n'=1}^{3} \frac{\Gamma_n^2}{\Gamma_{n'}} + \frac{e^2}{16\hbar} \sum_{n=1}^{3} \frac{\Gamma_1\Gamma_2\Gamma_3}{\Gamma_n^2}. \tag{3.7}$$

In the limit $\Gamma_{1,2} \ll \Gamma_3$, only terms with Γ_3 in the denominator are relevant, so that we obtain $S = (e^2/\hbar)\Gamma^2/32\Gamma_3$. With the above expressions for Γ_n, the corresponding Fano factor becomes

$$F_{1e} = \frac{\epsilon_2^2}{8\tau^2}. \tag{3.8}$$

It indeed exhibits the predicted parabolic dependence on the gate voltage $V_{\text{gate}} = \epsilon_2/e$. A quantitative comparison of both the current and the Fano factor with the numerical results depicted in Fig. 3.4(b) yields a satisfactory agreement in the range considered here. This implies that our one-electron model indeed captures the essential features of the electron avalanches through the triple quantum dot. Moreover, it implies that the (average) size of the avalanches is $q = e\epsilon_2^2/8\tau^2$.

The proportionality of the Fano factor to $(\epsilon_2/\tau)^2$ suggests for the transport in the one-electron regime the following scenario: Assume that the off-resonant dot is initially unoccupied, while electrons are transported via dots 1 and 3. Then, according to standard perturbation theory, electrons in these dots

may tunnel to dot 2 with a probability amplitude proportional to the tunnel matrix element divided by the energy difference, i.e. with a probability $p \propto (\tau/\epsilon_2)^2$. Thus after on average $1/p$ electrons have been transported, an electron will tunnel to dot 2 and cause temporary Coulomb blockade which is resolved only when the electron tunnels further. Thus, the dynamics is given by periods with an open channel that on average terminate after an avalanche with $1/p \propto (\tau/\epsilon)^2$ electrons has been transported. This explains the observed proportionality of the Fano factor $F \propto (\epsilon_2/\tau)^2$. This scenario also hints on why the cumulants deviate from conjecture (3.1): The average duration of an avalanche is as long as the waiting time between subsequent avalanches, while conjecture (3.1) is based on the assumption of a much shorter avalanche duration.

In the limit $\Gamma_3 \ll \Gamma$, it is still possible to evaluate some cumulants of higher order analytically, although this becomes increasingly tedious. Nevertheless it is worth proceeding up to forth order for which we obtain

$$C_1 = \frac{\Gamma}{4\hbar}, \tag{3.9}$$

$$C_2 = \frac{\Gamma}{4\hbar}\Big(\frac{\Gamma}{8\Gamma_3}\Big), \tag{3.10}$$

$$C_3 = -\frac{3\Gamma}{4\hbar}\Big(\frac{\Gamma}{8\Gamma_3}\Big)^2, \tag{3.11}$$

$$C_4 = \frac{3\Gamma}{4\hbar}\Big(\frac{\Gamma}{8\Gamma_3}\Big)^3. \tag{3.12}$$

Thus, the first two cumulants behave as expected for short avalanches with charge $q = e\Gamma/8\Gamma_3$. However, already the third and the forth cumulant deviate from the Poissonian value by a factor ± 3 in compliance with our numerical observations in Sec. 3.3.3.

3.5 Conclusions

The emergence of an interference pattern with good visibility usually requires the coherent superposition of two or more paths that are traversed with like probabilities. In an Aharonov-Bohm interferometer formed by quantum dots in ring configuration, a significant detuning of the dot that is not connected to any lead has the consequence that transport through one arm requires co-tunneling. Since this reduces the transmission probability of that path, the interference pattern as a function of a penetrating flux will fade away. We have demonstrated that, nevertheless, strongly detuned interferometers bear interesting effects manifest in the noise properties of the current. In particular, we have shown that strong electron bunching may occur. It turned out that this is most pronounced in the low bias regime in which Coulomb repulsion forbids the occupation of the triple quantum dot by more than one electron.

The prime quantity of interest in that context is the Fano factor for which we have predicted huge values: the relative noise strength may exceed that of a Poisson process by several orders of magnitude. This has led us to the conclusion that the current consists of avalanches with a finite duration. The physical reason for this is that electrons may become trapped in the off-resonant quantum dot, such that Coulomb blockade interrupts the transport until the trapped electron is released. The analysis of the higher-order charge fluctuations—the full-counting statistics—has revealed that the cumulants grow even super exponentially with their order.

For the computation of the full-counting statistics, we have employed the iterative scheme recently developed in Ref. [48]. This has been essential for the treatment of the three-dot problem, since the Hilbert space is already too large for a full analytical treatment. Nevertheless, in the most relevant

regime of single occupation, we have performed the first iteration steps analytically, such that we have obtained expressions for the first four cumulants in the limit of strong detuning.

In conclusion, we have studied electron interferometers in a regime that so far has not attracted much attention, most likely due to the lack of pronounced interference effects. Precisely in this regime, however, the shot noise properties are most interesting and strong electron bunching occurs. Thus, quantum dots in ring configuration may serve not only for the observation of interference effects, but also for the creation of currents with widely tunable super-Poissonian fluctuations.

Chapter 4

Phonon-mediated decoherence in triple quantum dots interferometers

If you have a problem with the third act, the real problem is in the first act.
Billy Wilder

Summary

In this chapter we study transport through a triple quantum dot in a ring configuration (see Fig. 4.2) under the influence of the interaction with a damped phonon mode [34]. We will focus on the situation where the dot energy levels are near resonance, and therefore interference is important. It has been theoretically shown that in this situation interference phenomena blocks transport in what is known as dark state, that is, an electron is trapped in the superposition [110, 37]

$$|\Psi_{\rm dark}\rangle = \frac{1}{\sqrt{2}}(|1\rangle - |2\rangle). \tag{4.1}$$

Obviously, it is orthogonal to state $|3\rangle$ and, thus, is decoupled from the drain. This implies that once an electron populates state (4.1), it cannot leave the triple dot. Since Coulomb repulsion inhibits further electrons from entering the dots, the current vanishes. Therefore, in this situation decoherence destroys the perfect superposition determining transport through the system. In this chapter we have studied the decoherence produced by the interaction with a damped phonon mode and we provide an effective Liouvillian that allows to study analytically the current and to have a clear image of the decoherence mechanism.

The chapter is organized as follows. In Sec. 4.2 we introduce the phonon-system-lead Hamiltonian and derive a quantum master equation with which we investigate in Sec. 4.3 the impact of decoherence on the current and its noise. Section 4.4 is devoted to an effective master equation for only the dot electrons based on a polaron transformation.

4.1 Brief introduction to decoherence

The natural enemy of interference is decoherence, i.e., the loss of the quantum mechanical phase. Decoherence is the result of the formation of quantum correlations with the environment. These

correlations are responsible of the strikingly different behavior of isolated and interacting systems.

Let us for example imagine that we can separate two quantum systems, $\mathcal{S}$ and $\mathcal{M}$, from the rest of the environment and make them interact and evolve according to the Scrödinger equation, that is

$$|\varphi\rangle|\phi\rangle \;\rightarrow\; \sum_n c_n(t)|\varphi_n(t)\rangle|\phi_n(t)\rangle \tag{4.2}$$

so that both systems become entangled.

In the case that, for example, the system $\mathcal{M}$ has many degrees of freedom, this entanglement becomes irreversible. Therefore, it is important to note that the environment can not be ignored or treated as a classical background. In this way, we see that decoherence and irreversibility are intimately related. Nevertheless, decoherence has not to be identified with dissipation. Decoherence precedes dissipation acting on a much faster timescale.

Details of the dynamics depend on the kind of coupling between the system we consider and the environment. In mesoscopic devices, the interaction of the environment will play the role of the measurement process. that the considered system interacts with environmental degrees of freedom and, thus, becomes entangled with them. Then, without specifying the state of the environment one must average over all possible states of the environment, diminishing the interference and thus, the system tends to behave classically.

We can differentiate between three sources of decoherence depending on the nature of the environment [153]. The most frequently employed model for describing decoherence is the linear coupling of a central system to a bath of harmonic oscillators representing, e.g., phonons or photons [105, 43, 21, 97, 64]. Owing to the linearity of both the bath and its coupling to the system, the former can be eliminated [42] yielding a master equation or a path integral description of the now dissipative central system. An example of this is a spatial delocalized particle [62] interacting weakly with an environment sensitive to its position. Thus, a cloud is built around the particle, measuring to some extent its position which leads to the destruction of the coherences. If decoherence stems from the coupling to localized modes baths such as nuclear spins or defects, a spin bath model is more appropriate [152, 146, 128]. This time, is the environmental spin phase which measures the spin phase of the central system, [152] leading to a much more effective decoherence action. A slightly different scenario is the so-called "third-party decoherence" [153] in which a quantum system couples via a further small quantum system to a bath consisting of many degrees of freedom (see Fig. **??**). A particular case is the coupling of the quantum system via a harmonic oscillator to a bath of harmonic oscillators. This system-oscillator-bath model is equivalent to a system-bath model with a spectral density peaked at the oscillator frequency,[172, 157, 57] unless nonlinearities of the oscillator are taken into account.[166]

Coherent coupling of discrete electronic states with discrete phonon modes leads to effects to similar to those obtained with phonon cavities. Experimentally, such coupling has been found in carbon

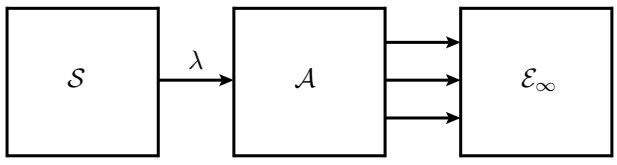

Fig. 4.1: Pictorical representation of the "third party" decoherence, where the main system $\mathcal{S}$ interacts with another quantum system $\mathcal{A}$ which is at the same time interacting with the environment $\mathcal{E}$.

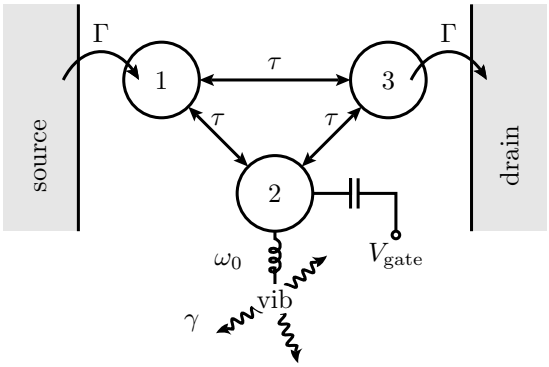

Fig. 4.2: Triple quantum dot in ring configuration with mutual tunnel couplings τ. Dots 1 and 3 possess onsite energies $\epsilon_{1,3} = 0$ and are tunnel coupled to the source and the drain, respectively. Dot 2 interacts with a damped vibrational mode with frequency ω_0, while its onsite energy can be tuned by a gate voltage such that $\epsilon_2 = V_{\text{gate}}/e$. Dot 2 has a vibrational degree of freedom, while dots 1 and 3 are rigidly attached to the contacts.

nanotubes [101], and also in single [171] and double [170, 135] quantum dots. In these systems, the phonon mediates "third-party decoherence" to the electrons. Here we investigate how the coupling of dot electrons in a triple quantum dot interferometer to a localized dissipative single phonon mode influences the destructive interference. We focus on the regime of weak dot-lead tunneling in which a master equation description is appropriate. Nevertheless, the electron dynamics may exhibit non-Markovian effects stemming from the coupling to the oscillator. Therefore, it is technically advantageous not to eliminate the oscillator but to treat it as part of the central system.

4.2 Model and Hamiltonian

4.2.1 Triple quantum dot attached to electron reservoirs

In order to describe transport through the triple quantum dot we use the same model as in the last chapter, that is coherent coupling between dots (see eq. (1.1)) and the Born-Markov approximation for the electron reservoirs (see eq. (1.6)). This time we restrict the transport regime to the limit of strong inter-dot and intra-dot Coulomb repulsion such that only the states with zero or one excess electron on the ring are relevant. Thus, the only relevant states are the empty state $|0\rangle$ and the one-electron states $|i\rangle = c_i^\dagger|0\rangle$, where $i = 1, 2, 3$ refers to the dot on which the electron resides and $c_i^\dagger$ is the associated electron creation operator.

4.2.2 Electron-phonon interaction

Electron-phonon interaction affects transport in several ways. As we mentioned above, in this work we will focus on the decoherence given in the dark state given by eq. (4.1). Therefore most of the effects can be captured in a model that just considers the interaction in one of the dots 1 or 2. Thus, for the sake of simplicity we will just consider the interactions of electrons passing through dot 2. Therefore,

we linearly couple them with a phonon mode according to [16]

$$H_{\text{ph}} = \hbar\omega_0 a^\dagger a, \tag{4.3}$$

$$V_{\text{e-ph}} = \lambda c_2^\dagger c_2 (a^\dagger + a), \tag{4.4}$$

which can be interpreted as a dynamical energy shift. In turn, an electron on dot 2 entails a force on the oscillator, such that the latter acquires information about the path that an electron takes on its way from source to drain. Such "which way information" influences interference properties. Notice that we treat the coupling energy λ as parameter despite the fact that it can be determined from microscopic considerations [16]. At the end of the chapter we will extend the formalism to all dots and see that there is an extra interference effect that is not included in the present set-up.

Dissipation of the localized phonon mode stems from the interaction with a bosonic environment such as substrate phonons. The environment and its coupling to mode a are described by the system-bath Hamiltonian

$$H_{\text{env}} = \sum_\nu \hbar\omega_\nu a_\nu^\dagger a_\nu, \tag{4.5}$$

$$H_D = (a^\dagger + a) \sum_\nu \lambda_\nu (a_\nu^\dagger + a_\nu), \tag{4.6}$$

where a_ν and $a_\nu^\dagger$ are the creation and annihilation operators of the bath modes, while λ_ν are the coupling constants. The influence of the environment is fully determined by its spectral density $I(\omega) = \pi \sum_\nu |\lambda_\nu|^2 \delta(\omega - \omega_\nu)$, which we assume to be Ohmic, i.e., $I(\omega) = \gamma\omega$, where γ denotes the effective damping rate.

4.2.3 Quantum master equation

In order to derive a master equation for the dissipative dynamics of the triple quantum dot and the localized mode, we start from the Liouville-von Neumann equation for the full density operator, $i\hbar\dot{R} = [H_{tot}, R]$, where H_{tot} is the sum of all the Hamiltonians appearing above. Using standard techniques [12], we obtain for the reduced density operator the equation of motion

$$\dot{\rho} = -\frac{i}{\hbar}[H_0, \rho] - \frac{1}{\hbar^2}\text{tr}_{\text{leads+bath}} \int_0^\infty dt [H_V, [\tilde{H}_V(-t), R]] \equiv \mathcal{L}\rho, \tag{4.7}$$

which can be evaluated under the factorization assumption $R \approx \rho_{\text{leads},0} \otimes \rho_{\text{bath},0} \otimes \rho$. We have defined $H_0 = H_{\text{TQD}} + H_{\text{ph}} + V_{\text{e-ph}}$. The tilde denotes the interaction picture $\tilde{X}(t) = U_0^\dagger(t) X U_0(t)$, where $U_0(t) = \exp\{i(H_0 + H_{\text{leads}} + H_{\text{bath}})t/\hbar\}$. The coupling of the central system to the leads and the heat bath has been subsumed in the interaction Hamiltonian $H_V = H_{\text{dot-leads}} + H_D$.

We insert $H_{\text{dot-leads}}$ and H_D and evaluate the trace of the electron and phonon reservoirs to obtain the Liouvillian [3, 60]

$$\begin{aligned}\mathcal{L}\rho = &-\frac{i}{\hbar}[H_0, \rho] - \frac{\Gamma_L}{\hbar}(2c_1\rho c_1^\dagger - c_1^\dagger c_1\rho - \rho c_1^\dagger c_1) - \frac{\Gamma_R}{\hbar}(2c_3^\dagger\rho c_3 - c_3 c_3^\dagger\rho - \rho c_3 c_3^\dagger) \\ &+ \frac{\gamma}{2}(\bar{n}+1)(2a\rho a^\dagger - a^\dagger a\rho - \rho a^\dagger a) + \frac{\gamma}{2}\bar{n}(2a^\dagger\rho a - aa^\dagger\rho - \rho aa^\dagger),\end{aligned} \tag{4.8}$$

where $\bar{n} = [\exp(\hbar\omega_0/k_BT) - 1]^{-1}$ is the thermal occupation number of the localized mode at temperature T. Restricting ourselves to the limit in which all dot states lie within the voltage window, we have replaced the Fermi function of the left lead by 1 and that of the right lead by 0. Only in this limit, the

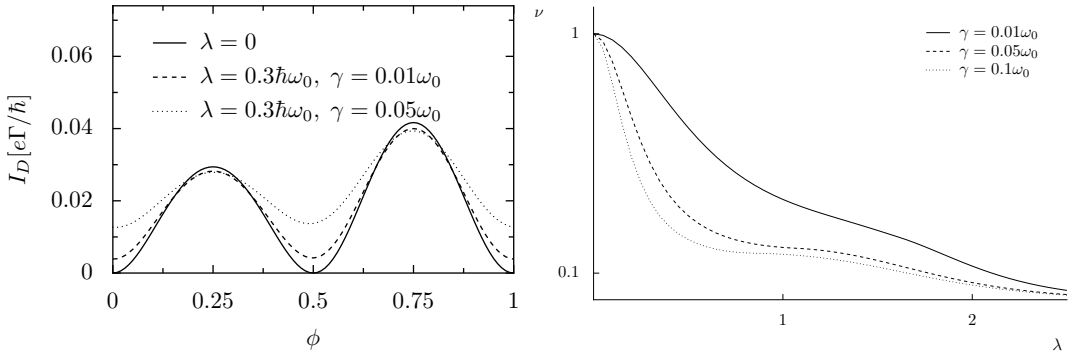

Fig. 4.3: Left pannel shows current at zero detuning, $\epsilon_2 = 0$, as a function of the scaled magnetic flux ϕ for two values of the phonon damping strengths γ compared to the current in the absence of the phonon ($\lambda = 0$). The dot-lead tunneling rate is $\Gamma = 0.1\omega_0$. In the non-interacting case, the current drops to zero at semi-integer values of the quantum flux. The Aharonov-Bohm amplitude is reduced by the phonon-mediated decoherence of the dark state. Right pannel shows a plot of the visibility ν vs. λ for three different values of $\gamma = 0.01\omega_0$, $0.05\omega_0$ and $0.1\omega_0$.

dot-lead tunnel terms proportional to $\Gamma_{L,R}$ assume this simple form. Moreover, we consider the oscillator dissipation within rotating-wave approximation [55]. In contrast to the last chapter, we are allowed to use the localized basis of the system because we work in the infinite bias regime.

We use current and noise operators from the last chapter, for unidirectional transport, i.e. $\mathcal{J}^- = 0$, and

$$\mathcal{J}^+ = \frac{e\Gamma_3}{\hbar} c_3^\dagger \rho c_3. \tag{4.9}$$

Then the stationary current and noise [116] expectation values read

$$I = \mathrm{Tr}\mathcal{J}^+\rho_\infty, \tag{4.10}$$

$$S = e\mathrm{Tr}\mathcal{J}^+\rho_\infty - 2e\mathrm{Tr}\mathcal{J}^+\hat{\mathcal{L}}^{-1}\mathcal{J}^+\rho_\infty, \tag{4.11}$$

where ρ_∞ denotes the stationary solution of the master equation (4.8), and $\hat{\mathcal{L}}^{-1}$ is the pseudo-inverse of $\mathcal{L}$, whose action on $\mathcal{L}\rho_\infty \equiv X$ is computed by solving $\mathcal{L}X = \mathcal{J}^+\rho_\infty$ under the condition $\mathrm{Tr}X = 0$. Below we will always discuss the noise strength in relation to the current. This motivates the definition of the Fano factor $F = S/eI$, which assumes the value $F = 1$ for a Poisson process.

For a numerical solution, we will have to truncate the Hilbert space of the localized phonon mode at some maximal phonon number N. Unless explicitly stated otherwise, truncation at $N = 20$ ensured numerical convergence.

4.3 Numerical observations

In this section we briefly explain the behavior of the numerical results obtained from the quantum master equation, which accounts the whole electron-phonon system. We differentiate between two different regimes, $\epsilon_2 \gg \tau$ and $\epsilon_2 \lesssim \tau$.

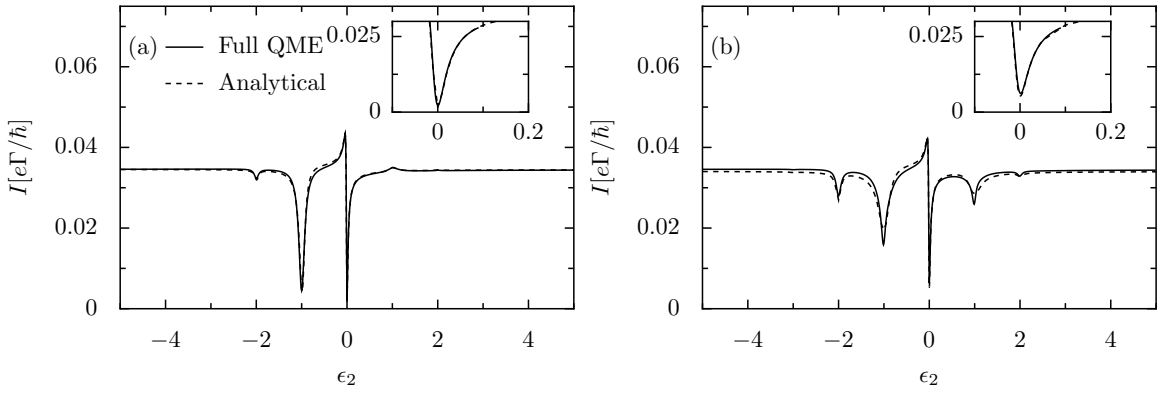

Fig. 4.4: Comparison of the results with the full quantum master equation (4.8) and those of the effective master equation (4.31) for $\lambda = 0.1\hbar\omega_0$, $\gamma = 0.05\omega_0$, $\tau = 0.01\hbar\omega_0$ and $\Gamma = 0.1\omega_0$. The temperature is(a) $T = 0$ and (b) $T = 1.5\hbar\omega_0/k_B$.

4.3.1 $\epsilon_2 \gg \tau$

As we have already seen in the previous chapter, when dot 2 is strongly detuned, i.e., for $|\epsilon_2| \gg \tau$, tunneling from and to this dot becomes off-resonant. Thus, the direct path from dot 1 to dot 3 is much more likely than the detour via dot 2. Then, in the absence of the oscillator, we expect interference effects to play a minor role. Nevertheless, electrons may be trapped in dot 2 such that the current flow is interrupted until the trapped electron tunnels off-resonantly to dot 3 and transport is restored. Consequently, the electron transport becomes bunched [35]. The current plotted in Fig. 4.4 demonstrates that this scenario needs to be refined when the electron on dot 2 couples to a vibrational mode, because then temporal electron trapping can be caused also by emission and absorption of phonons. This leads to dips and peaks in the current whenever ϵ_2 is detuned by roughly an integer multiple of $\hbar\omega_0$. For finite temperature and negative detuning [Fig. 4.4(b) for $\epsilon_2 < 0$], the dips are caused by the predominating phonon emission, while those for positive detuning are due to the a more frequent absorption (see discussion below concerning C_ϵ). The different size of the peaks and dips for positive and negative values of ϵ [Fig. 4.4(b)] stems from spontaneous processes which render emission more likely than absorption. In the zero temperature limit [Fig. 4.4(a)], phonon absorption no longer occurs and consequently, the dips at positive detuning vanish. Then small peaks emerge, which correspond to the relaxation of electrons that temporally populate in dot 2. As we can clearly appreciate in Fig. 4.4, results obtained by means of the effective master equation fit rather well with those obtained with the quantum equation.

4.3.2 $\epsilon_2 \lesssim \tau$

At zero flux, $\phi = 0$, the two paths $|1\rangle \to |3\rangle$ and $|1\rangle \to |2\rangle \to |3\rangle$ interfere destructively at the drain [110, 37]. If ϕ is changed, a finite current flows, unless ϕ assumes a semi-integer value [37, 19], as is visible from the Aharonov-Bohm oscillations depicted in Fig. 4.3. Figure 4.3 also shows that when coupling dot 2 to the oscillator, Aharonov-Bohm oscillations fade out with increasing dissipation strength γ, which is a signature for the influence of decoherence. Moreover, it can be seen that this fading can be read off faithfully at $\phi = 0$ and, thus, henceforth we restrict ourselves to this value. The insets of Fig. 4.4

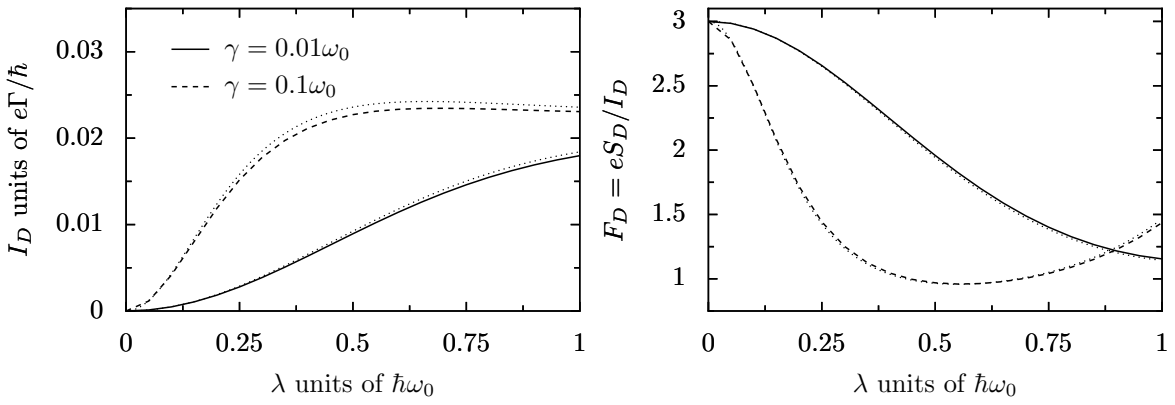

Fig. 4.5: Current and Fano factor as a function of the electron-phonon coupling for the dark state, i.e., for the detuning $\epsilon = \epsilon_2 - \lambda^2/\hbar\omega_0 = 0$, at zero temperature and two values of the dissipation strength γ. All other parameters are as in Fig. 4.4(a). The dotted lines mark the results obtained with the reduced master equation (4.31). Numerical convergence was reached when considering $N = 25$ Fock states of the phonon mode.

show the current as a function of the detuning for the electron-phonon coupling strengths $\lambda = 0.1\hbar\omega_0$ and two different temperatures for small detuning. An interesting observation is that with increasing electron phonon coupling (not shown), the minimal current not only grows, but also is shifted from $\epsilon_2 = 0$ to the value $\epsilon_2 = \lambda^2/\hbar\omega_0$. This shift can be obtained by a polaron transformation, as we will detail in Sec. 4.4.

As a criterion for the relevance of interference, we compute the visibility

$$\nu = \frac{I_{\max} - I_{\min}}{I_{\max} + I_{\min}}, \tag{4.12}$$

where $I_{\max} = \max_\Phi I(\Phi)$ is the maximal current upon flux variation for a given gate voltage, and $I_{\min}$ is defined accordingly. In the right pannel of Fig. 4.3 we show ν vs. λ for three different values of the coupling with the dissipative bath γ. As expected, decoherence is more severe for a higher coupling γ.

The influence of the electron-phonon interaction on the current close to the dark state can be seen in figures 4.5(a) and 4.6. There, we show the current as a function of the electron-phonon coupling and the temperature, respectively, for a detuning $\epsilon = 0$ which corresponds to the dark state. Both plots confirm that the current blockade is resolved with increasing electron-phonon coupling and temperature, underlining the growing importance of decoherence. The current saturates at the value $I_D \approx 0.02e\Gamma/\hbar$, as a function of the electron-phonon coupling λ; see Fig. 4.5(a). Figure 4.5(b) depicts the associated current noise in terms of the Fano factor. As the electron-phonon coupling increases, both the current and the shot noise become larger. Initially, the current grows faster than the shot-noise, and consequently the Fano factor is reduced; see Fig. 4.5(b). Once the electron-phonon coupling λ becomes of the order $\hbar\omega_0$, this tendency is reversed. While the current saturates, the shot noise keeps growing, as is visible in the behavior of the Fano factor. For larger values of λ, numerical convergence requires taking an increasing number of oscillator states into account, which limits the observable range.

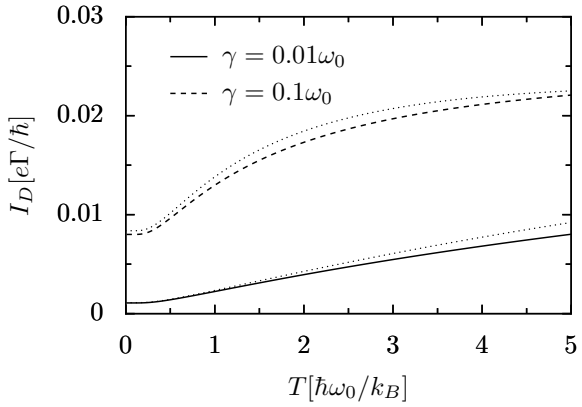

Fig. 4.6: Current as a function of the temperature for electron-phonon coupling $\lambda = 0.15\hbar\omega_0$, $\Gamma = 0.1\omega_0$ and detuning $\epsilon = \epsilon_2 - \lambda^2/\hbar\omega_0 = 0$, corresponding to the dark state. The dotted lines are obtained with the reduced master equation (4.31) for the dot electrons.

4.4 Effective master equation

In this section we obtain an effective master equation for the electronic part by tracing out the phonon degree of freedom. In order to trace out the phonon mode and try to keep most of the dynamical effects on the electronic part, one can take advantage of the fact that the dynamics of the phonon mode are much faster than the electronic system. Thus, we can imagine that a cloud of phonons dresses instantaneoulsy the electron moving coherently between the dots. Consequently, the system can be acurately described by the so-called displacement-oscillator ansatz [150, 67]

$$|\Psi\rangle = \alpha_1|1\rangle|0_{ph}\rangle + \alpha_2|2\rangle|\lambda_{ph}\rangle + \alpha_3|3\rangle|0_{ph}\rangle, \tag{4.13}$$

where λ_{ph} is a variational parameter. Then, we apply the polaron transformation, which consists basically in a displacement of the phonon mode to its ground state, that is

$$|\Psi\rangle = (\alpha_1|1\rangle + \alpha_2|2\rangle + \alpha_3|3\rangle) \otimes |0_{ph}\rangle. \tag{4.14}$$

and trace out the phonon degree of freedom from the Hamiltonian. One then finds that the variational parameter is equal to $\lambda/\hbar\omega_0$. Below, we will perform the polaron transformation to the whole quantum master equation and then we will trace out the phonon degree of freedom.

4.4.1 Polaron transformation

We start with the unitary transformation [150, 67, 119, 106, 15] $O \to \bar{O} = SOS^\dagger$ of the master equation (4.8), where

$$S = \exp\left[\frac{\lambda}{\hbar\omega_0}\hat{n}_2(a^\dagger - a)\right], \tag{4.15}$$

beeing $\hat{n}_2 = c_2^\dagger c_2$, so that the transaffects operators containing $c_2^{(\dagger)}$. Performing such transformation to the Hamiltonian corresponds to the replacements

$$a^{(\dagger)} \to a^{(\dagger)} - \frac{\lambda}{\hbar\omega_0}\hat{n}_2 \tag{4.16}$$

$$c_2 \to c_2 X^\dagger, \tag{4.17}$$

with the phonon displacement operator

$$X = \exp\Big[\frac{\lambda}{\hbar\omega_0}(a^\dagger - a)\Big]. \tag{4.18}$$

Notice that all lead and bath operators remain unchanged. The Hamiltonian H_0 then reads

$$\bar{H}_0 = \epsilon\widehat{n}_2 + \tau(c_1^\dagger c_3 + c_2^\dagger c_3 X + c_1^\dagger c_2 X^\dagger + \text{h.c.}) + \hbar\omega_0 a^\dagger a, \tag{4.19}$$

where $\epsilon = \epsilon_2 - \lambda^2/\hbar\omega_0$ denotes the effective detuning, about we have spoken above.

We also have to perform the polaron transformation to the rest of the Liouvillian. It can be demonstrated that for the infinite bias regime, the tunnel dot-lead couplings remain unchanged. However, one has to perform the transformation to the phonon damping terms of the general Liouvillian (4.8), that is

$$\mathcal{L}_{\text{damping}} = \frac{\gamma}{2}(\bar{n}+1)(2\bar{a}\rho\bar{a}^\dagger - \bar{a}^\dagger\bar{a}\rho - \rho\bar{a}^\dagger\bar{a}) + \frac{\gamma}{2}\bar{n}(2\bar{a}^\dagger\rho\bar{a} - \bar{a}\bar{a}^\dagger\rho - \rho\bar{a}\bar{a}^\dagger), \tag{4.20}$$

by the simple substitution of the rule given in eq. (4.16).

4.4.2 Elimination of the dissipative mode

The next step consists in tracing out of the phonon mode. There are two different kinds of Liouvillians. The first one is given by the resulting transformation of eq. (4.20), which can be directly and easily done because the only electron operator it has is n_2, which is approximately constant in the interaction picture. On the other hand, we have the Hamiltonian given by eq. (eq:imint) which contains electron and phonon operators that change dynamically. In order to keep the phonon influence on the electronic system, we take second order expansion and trace the damped phonon mode, taking into account that the phonon terms in the transformed Hamiltonian are proportional to the small quantity τ. In order to do this we follow the recipe given in chapter 2. The first thing is to obtain the interaction picture, then second order Born expansion, Markov approximation and finally the trace of the damped phonon mode.

Interaction picture We take the interaction picture respect to the Hamiltonian

$$H_{\text{TQD,eff}} = \epsilon\hat{n}_2 + \tau(c_1^\dagger c_3 + \text{h.c.}) + \bar{\tau}(c_2^\dagger c_3 + c_1^\dagger c_2 + \text{h.c.}) \tag{4.21}$$

where the electron tunneling τ between dot 2 and the two other quantum dots is renormalized according to

$$\bar{\tau} = \tau\langle X\rangle = \tau\exp\Big\{-\Big|\frac{\lambda}{\omega_0}\Big|^2 \coth\Big(\frac{\hbar\omega_0}{2k_BT}\Big)\Big\}. \tag{4.22}$$

We then treat the tunnel terms

$$H_Y = \tau(c_2^\dagger c_3 Y + c_1^\dagger c_2 Y^\dagger + \text{h.c.}). \tag{4.23}$$

to second order in the Bloch-Redfield approximation. We have used the phonon part of the interaction, $Y = X - \langle X\rangle_{\rm eq}$, such that $\langle H_Y\rangle_{\rm eq}$ vanishes. It is important to note that the phonon mode is damped by the bath of oscillators. For this reason, we use the Heisenberg picture of the displacement operators

$$X_t = \exp\left(\frac{\lambda}{\hbar\omega_0}\left(-ae^{-(i\hbar\omega_0+\gamma/2)t} + a^\dagger e^{(i\hbar\omega_0-\gamma/2)t}\right)\right) \tag{4.24}$$

which accounts for the irreversible coupling.

Born-Markov approximation In this study we restrict ourselves to the easiest scenario, that is, the assumption of a decoupled time evolution of the boson works well at any detuning. This route has been taken in Refs. [15, 16], and it is equivalent to the non-interacting blip approximation common in quantum dissipation [32, 31, 112]. Then, using such a decoupling of the reduced density matrix we obtain

$$\tilde\rho(t') \approx \rho^0_{\rm ph}{\rm Tr}_{\rm ph}\tilde\rho(t'), \tag{4.25}$$

neglecting possible backaction effects. We also make use of the Markov approximation so that we make the substitution $\rho(s) \to \rho(t)$. **Second order expansion** We are now ready to take the trace over the phonon mode, yielding

$$\frac{d}{dt}\tilde\rho(t)_e = -\frac{1}{\hbar^2}\int_0^t ds{\rm Tr}_{\rm ph}\left\{\left[\tilde H_Y(t),\left[\tilde H_Y(s),\tilde\rho(t)\right]\right]\right\} \tag{4.26}$$

The commutator and the double commutator give rise to four different terms which are evaluated with the help of the quantum regression theorem. These are

$$c_i^\dagger c_j(t)\rho(t)\langle X_t\rangle \to \text{renormalization of the tunnel interdot,} \tag{4.27}$$
$$c_i^\dagger c_j(t)\rho(t)c_i^\dagger c_j(s)\langle X_t^\dagger X_s\rangle \to \text{correlation functions,} \tag{4.28}$$
$$c_i^\dagger c_j(t)\rho(t)c_i^\dagger c_j(s)\langle X_t X_s\rangle, \to \text{counterrotating terms, negligible} \tag{4.29}$$
$$c_i^\dagger c_2(t)\rho(t)c_2^\dagger c_j(s)\langle X_t^\dagger X_s\rangle \to \text{time ordering changed, negligible.} \tag{4.30}$$

Taking into account just those terms which arise from eqs. (4.27) and (4.28), and taking back the the Liouvillians of the leads $\mathcal{L}_{\rm res}$ and the polaron transformed and reduced phonon damping given by the trace of eq. (4.20), we arrive to

$$\frac{d}{dt}\rho_e(t) = -\frac{i}{\hbar}\left[\overline{H}_0,\rho_e(t)\right] - \frac{i}{\hbar}\bar\tau\left[p_{12}+p_{23}+h.c.,\rho_e(t)\right] + \mathcal{L}_{\rm res}\rho_e(t) + \mathcal{L}_{\rm decoh}\rho_e(t) + \mathcal{L}_{\rm corr}\rho_e(t). \tag{4.31}$$

In the derivation of this Liovillian we have neglected terms like (4.29) and (4.30), for different reasons. The term (4.29) depends on the time $t+s$ and, thus, is rapidly oscillating. Therefore it can be neglected within a rotating-wave approximation. Finally, terms of the type (4.30) come in pairs with opposite time-ordering and opposite sign. Therefore their net contribution is proportional to a commutator and, thus, is of the order τ, i.e., one order beyond what is considered in the master equation (4.31).

We can see that apart from the tunnel renormalization, two additional Liouvillians emerge. The first one, $\mathcal{L}_{\rm decoh}$, describes decoherence of the dark state, and is directly obtained replacing eq. (4.16) in the last two terms of the master equation (4.8) and reads

$$\mathcal{L}_{\rm dec}\rho_e = \frac{\gamma}{2}(1+2\bar n)\Big(\frac{\lambda}{\hbar\omega_0}\Big)^2(2\hat n_2\rho_e\hat n_2 - \hat n_2\rho_e - \rho_e\hat n_2), \tag{4.32}$$

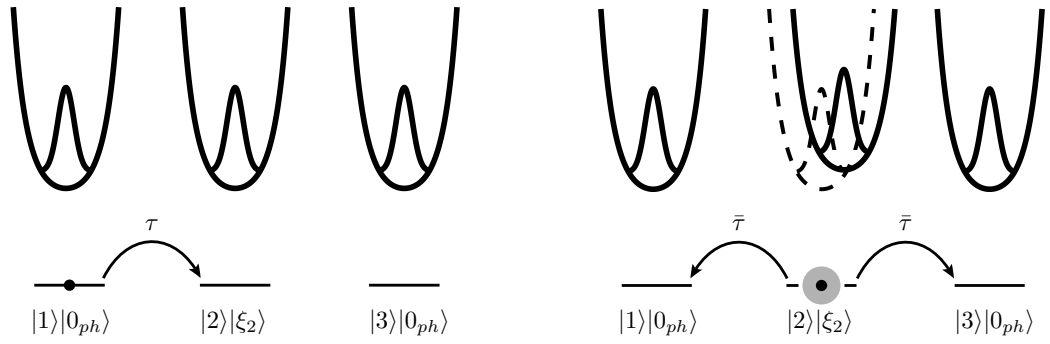

Fig. 4.7: Illustrative schema of the tunnel renormalization by the interaction with the phonon mode. When the electron passes through dot 2 a phonon cloud surrounds the position of the electron. Consequently, the electron mass is renormalized and the tunnel decreases exponentially.

where we have used the operator relation $\hat{n}_2^2 = \hat{n}_2$. While $\mathcal{L}_{\rm corr}$, stems from the double commutator in the Bloch-Redfield master equation (4.26)

$$\begin{aligned}\mathcal{L}_{\rm corr}\rho_e(t) = &-\left(\frac{\tau}{\hbar}\right)^2 \left(C_{-\epsilon}(\hat{n}_1+\hat{n}_3)\rho_e(t) + C^*_{-\epsilon}\rho_e(t)(\hat{n}_1+\hat{n}_3) + C_\epsilon \hat{n}_2\rho_e(t) + C^*_\epsilon \rho_e(t)\hat{n}_2\right)\\ &+2\left(\frac{\tau}{\hbar}\right)^2 \left(\mathcal{R}(C_{-\epsilon})\left(p_{23}\rho_e(t)p^\dagger_{23} + p^\dagger_{12}\rho_e(t)p_{12}\right) + \mathcal{R}(C_\epsilon)\left(p_{12}\rho_e(t)p^\dagger_{12} + p^\dagger_{23}\rho_e(t)p_{23}\right)\right), \qquad (4.33)\end{aligned}$$

and describes incoherent tunneling between the quantum dots where $C_\epsilon \equiv C'_\epsilon + iC''_\epsilon$ denotes the phonon correlation function in Laplace space, derived in appendix E.

4.5 Elements of the effective master equation

4.5.1 Tunnel renormalization

As we have already explained, the fact that the phonon dynamics is much faster than the electron moving between dots, makes possible that a cloud of phonons follows instantaneously any change in the position of the electron (see Fig. 4.7 for illustration). This fact makes that the electron mass becomes renormalized. The consequence of this renormalization is an exponential reduction of the interdot tunnel $\tau \to \bar{\tau}$. Following the reasoning of the last chapter, this renormalization will increment the Fano factor (see higher values of λ in Fig.4.5). By itself, the tunnel renormalization does not lead to the decoherence of the dark state and thus to finite current. Indeed, renormalization can be externally compensated by means of a gate voltage [38] and the dark state will be displaced from $\epsilon = 0$ as

$$\epsilon_0 = \frac{\tau_{12}}{2\tau_{13}\tau_{23}}\left(\tau_{13}^2 - \tau_{23}^2\right). \qquad (4.34)$$

In fact, in the limit $\gamma \to 0$, we can find a value of the detuning where the current drops to zero, as we have seen in the introduction.

4.5.2 Liouvillian affecting at $\epsilon \gg \tau$

As we have seen above, when detuning of dot 2 is proportional to an integer value of the frequency ω_0, the influence of the damped phonon mode is given in form of peaks and dips in the current

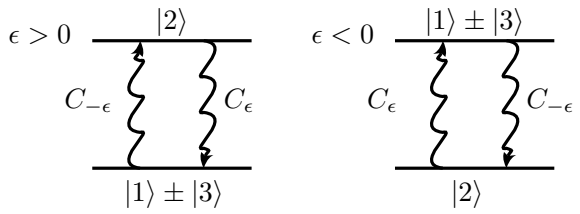

Fig. 4.8: Illustration of the incoherent tunnels betweeen the states $|2\rangle$ and $|1\rangle \pm |3\rangle$ weighted by the correlation function C_ϵ for the tunnel $|2\rangle \to |1\rangle \pm |3\rangle$, and $C_{-\epsilon}$ for $|1\rangle \pm |3\rangle \to |2\rangle$.

spectrum. This behavior is recast in the extra Liouvillian $\mathcal{L}_{\rm corr}$. It describes incoherent tunnel processes between dot 2 and 1, 3 with the transfer of energy ϵ (see $P(E)$-theory [74, 14]). Incoherent tunnels are weighted by the real part of the correlation function C_ϵ, (see Fig. 4.9). Specifically, the tunnel from $2 \to 1$ and 3 is weighted by C_ϵ, while tunnels from 1 and $3 \to 2$ is weighted by $C_{-\epsilon}$ (see Fig. 4.8). Taking into account the form of the curve C_ϵ (see Fig. 4.9), we can understand the asymmetry of the intensity of the dips ($\epsilon < 0$) the peaks ($\epsilon > 0$) observed in Fig. 4.4 and their behavior with temperature.

The regime of validity of this Liouvillian is the same as for the Fermi Golden rule, that is, the coupling constant has to fulfill $\lambda \ll \hbar\omega_0$.

4.5.3 Liouvillian affecting at $\epsilon \lesssim \tau$

The term $\mathcal{L}_{\rm decoh}$ describes the indirect interaction of the infinite bath of oscillators with the electron. Due to the irreversible nature of the interaction, it gives rise to decoherence of the dark state, and therefore to a finite current. A physical picture of the electron decoherence can be developed by considering the influence of the phonon on the dark state (4.1) and the bath of oscillators. This reasoning will also yield the associated decoherence rate of the effective Liouvillian (4.32) (see below).

Numerical calculations provide evidence that $\mathcal{L}_{\rm corr}$ is not relevant for the behavior of the dark state (see Fig. 4.5). Thus, close to $\epsilon = 0$, we can neglect $\mathcal{L}_{\rm corr}$ in the master equation (4.31), and then we obtain to lowest order in τ the stationary current

$$I_D \approx \frac{4\Gamma\left[4g_1(\tau^2-\bar\tau^2)^2 + g_1 g_2 \tau^2 \Gamma_D + g_2 \bar\tau^2 \Gamma\Gamma_D\right]}{\Gamma(2\Gamma+3\Gamma_D)(4g_1\bar\tau^2 + g_2\Gamma\Gamma_D) + 4\tau^2\left(2\Gamma^3 + 7\Gamma^2\Gamma_D + 12\Gamma\Gamma_D^2 + 8\Gamma_D^3\right)}, \tag{4.35}$$

with $g_1 = \Gamma + 2\Gamma_D$, $g_2 = \Gamma + \Gamma_D$, and the effective dissipation rate $\Gamma_D = (\frac{1}{2} + \bar n)\gamma(\lambda/\hbar\omega_0)^2$. The validity of this result close to the dark state is shown with Figs. 4.5 and 4.6. The agreement is rather good for any coupling constant λ and temperature. The according result for the Fano factor also fits well (see Fig. 4.5b). A comparison in a broad range of λ, shown in Figs. 4.5 and 4.6, demonstrates that the approximation is globally valid.

Physical picture of the decoherence mechanism

Let us assume that the electron resides in the dark state $|\Psi_{\rm dark}\rangle \propto |1\rangle - |2\rangle$. Its time evolution under the influence of the phonon is determined by the interaction-picture Hamiltonian

$$H_I(t) = \lambda \hat n_2(t)(a^\dagger e^{i\omega_0 t} + a e^{-i\omega_0 t}). \tag{4.36}$$

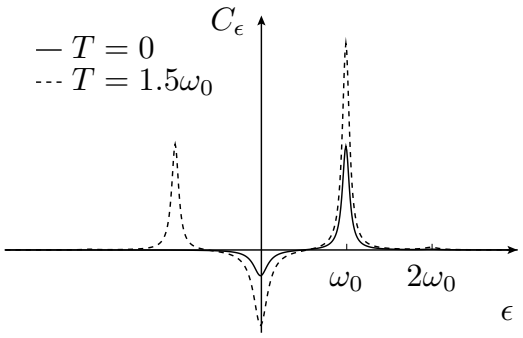

Fig. 4.9: Real part of the correlation function versus the energy ϵ at two different temperatures $T = 0K$ and $T = 1.5\hbar\omega_0$, $\lambda = 0.15\hbar\omega_0$ and $\gamma = 0.1\omega_0$. In the first case, $T = 0K$ just emission is possible and thus, only C_ϵ for $\epsilon > 0$ is finite. This function weights the incoherent tunnel coupling between states $|2\rangle$ and $|1\rangle$ and $|3\rangle$, see discussion in the main text.

Since the electron dynamics is much slower than the oscillator, the number operator $\hat{n}_2$ is essentially time-independent. Then the time ordering in the corresponding time-evolution operator

$$U(t) = T_{\leftarrow} \exp\Big[-\frac{i}{\hbar} \int_0^t ds\, H_I(s) \Big] \tag{4.37}$$

can be evaluated by employing the commutation relation [17]

$$[H_I(t), H_I(t')] = 2i\lambda^2 \hat{n}_2 \sin[\omega_0(t - t')] \tag{4.38}$$

from which we obtain the propagator

$$U(t) = \exp\left[-\frac{1}{2} \int_0^t ds\, ds' [H_I(s), H_I(s')] \theta(s - s') \right] V(t). \tag{4.39}$$

The operator $V(t) = \exp\{\hat{n}_2[a^\dagger \alpha(t) - a\alpha(t)^*]\}$ describes an oscillator displacement by

$$\alpha(t) = \frac{\lambda}{\hbar\omega_0}(1 - e^{i\omega_0 t}), \tag{4.40}$$

while the integral of the commutator in Eq. (4.37) is a mere phase factor which is not relevant for the subsequent discussion and will be ignored. Thus, the dark state evolves according to

$$U(t)|\Psi_{\rm dark}\rangle = \frac{1}{\sqrt{2}}\big(|1\rangle|0\rangle_{\rm ph} - |2\rangle|\alpha(t)\rangle_{\rm ph}\big), \tag{4.41}$$

which means that the oscillator turns into a cat state, i.e., a superposition of two coherent states $|0\rangle$ and $|\alpha(t)\rangle$. Up to this moment, the bath of harmonic oscillators was undisturbed. However, once the coherent state $|\alpha(t)\rangle$ is formed, the environment starts interacting, pulling it towards the vacuum state. The evolution of the P representation [23] of this decay has the form of a spiral in the phase space [23] (see illustration of Fig. 4.10). Then, the irreversible emission of a quanta into the infinite bath

$$\frac{1}{\sqrt{2}}\big(|1\rangle|0\rangle_{\rm ph} - |2\rangle|\alpha(t)\rangle_{\rm ph}\big) \otimes |0\rangle_{\mathcal{E}} \to \frac{1}{\sqrt{2}}\big(|1\rangle|0\rangle_{\rm ph} \otimes |0\rangle_{\mathcal{E}} - |2\rangle|\alpha'(t)\rangle_{\rm ph} \otimes |1\rangle_{\mathcal{E}}\big). \tag{4.42}$$

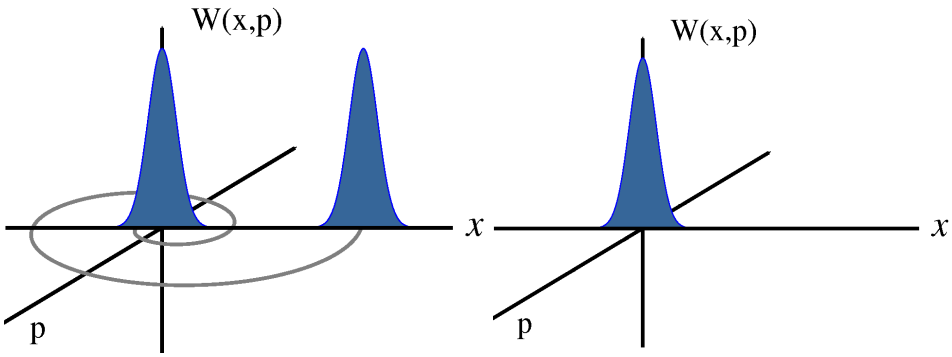

Fig. 4.10: We illustrate the evolution of the P representation of the cat state given by eq.4.41. We see that the interaction with the bath of oscillators provokes that the initial coherent state $|\alpha\rangle$ decays towards $|0\rangle$ describing a spiral in the phase space.

This process provokes that the electron-phonon cat state becomes a mixed state, namely

$$\rho_{\text{e-ph}} = |1\rangle\langle 1| \otimes |0\rangle\langle 0|_{\text{ph}} + |2\rangle\langle 2| \otimes |\alpha'\rangle\langle\alpha'|_{\text{ph}}. \tag{4.43}$$

In Appendix F we give a more detailed analysis of the decoherence produced in a superposition two coherent states by a Markovian bath of harmonic oscillators [169]. In the limit $\gamma t \ll 1$, the coherence of such a superposition decays with the rate [20, 169] $\Gamma_D(t) = (\gamma/2)(1+2\bar{n})|\alpha(t)|^2$, which in the average over one oscillation period reads

$$\Gamma_D = \frac{\gamma}{2}(1+2\bar{n})\left|\frac{\lambda}{\hbar\omega_0}\right|^2. \tag{4.44}$$

Since each of the two involved phonon states is linked to a particular electron state, we can attribute this decoherence process also to the electrons. Then we can conclude that the electron coherence also decays with the rate (4.44), which complies with the actual rate in the effective Liouvillian Eq. (4.32). Thus, the phonon elimination described above is such that the decoherence of an oscillator cat state directly turns into decoherence of the dark state.

For larger inter-dot tunneling, $\tau \gtrsim \hbar\omega_0$, the interaction-picture operator $n_2(t)$ can no longer be considered time-independent, such that our reasoning has to be modified.

4.6 Other reservoir coupling

As we have seen in the last section, the dynamics between the environment and the phonon mode determines completely the functional form of the decoherence rate, and thus of the transport. For this reason, it is of particulary interest to study the effects of different couplings between the environment and the phonon mode. As an example, we provide here the case where the phonon mode interacts with the bath of oscillators by means of an operator, $a^\dagger a$,

$$H = \hbar\omega_0 a^\dagger a + a^\dagger a \sum_\nu \lambda_\nu (a_\nu^\dagger + a_\nu) \tag{4.45}$$

With this coupling there is no energy damping, there is however a phase damping. The environment may be considered as making a measurement of the number of quanta in the system. It is worthy to not

that the operator $a^\dagger a$ is an exact pointer observable of this Hamiltonian since $[a^\dagger a, H] = 0$. It is also a quantum non-demolition obervable. This Hamiltonian leads to the master equation

$$\frac{\partial \rho}{\partial t} = -i\hbar\omega_0 \left[a^\dagger a, \rho\right] + \frac{\gamma}{2}\left(2a^\dagger a \rho a^\dagger a - a^\dagger a a^\dagger a \rho - \rho a^\dagger a a^\dagger a\right) \tag{4.46}$$

Then, performing the polaron transformation and tracing out the phonon mode we find a decoherence rate which depends on

$$\Gamma_D = \frac{\gamma}{2}(1 + 2\bar{n})\left|\frac{\lambda}{\hbar\omega_0}\right|^4 \tag{4.47}$$

4.7 Extension of the electron-phonon interaction to all dots

For the sake of simplicity, at the begining of this chapter we have assumed that the interaction affects only dot number 2. Since this interaction may differentiate one of the paths, and therefore decoherence may act and the current arises. In principle, one could expect that the main physical effect of decoherence is captured by this one-site interaction model. However, this is not entirely truth. In this section we will see that the inclusion of an extra interaction does lead to an interference effect which was disregarded in the one-site interaction.

Let us first revisit the electron-phonon Hamiltonian, and extend the interaction to all dots, by replacing eq. (4.4) by

$$V_{e-ph} = \sum_{i=1}^{3}(\lambda_i a^\dagger + \lambda_i^* a)\hat{n}_i \tag{4.48}$$

where λ_i is the *ith*-site electron-phonon coupling constant. Loosely speaking, this constant is a complex number coming from evaluating the matrix elements $\lambda_j = \langle j|e^{i\hat{\mathbf{r}}_\mathbf{j}\cdot\mathbf{q}}|j\rangle = \lambda e^{i\phi_j}$, where $\phi_j = \mathbf{q}\cdot\mathbf{r_j}$ and $\mathbf{r_j}$ is the vector accounting the position of the *jth*-dot. Assuming homogeneous dots, we obtain that the electron-phonon coupling differs from one dot to the other from a the fase factor $\phi_i - \phi_j$.

The polaron transformation is now given by

$$S = \sum_{j=1}^{3}(a^\dagger \alpha_j - a\alpha_j^*)\hat{n}_j, \tag{4.49}$$

where we have used $\alpha_j = \lambda_j/\hbar\omega_0$. The new operator leads to rewrite the transformed tunnel operators as

$$\bar{p}_{i,j}^\dagger = p_{i,j}^\dagger e^{(\beta a^\dagger - \beta^* a)} \tag{4.50}$$

$$\bar{a}^{(\dagger)} = a^{(\dagger)} - \sum_{j=1}^{3}\alpha_j^{(*)}\hat{n}_j \tag{4.51}$$

where we have used $\beta = \alpha_i - \alpha_j$. From this result we can directly extract the easy consequence that when $\alpha_i = \alpha_j$, the transformed tunnel operators remain untransformed, that is, $\bar{p}_{i,j}^\dagger = p_{i,j}^\dagger$, and therefore $\tau_{\text{renorm}} = \tau$. This does not only happens with the renormalization of the tunnel, the dark electron state and the phonon state would factorize and be $\propto (|1\rangle - |2\rangle)|\alpha(t)\rangle$. Then no phonon-induced decoherence would take place, and consequently, the dark state would continue blocking the electron transport. As it might be expected, an equal interaction leads to zero correlation function.

Another important effect is the fact that when we perform the transformation to the decoherence Liouvillian $\mathcal{L}_{\rm decoh}$, we obtain a phase dependence that was not previously considered, that is

$$\langle i|\mathcal{L}_{\rm decoh}\rho(t)|j\rangle = \frac{\gamma}{2}\left(\alpha_i^*\alpha_j - |\alpha_i|^2 - |\alpha_j|^2\right)\rho_{ij}. \tag{4.52}$$

Diagonal projection yields a zero contribution, while the nondiagonal depends on the phase difference $\alpha_i = \alpha e^{i\phi_i}$. Assuming that we can tune experimentaly the direction of the phonon wave length, we will observe current oscillations in the visibility as a function of the angle between q and d.

4.8 Approximations taken deriving the effective Liouvillian

The performed trace out of the phonon mode contains several approximations. In this section we explain in more detail two of these approximations and also we comment briefly the modification that the presented results would suffer without performing them.

4.8.1 Infinite bias regime

In the derivation of the effective master equation we have only considered the infinite bias regime. In a setup closer to real experiments one should consider a finite bias regime. In this situation there are several things that change respect to the presented scenario. The first thing that one has to have in mind is the fact that the localized basis approximation makes no sense since the dot 2 is not attached to the leads and therefore its energy (electron + phonon) as a function of the finite bias is not taken into account. Therefore, for a correct calculation in the finite bias regime one has to modify the basis of the model. This would increase considerably the total number of equations, but other approximations could be performed to keep the problem numerically tractable.

Once we have modified the basis, we can realize that the bias difference determines the number of phonons that are allowed to be occupied. For this reason, the sums performed in the trace out of the renormalized tunnel eq. (4.22) and the correlation function C_ϵ (see App. E) and the decoherence rate given in eq. (4.32) can not be taken from zero up to infinity, but up to the integer part of the ratio $\mu_L - \mu_R/\hbar\omega_0$. Consequently, all the sums are modified by reducing the rate since a less number of phonons enter into play [108].

Furthermore, there are also modifications in the dot-leads coupling $\Gamma_{\rm L,R}$ in the case of finite bias and the electron-phonon interaction affecting to all dots. Let us see for example a specific case, where the dot-lead Hamiltonian contains a term like $\sum_k c_1^\dagger l_k$. After the polaron transformation the Hamiltonian yields $\sum_k c_1^\dagger c_k X$. Then, taking the interaction picture and the double commutator, we arrive to integrals like

$$\int_0^{\mu_L} d\epsilon \int_0^\infty dt' e^{i(\epsilon-\epsilon_1)t'}\langle C(t')\rangle \approx \int_0^{\mu_L} d\epsilon C_{\epsilon-\epsilon_1} \tag{4.53}$$

making that the dot-leads coupling $\Gamma_{\rm L,R}$ becomes renormalized by the integral over ϵ of the correlation function C_ϵ. Now, we can imagine from figure 4.9 that the resulting value will suffer drastic modifications when the chemical potential of the reservoir is smaller than the frequency $\hbar\omega_0$. On the other hand, for $\lambda \ll 1$, and $\mu_{L,R} > \hbar\omega_0$, the coupling constants $\Gamma_{L,R}$, remain unchanged.

4.8.2 Zero temperature limit

In the main text we have used the Liouvillian given by eq. (4.8) to study the evolution of a damped phonon mode. We have mainly used the zero temperature approach and ocassionally its

temperature dependence. However, when we speak about decoherence we have to be a bit more carefull because decoherence at zero temperature is a topic under great discussion. In fact, the approximation used here it is not valid in that limit. This happens because in the Liouvillian that describes the phonon damping it is implicitely assumed that the correlation functions of the bath of oscillators are proportional to delta functions. This is not true for the zero temperature case because quantum correlations leave more time when the temperature is close to zero. Therefore, we use zero temperature to denote the temperature at which the reservoir correlation functions can be described by delta functions. In that case, the system is able to leave a trace in the bath, leading to decoherence.

4.9 Conclusions

We have investigated decoherence effects in a triple quantum dot interferometer the stemming from the coupling to a single dissipative bosonic mode. In our model, the dots are arranged in a symmetric ring configuration in which two dots couple to source and drain, while the third dot interacts with a dissipative harmonic oscillator. In the absence of the oscillator, a strong detuning of the third dot leads to electron trapping and bunching. When all dots are close to resonance, by contrast, interference effects dominate. In particular, ideal destructive interference may occur, such that the current vanishes completely, even when all electronic energy levels lie within the voltage window.

It turned out that the oscillator entails two effects: First, the current minimum is found at a shifted detuning and, second, destructive interference is no longer perfect, such that always a finite current emerges. This suspension of destructive interference is also visible in the current noise measured in terms of the Fano factor. When the residual current is very small, i.e., for small decoherence, the associated shot noise is enhanced, while transport becomes almost Poissonian with stronger decoherence.

A qualitative understanding of these effects has been achieved by an analytical approximation after a polaron transformation leading to a reduced master equation for only the dot electrons. Within a standard treatment similar to the non-interacting blip approximation, we have obtained an effective master equation for the electron transport. Then it became possible to analytically obtain the current from the resulting master equation also close to destructive interference. The results agree well with the full numerical results, provided that the oscillator frequency is sufficiently large and the intra-dot tunneling is small. In turn, we can conclude that our reduced master equation faithfully describes transport effects entailed by a dissipative mode. Moreover, this picture provide evidence that the decoherence of an oscillator cat state directly turns into decoherence of the dark state.

In summary, our results underline the impact of already one phonon mode on quantum dot interferometers. With our reduced master equation for the quantum dot electrons, we have put forward a method for describing such systems efficiently after eliminating the oscillator. Such a method is in particular welcome when the oscillator is only weakly damped, since then an explicit treatment requires taking quite a few oscillator states into account.

Chapter 5

Is the Hyperfine interaction equivalent to an inhomogeneous magnetic field?

Quand on désespère de comprendre quelque chose, il est vraiment trop facile de faire intervenir la divinité.
Jules Verne

Summary

In this chapter we study the triplet-sinnglet transition mediated by the hyperfine and the electron-phonon interactions in a double quantum dot. We apply an elementary measurement scheme to have an intuitive picture of the mechanism that makes the hyperfine interaction different from an effective inhomogeneous magnetic field. The main characteristic that differentiates the hyperfine interaction from local magnetic fields is the local nuclear back-action process (flip-flop). We will see that this process is the responsible of the appearance of finite current in the spin-blockade regime. For this reason it is important to study its functional form to obtain the dynamical effects produced due to the interaction.

5.1 Introduction

In this chapter we will study the effects that the decoherence of a bath consisting of localized modes has on particular eigenstates of a system. As we introduced in the first chapter of this manuscript, transport in the spin-blockade regime is determined by the spin-flip transitions produced by the environment. These interactions are typicially, the hyperfine and the spin-orbit interactions. However, experimental results show that the hyperfine interaction is the main responsible of the triplet-singlet transitions and for this reason and also from a fundamental point of view, it deserves some atention. Special attention has been paid to the interaction between the nuclear and the electronic spins by means of the hyperfine interaction (HF) [84, 109, 26, 83, 130]. The importance of this well-known decoherence process is clearly manifest in a very known system: a double quantum dot (DQD) in the spin blockade regime (SB) [117, 79, 122, 90, 73, 71, 72, 80, 136]. There, the occupation depends on the spin degree of

freedom and sequential transport is blocked due to the Pauli exclusion principle. In this way, whenever the transport is blocked, a current may arise only when spin scattering processes such as HF interaction flips one of the electronic spins [117, 73, 71, 72], inducing the triplet-singlet transition ($T_{\pm1}$-S).

Many experiments have been performed in a lateral DQD in the SB regime. Some of them show a hysteretic behavior upon sweeping the magnetic field [122, 90]. Besides this hysteretic behavior, other experiments in the strong interdot coupling regime show how current changes radically and prominent current spikes appear tuning the in-plane magnetic field [90]. Motivated by these recent experiments, we have studied microscopically the $T_{\pm1}$-S transition probability induced by the HF interaction in a lateral DQD. The $T_{\pm1}$-S transition determines transport and serves as a basis to study the nuclear dynamical polarization, providinging the possibility to study quantitatively the current in any interdot coupling regime. The transitions could be produced by the interaction with the environment by means of the hyperfine or the spin-orbit interaction, or external magnetic fields.

Before entering into the details of the calculation of the transition rate, let us discuss some physical aspects which make the HF interaction different from other interactions such as the spin-orbit interaction or an anisotropic magnetic field. The HF interaction has two special characteristics: the first one is its local character. Thus, the electronic envelope function determines the number of nuclei which can interact with the electronic spin. Therefore, it is natural to associate an ensemble of nuclear spins to each quantum dot (N_L and N_R in Figs. 5.2 b and c). The second one is related to spin conservation. Whenever there is an electronic spin-flip transition ($T_{\pm1}$-S), the spin orientation of one nuclear spin localized in one of the two baths, N_L or N_R, is reversed. It is precisely this local change which allows one to detect in which of the dots the electronic spin flips. In analogy to the double slit experiment, we will show that the negative $T_{\pm1}$-S interference pattern is completely destroyed when the nuclear spin ensembles measure exactly in which of the dots is the spin-flip produced (Fig. 5.2b). To complete our analysis, we have considered the case where some of the nuclear spins interact with both dots (Fig. 5.2c), which occurs when the electronic wave function is extended, i.e., strong interdot coupling. As we will see, the shared bath give rise to an uncertainty in the local measurement of the spin-flip, leading to the appearance of negative interference terms proportional to the overlap of the electronic wave functions.

Considering the nuclear spin bath as a slit detector is supported by the fact that nuclear spins have no internal dynamics [42]. Estimations of nuclear spin dynamics, due to dipole-dipole nuclear spin interaction, suggest that time scales governing nuclear spin evolution ($t > 100$ms) are orders of magnitude slower than other associated with electron spin processes [109]. Thus, we consider only changes of the nuclear spin states induced by the HF interaction with the electrons. If the internal nuclear spin dynamics were not frozen, one would take them into account [26, 83, 130].

5.2 Model and Hamiltonian

5.2.1 Two electrons in a double quantum dot

The spin blockade regime is composed by triplet states in the (1,1) configuration isolated energetically from the triplet states in the (0,2) configuration. Therefore, when those triplet states become occupied transport is blocked and only transitions to the singlet state (1,1), which is coupled to singlet states (0,2), can give rise to a finite current. In order to describe the system we will use the Heitler-London approximation, used in references [18, 30] for lateral double quantum dots. Further approximations include also sp-wave functions and double occupied singlet and triplet states, known as Pfund-Mulliken, however we will use here the most simple approximation, which fits with the experimental setup. Both

extensions of the approximation are included in reference [18], and could be easily improved in our model (see AppC).

Assuming a low temperature description $kT \ll \hbar\omega_0$, beeing $\hbar\omega_0$ the parabolic confinement potential, we restrict to the two lowest orbital levels of the total Hamiltonian $H_{\rm orb}$ (see its explicit form in appendix C). In this reduced Hilbert space, the total Hamiltonian can be replaced by

$$H_s = J\mathbf{S_1}\cdot\mathbf{S_2}, \tag{5.1}$$

where $J = \epsilon_t - \epsilon_s$ is the exchange energy.

In order to obtain the eigenvalues of the Hamiltonian H we consider the Heitler-London approximation. In this approximation, one starts from single-dot ground state orbital wave functions $\phi(\mathbf{r})$ which are the displaced Fock-Darwin wave functions and combines them into the (anti)symmetric two-particle orbital state vector

$$|\Psi_\pm\rangle = \frac{1}{\sqrt{2\,(1\pm O^2)}}\left(|L(1)R(2)\rangle \pm |L(2)R(1)\rangle\right) \tag{5.2}$$

the positive (negative) sign corresponds to the spin singlet (triplet) state. Here, $\phi_{-a} = \langle r|1\rangle$ and $\phi_{+a} = \langle r|2\rangle$, denote the one-particle orbitals centered at $r = (\pm a, 0, 0)$, and $|ij\rangle$ the two-particle product states. The constant $O = \int d^2r\langle L|\mathbf{r}\rangle\langle\mathbf{r}|R\rangle$ corresponds to the overlap of the right and left orbitals, it is given by $O = \exp(-m\omega a^2/\hbar - a^2\hbar/4l_B^4 m\omega)$. The sign $+(-)$ corresponds to the singlet (triplet) state, while the numbers 1 and 2 label the electrons. The exchange energy is obtained through $J = \epsilon_t - \epsilon_s = \langle\Psi_-|H_{\rm orb}|\Psi_-\rangle - \langle\Psi_+|H_{\rm orb}|\Psi_+\rangle$ The final wave functions are given by the antisymmetric product

$$|S\rangle = \frac{1}{\sqrt{2}}\left(|\uparrow_1,\downarrow_2\rangle - |\downarrow_1,\uparrow_2\rangle\right)\otimes|\Psi_+\rangle \tag{5.3}$$

$$|T_{+1}\rangle = |\uparrow_1,\uparrow_2\rangle\otimes|\Psi_-\rangle \tag{5.4}$$

$$|T_0\rangle = \frac{1}{\sqrt{2}}\left(|\uparrow_1,\downarrow_2\rangle + |\downarrow_1,\uparrow_2\rangle\right)\otimes|\Psi_-\rangle \tag{5.5}$$

$$|T_{-1}\rangle = |\downarrow_1,\downarrow_2\rangle\otimes|\Psi_-\rangle. \tag{5.6}$$

We can now see that the orbital and spins degrees of freedom become entangled. Setting the energy of the singlet state at zero, it yields the final form of the Hamiltonian is

$$H_{\rm dqd} = J|T_0\rangle\langle T_0| + (J-\Delta_z)|T_{+1}\rangle\langle T_{+1}| + (J+\Delta_z)|T_{-1}\rangle\langle T_{-1}| \tag{5.7}$$

The energy difference J depends on the intensity of the magnetic field and on the interdot distance (see Ref. [18]).

5.2.2 Reservoirs and their interactions

Nuclear spins

For simplicity we assume that under the action of an external magnetic field, the nuclear spins will be oriented in the direction of the external field pointing up or down randomly. Under this assumption, nuclear spins can be described by the Hamiltonian

$$H = \sum_{\rm k=1}^{N}\mathbf{B}\cdot\mathbf{I}_{\rm k} + \sum_{\rm k,k'}^{N} V_{\rm k,k'}\mathbf{I}_{\rm k}\cdot\mathbf{I}_{\rm k'} \tag{5.8}$$

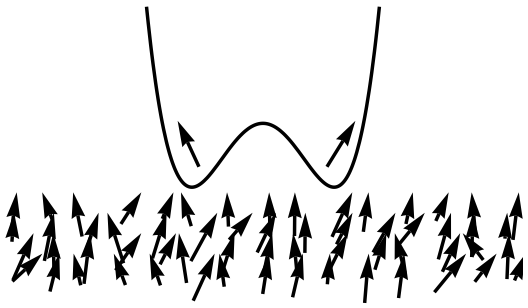

Fig. 5.1: Schema of two spins placed in a double well potential in the presence of nuclear spins.

being $\mathbf{B}$ an external magnetic field and $V_{k,k'}$ the interaction between nuclear spins. Experiments show that $V_{k,k'}$ is much weaker than the hyperfine interaction, thus, the spin bath can no longer be treated as a delocalized bath of harmonic oscillators, i.e. as the Caldeira-Legget model for this reason we will consider the spin bath as a bath of localized modes.

Taking into account that $V_{k,k'}$ is negligible we will model the nuclear spins as an independent set of spatially distributed spins up or down. It is worthy to say that although this assumption is not necessarily true, however it does not affect the main point of the final results. It just does modify the intensity of spin averages obtained below. Thus, we describe the independent set of spins by means of the wave function

$$|m_i\rangle = \prod_{k=1}^{N} |\sigma_k^z\rangle, \tag{5.9}$$

which is an eigenstate of $J_z = \sum_k I_k^z$. Here σ_k^z is the z-eigenvalue of the kth nuclear spin.

Hyperfine interaction

The hyperfine interaction of an electron spin to a single nucleus at position $\mathbf{R}$ can be seen as

$$2\mu_B\gamma_n\hbar\left(\frac{3(\mathbf{I}\cdot\mathbf{n})(\mathbf{S}\cdot\mathbf{n})-\mathbf{I}\cdot\mathbf{S}}{|\mathbf{r}\cdot\mathbf{R}|^3}+\frac{8\pi}{3}\mathbf{I}\cdot\mathbf{S}\delta(\mathbf{r}\cdot\mathbf{R})\right) \tag{5.10}$$

where $\mathbf{n} = (\mathbf{r}-\mathbf{R})/|\mathbf{r}-\mathbf{R}|$, γ_n is the nucleus magnetic moment. The first term is the coupling term between magnetic dipoles of the electron and nuclei, but the latter term, so called, contact term is a correction due to the non-zero electron density at the nucleus [25].

In GaAs, and other materials with s-orbital conduction band, the dipole-dipole term is strongly suppressed, leaving the contact term as the dominant contribution. Then, accounting the interaction to all nuclear spins ($\mathrm{N_{QD}} \approx 10^5 - 10^6$) the Hamiltonian becomes [151]

$$H_{HF} = \sum_{i=1,2}\sum_{k}^{N} A_{i,k}\mathbf{S}_i\cdot\mathbf{I}_k\delta(\mathbf{r}_i-\mathbf{R}_k) \tag{5.11}$$

where $\mathbf{S}_i$ ($\mathbf{I}_k$) and $\mathbf{r}_i$ ($\mathbf{S}_i$) denote the spin and position of the *ith* electron (*kth* nuclei). The delta function indicates that the point-like nature of the contact interaction will result in a position dependent

coupling. The tensor element $A_{i,k}$ is the Hyperfine coupling constant. In GaAs the conduction band is mainly composed of s-like wave functions, therefore we assume that all the nuclei interact with the same coupling constant. Due to possible geometrical differences between left and right dots, we will consider two different hyperfine constant couplings A_L and A_R. We transform now eq. (5.11) to the triplet-singlet basis, yielding

$$H_{HF} = \sum_{\mathrm{k}} \left(\frac{N_+}{N_-} \left[(A_R I^+_{k,R} - A_L I^+_{k,L})|S\rangle\langle T_{+1}| + (A_L I^-_{k,L} - A_R I^-_{k,R})|S\rangle\langle T_{-1}| + (A_R I^z_{k,R} - A_L I^z_{k,L})|S\rangle\langle T_0| \right] \right.$$
$$\left. + (A_R I^+_{k,R} + A_L I^+_{k,L})|T_0\rangle\langle T_{+1}| + (A_R I^-_{k,R} + A_L I^-_{k,L})|T_0\rangle\langle T_{-1}| + h.c. \right) \tag{5.12}$$

where $S^{\pm}_i$ are the raising/lowering spin operators of the electron i. The $I^{\pm}_{k,L(R)}$ are the raising/lowering of the kth nuclear spin operator, and the subscripts L and R denote in which of the dots are placed the nuclear spins. It is important to note that due to the overlap of the wave functions, there is a set of nuclear spins which can be flipped from both dots. Besides, it is implicitely assumed that the number of nuclear spins can be different so that the sums over k have in general diffent upper limits $N_{L(R)}$. The hyperfine constants A_L and A_R for the left and the right dot, respectively.

Terms containing the raising and the lowering operators describe the dynamic part of the hyperfine interaction, they are responsible for the electronic-nuclear spin-flip. On the other hand, the z-projection terms give rise to an additional Zeeman splitting, called Overhauser shift. With this in hand we replace the Dirac-delta in eq. (5.11) for a subindex in the nuclear spin vectors, denoting the region where the nuclear spin yield

In single quantum dots, the average of the nuclear spins has a typical length of 5×10^{-4}meV, which corresponds to a 100Gauss magnetic field.

Piezo-electric phonons

Vibrational excitations of the lattice are always present in mesoscopic devices and the interaction with electrons is tipically the way in which electrons transfer energy to the environment. In a GaAs quantum dot made in the [100] direction, vibrational excitations are typically domminated by the piezo-electric coupling potential

$$H_{\mathrm{ph}} = \sum_{\lambda \mathbf{k}} \hbar \omega_{\lambda \mathbf{k}} a^{\dagger}_{\lambda \mathbf{k}} a_{\lambda \mathbf{k}}. \tag{5.13}$$

5.2.3 Electron-Phonon interaction

Since we are in the low energy and temperature regimes, we will restrict to the single phonon scattering events with long wavelength acoustic phonons. The electron-phonon Hamiltonian is given by

$$V_{e-p}(\mathbf{q}) = \lambda_q e^{i\mathbf{qr}} \left(b^{\dagger}_{-\mathbf{q}} + b_{\mathbf{q}} \right), \tag{5.14}$$

where $b_{\mathbf{q}}$ and $b^{\dagger}_{-\mathbf{q}}$ are the phonon anhihilation creation operators respectively, and the coupling parameter $\lambda_{\mathbf{q}}$ depends on the mechanism of electron-phonon interaction, e.g. deformation potential or piezo-electric coupling. For low temperatures the electron-phonon interaction is dominated by the piezo-electric coupling to long-wavelength bulk (3D) acoustic phonons. For zinc blende crystal structures the coupling parameter is

$$|\lambda_{\mathbf{q}}|^2 = \frac{1}{V} \frac{1}{cq} \frac{\hbar P}{2\rho_M}. \tag{5.15}$$

In order to calculate the electron-phonon coupling one needs to reformulate the electron-phonon in the triplet-singlet basis. We see that due to the fact that the electron phonon coupling does not change the spin, we will just consider diagonal transitions, and rewrite the Hamiltonian as

$$V_{ep}(q) = \alpha_q \sum_{i=0,\pm 1} |T_i\rangle\langle T_i| + |S\rangle\langle S|\beta_q \tag{5.16}$$

where the constants α_q and β_q are given by

$$\alpha_q = \langle \Psi_-|V_{ep}(q)|\Psi_-\rangle = \langle 12|V_{ep}(q)|12\rangle + \langle 21|V_{ep}(q)|21\rangle - \langle 12|V_{ep}(q)|21\rangle - \langle 21|V_{ep}(q)|12\rangle \tag{5.17}$$

$$\beta_q = \langle \Psi_+|V_{ep}(q)|\Psi_+\rangle = \langle 12|V_{ep}(q)|12\rangle + \langle 21|V_{ep}(q)|21\rangle + \langle 12|V_{ep}(q)|21\rangle + \langle 21|V_{ep}(q)|12\rangle \tag{5.18}$$

5.3 Triplet-singlet transition

In general, the energy difference between the electronic (triplet-singlet and triplet-triplet) and the nuclear states depends on the magnetic field (see Ref. [18]). Due to the small Zeeman splitting of the nuclear spins, the energy differences between the triplet-singlet and the triplet-triplet states are for most of the range of the magnetic field intensities much higher than the difference between the spin up and down, although for some of the values of the magnetic field these two energies become comparable. Therefore we can establish two different regimes. The first regime accounts the case of $\Delta_Z^N \ll J$, $J + \Delta_z$ and $J - \Delta_z$, and the other one is when one of them is comparable to the nuclear zeeman splitting.

For the first regime we will analyze the spin-flip mediated by the electron-phonon coupling. We remind here that in order to conserve energy of the electron-nuclear system, the process needs to be mediated by the electron-phonon interaction. Since nuclear spins do not fluctuate in time, we will be able to perform average over the nuclear spins. Nevertheless, we will see below that the result of this average is different from the result of taking directly the average of the nuclear spin bath.

5.3.1 Phonon mediated triplet-singlet transition

Polaron transformation

We now perform the polaron transformation and obtain an effective liouvillian of the electronic state. As in the former chapter, the resulting displacement operator X and consequently the electron-phonon correlation function depend on the electron-phonon coupling difference. Then, taking into account that the electron-phonon coupling α_q of the triplet states is equal, it means that there will be no transitions mediated by the electron-phonon coupling between triplet states. On the other hand, the triplet-singlet transitions are coupled by the difference

$$\alpha_q - \beta_q = 2\langle L(1)R(2)|V_{ep}(q)|L(2)R(1)\rangle(1 + e^{2i\mathbf{d}\cdot\mathbf{q}}), \tag{5.19}$$

which depends on the overlap O. Therefore, by increasing the overlap of the double quantum dot we will increase the triplet-singlet transitions. We skip all the intermediate and tedious steps an we write down

the final electron-nuclear effective Liouvillian

$$\begin{aligned}\mathcal{L}_{corr}\rho_e(t) = &-\Big(C_{J+\Delta_Z}\chi^+\chi^-\hat{n}_{T_{-1}} + C_{J-\Delta_Z}\chi^-\chi^+\hat{n}_{T_{+1}} + C_J(\chi^z)^2\hat{n}_{T_0}\Big)\rho_{e,N}(t) + h.c.\\ &-\Big(C_{J+\Delta_Z}\chi^+\chi^- + C_{J-\Delta_Z}\chi^-\chi^+ + C_J(\chi^z)^2\Big)\hat{n}_S\rho_{e,N}(t) + h.c.\\ &+2\Big(\mathcal{R}\{C_J\}\chi^z|S\rangle\langle T_0|\rho_{e,N}(t)|T_0\rangle\langle S|\chi^z + \mathcal{R}\{C_{-J}\}\chi^z|T_0\rangle\langle S|\rho_{e,N}(t)|S\rangle\langle T_0|\chi^z\Big)\\ &+2\Big(\mathcal{R}\{C_{J-\Delta_z}\}\chi^+|S\rangle\langle T_{+1}|\rho_{e,N}(t)|T_{+1}\rangle\langle S|\chi^- + \mathcal{R}\{C_{-J+\Delta_z}\}\chi^-|T_{+1}\rangle\langle S|\rho_{e,N}(t)|S\rangle\langle T_{+1}|\chi^+\Big)\\ &+2\Big(\mathcal{R}\{C_{J+\Delta_z}\}\chi^-|S\rangle\langle T_{-1}|\rho_{e,N}(t)|T_{-1}\rangle\langle S|\chi^+ + \mathcal{R}\{C_{-J-\Delta_z}\}\chi^+|T_{-1}\rangle\langle S|\rho_{e,N}(t)|S\rangle\langle T_{-1}|\chi^-\Big)\end{aligned} \tag{5.20}$$

where we have defined the operators $\chi^x = \sum_{k=1}^{N}\left(A_L I^x_{k,L} - A_R I^x_{k,R}\right)$ with $x = +, -$ or z. The Laplace transformed correlation functions are C_J are the correlation functions of a bath of piezoelectric phonons, instead of a single mode. In normal space the correlation function has the form

$$C(t-t') = e^{-\Phi(t-t')} \tag{5.21}$$

$$\Phi(t) = \int_0^\infty d\omega\rho(\omega)\left[(1-\cos(\omega t))coth(\beta\omega/2) + i\sin(\omega t)\right] \tag{5.22}$$

$$\rho(\omega) = \sum_{\mathbf{q}}\frac{|\alpha_{\mathbf{q}} - \beta_{\mathbf{q}}|^2}{\omega^2}\delta\left(\omega - \omega_{\mathbf{q}}\right) \tag{5.23}$$

Taking into account that the electron-phonon coupling is small because it depends on the overlap of the wave functions we can approximate $C(t-t') \approx 1 - \Phi(t-t')$, and then integrate.

In the next paragraph we trace out the nuclear spin states assuming that the nuclear spins fluctuations are small compared to the the mean value of the quantum field.

Spin-flip probability

Here we evaluate the average over the nuclear spins in the effective Liouvillian given by eq. (5.20). We have to assume that there are no correlation functions between the nuclear spins and the electronic system and therefore the density matrices become separable, i.e. $\rho_{e,N}(t) \approx \rho_e(t)\otimes\rho_N$ [1]. We assume that the nuclear spin density matrix is a mixed state and has the form

$$\rho_N = \sum_i P_i|i\rangle\langle i| \tag{5.24}$$

Where P_i is the probability of having the state $|i\rangle$. Since they are randomly oriented we assume a gaussian distribution. We evaluate terms like

$$\sum_\mu\langle\mu|\chi^+\chi^-\rho_N|\mu\rangle = \sum_\mu\sum_{k=1}^{N}P_\mu\langle\mu|(A_L I^+_{k,L} - A_R I^+_{k,R})(A_L I^-_{k,L} - A_R I^-_{k,R})\chi^-|\mu\rangle$$

[1] In contrast to the Born approximation the nuclear spin density matrix depends on time because the nuclear bath keeps the number of times that the electron spin has fliped

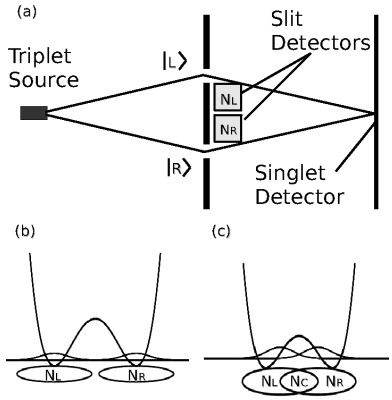

Fig. 5.2: (a) Spin Blockade regime shown in the scheme of the double slit experiment. Schematic drawn of the atomic envelope functions of a DQD in the (b) weak, (c) strong coupling regimes.

Getting rid momentanly of the sum over μ and defining

$$|\mu_{L(R)}\rangle \equiv \sum_{k=1}^{N_{L(R)}} I^{+}_{L(R),k}|\mu\rangle, \tag{5.25}$$

as a linear combination of nuclear states, where one of the initial nuclear states of the $L(R)$ dot has been flipped from $\downarrow$ to $\uparrow$, i.e. $N_{R(L),\downarrow}$. We can recast the average values as

$$\langle\mu|\chi^{+}\chi^{-}\rho_N|\mu\rangle = P_\mu\left(\langle\mu_L|\mu_L\rangle + \langle\mu_R|\mu_R\rangle - \langle\mu_L|\mu_R\rangle - \langle\mu_R|\mu_L\rangle\right) \tag{5.26}$$

where the products $\langle\mu_{L(R)}|\mu_{L(R)}\rangle$ and $\langle\mu_{L(R)}|\mu_{R(L)}\rangle$ have an easy interpretation. The first product accounts for the probability that the electron has to flip in the left (right) dot. The second product is the probability that the electron has to flip a nuclear spin in the right (left) region when it is placed in the left (right) dot. The existence of the overlap between the electronic wave functions implies that both electrons can interact with a common ensemble of nuclear spins at the same time. Thinking in terms of detectors, we would say that the existence of the shared bath gives rise to an uncertainty in the localization of the electronic spin-flip. Thus, the higher $N_{C,\downarrow}$, the less reliable the spin-flip detectors and the more pronounced the negative interference term.

It is important to realize that replacing initially the hyperfine interaction by a local magnetic field, yields to a different probability rate. In that case one could obtain the cancellation of the transition in the case that the left and right effective fields are equal. However, in our case it is imposible that the probability yields a zero result because the the interference term is always lowered by the overlap of the wave functions.

Using eq. (5.12) we can calculate directly the product $\rho = V_{HF}|\Psi\rangle\langle\Psi|V_{HF}$. Finally we have to carry out the projection on the final nuclear (nuclear trace out) and electronic (singlet) states. Before presenting the general results, it is convenient to evaluate first scalar products involved in the nuclear trace

$$\sum_{k=1}^{N}\langle m_{f,k}|M_i\rangle\langle M_j|m_{f,k}\rangle = \langle M_i|M_j\rangle, \tag{5.27}$$

for i and j equal to L and R. First of all, we evaluate the case $i = j$. Due to orthogonality, the projection of each component of state (5.25) contributes to the total scalar product with unity, if two equal components are projected, and zero otherwise. With this in mind it is easy to calculate

$$\langle M_{L(R)}|M_{L(R)}\rangle = N_{L(R),\downarrow}. \tag{5.28}$$

Finally, we replace the obtained expressions (5.27) and (5.28) into the nuclear spin bath of eq. (5.20), yielding

$$\mathcal{P}_{T_{\pm 1}\to S} = \frac{1}{2}D\left(B^2\frac{N_{R,\downarrow(\uparrow)}}{N_R^2} + A^2\frac{N_{L,\downarrow(\uparrow)}}{N_L^2} - 2AB\frac{N_{C,\downarrow(\uparrow)}}{N_L N_R}\right) \tag{5.29}$$

$$\mathcal{P}_{T_0\to S} = D\left(B^2\frac{N_{R,\downarrow(\uparrow)}}{N_R^2} + A^2\frac{N_{L,\downarrow(\uparrow)}}{N_L^2} - 2AB\frac{N_{C,\downarrow(\uparrow)}}{N_L N_R}\right), \tag{5.30}$$

where we have used $D = \left(1+O^2\right)/\left(1-O^2\right)$. Equation (5.30) is the main result of our work. It is composed by three terms, the first two arise due to the contribution of the nuclear spins of each dot which are able to flip the electronic spin, while the third one arises due to the uncertainty in the measurement of the spin-flip position ($N_{C,\downarrow}$), caused by the overlap of the electronic wave functions. We observe a change the tunnel interdot on the interference pattern. In the weak-coupling regime, the interference tends to zero since the overlap is negligible ($O^2 \to 0$). In this case, nuclear detectors are perfectly reliable and thus the interference term of eq. (5.30) is cancelled [73, 71, 72]. On the other hand, in the strong-coupling regime the overlap is not negligible and an uncertainty in the spin-flip position arises and leads to the appearance of a negative interference pattern. It must be noted the fundamental difference between the HF interaction and the effect of an inhomogeneous magnetic field, in the case of the inhomogeneous magnetic field the interference pattern holds, leading to a probability which depends on the difference between the in-plane effective magnetic fields of each dot [80].

Let us extend our analysis to the transition rates between the triplet states $T_{\pm 1}$ and T_0. It yields a similar expression as (5.30), except for D which becomes one, and the negative sign of the interference pattern which becomes positive. On the other hand, the states T_0 and S are mixed due to the difference between the Zeeman splittings within each dot, i.e., due to the magnetic field anisotropy [70].

5.4 Current

In order to show how the obtained transition rate (5.30) determines a measurable quantity as the current, we analyze transport in the strong interdot coupling regime by means of a simple model. We focus on the following transport configuration: zero detuning, low in-plane magnetic field and strong interdot coupling, we consider the schematic picture of the different spin-flip transitions depicted in Fig. 2 [90]. At this experimental conditions, the energy difference between the T(1,1) and S(1,1) (T_0 and $T_{\pm 1}$) states is larger than the nuclear Zeeman splitting. Therefore, at low temperatures only transitions $T_{\pm 1}$-S and $T_{\pm 1}$-T_0 involving phonon emission are efficient [39].

We calculate the stationary current through the DQD based in a model presented in reference [80]. Within a density matrix formalism, considering the electron reservoirs within Markov approximation. The system involves seven diagonal matrix elements: three triplet states $T(1,1)$, two singlet states $S_{++} = \frac{1}{\sqrt{2}}\left(S(1,1)+S(0,2)\right)$ and $S_{--} = \frac{1}{\sqrt{2}}\left(S(1,1)-S(0,2)\right)$ and two single occupied states. Here we use (n,n') to specify the extra number of electrons in the left and right dot respectively. Additionally, it involves six non-diagonal matrix elements, corresponding to the coherences between the singlet states S_{++}, S_{--} and the triplet $T_0(1,1)$ states, which are mixed by the anisotropy of the Overhauser field (ΔB_z). We calculate

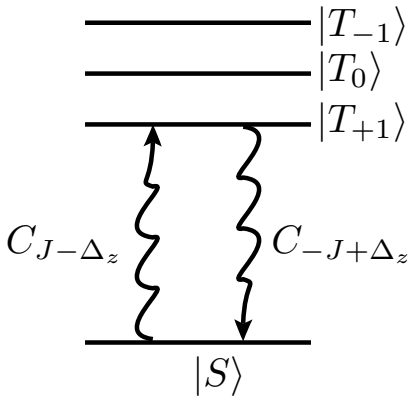

Fig. 5.3: Transport window schema of a DQD in the sharp transport regime. The dashed arrows represent spin-flip phonon assisted transitions, while the double arrows represent coherent couplings due to the inhomogeneous Overhauser field.

the stationary current making the time derivatives equal to zero. Aiming at simplicity, the triplet states T(1,1) and the extended singlet state S_{++} are coupled to the left lead while S_{++} and S_{--} are coupled to the right, by means of the coupling constant Γ. The current is proportional to the occupation of the state S(0,2) and can be calculated analytically for the general case. The general solution is quite lengthy but it can be simplified assuming that $\Delta B_z \ll E_S - E_T$ and that the transition rate Γ is orders of magnitude higher than the spin-flip rates, yielding

$$I = \frac{7\beta\delta(\alpha+\delta)}{6\beta\delta + 2\delta(3\delta+2\alpha) + 2\alpha\beta}, \tag{5.31}$$

where α and β represent the inelastic transition rates $T_{\pm1}$-S, while δ represents the rates $T_{\pm1}$-T_0. Obviously this simple model does not attempt to explain quantitative experimental evidences [90], but it is illustrative in order to show how the current is governed mainly by the transition rates $T_{\pm1}$-S and $T_{\pm1}$-T_0 (5.30). To obtain a more detailed model one has to study the time evolution accounting for the dynamical polarization of the nuclear spin ensembles, which is responsible for current bistability among other non-linear effects [73, 71, 72].

5.5 Conclusions

We have presented a microscopic model to describe the triplet-singlet and triplet-triplet transition probabilities mediated by the HF interaction in a DQD. We have stressed the importance of the local character and the nuclear flip-flop process of the HF interaction. These characteristics lead to a partial cancellation of the interference pattern, which can be intuitively seen by means of an analogy between the triplet-singlet transition and the double-slit experiment. With this picture in mind, we have shown the fundamental difference between the transition mediated by the hyperfine interaction and an anisotropic magnetic field. The transition under study turned out to be relevant in the spin blockade regime. The obtained results will serve as a basis to study transport accounting for the nuclear spin dynamical polarization and will open the possibility to explain experiments covering different tunneling coupling regimes.

Part II

Majorana fermions in a quantum wire

Chapter 6

Majorana fermions in a nutshell

You see, the point is that the strongest man in the world is he who stands most alone.
H. J. Ibsen

Summary

The last part of this thesis is dedicated to the study of the dynamical detection of Majorana fermions in a finite quantum wire. This topic breaks with the previous part of the thesis, and therefore, before entering into the details of our study it seems convenient to present a brief introduction about what Majorana fermions are, which properties do they have, how they might appear in condensed matter devices, and how can be detected. For a further and more formal overview of the topic I recommend the reviews [7] and [2], and the introduction to the topic in Ref. [99], where one can also find most of the relevant references. Afterwards, we abandon the general frame to show a concrete microscopic derivation of the appearance of Majorana fermions in a solid state device, i.e. a quantum wire, where "easy interactions" such as spin-orbit coupling, magnetic field and s-wave superconductivity are combined to give rise to this non-trivial state. This section basically reproduces the previous proposals [104, 118] and constitutes the base of the system of our contribution. Finally, in the next chapter I will present the analysis of the current biased Shapiro experiment in the presence of Majorana bound modes. There, we take into account finite size effects, extra Andreev modes and also quasiparticle poisoning. We will see that this method of detection is rather robust against these effects.

6.1 Past and present of Majorana fermions

Quantum electrodynamics can be deduced by quantizing a system of equations which include the Dirac wave equation for the electron and the Maxwell equations. They contain terms of different types. On the one side, the electromagnetic potentials can be given in a classical interpretation, within the limits posed by the correspondence principle. On the other side, there are matter waves, which represent particles obeying the Fermi statistic, and which have only quantum interpretation. In this respect, Majorana found unsatisfactory that the equations as well as the whole quantization procedure have to be derived from a variational principle which can be given only by a classical interpretation. Therefore, in 1937 he derived [107] the Maxwell-Dirac equations from quantum electrodynamics using a non-commutative variational principle. From his theory an elementary neutral fermion should arise in

nature; the Majorana fermion. This fermion has the special property of presenting its creation operator equal to the annihilation operator, that is

$$\gamma^\dagger = \gamma. \tag{6.1}$$

These operators fulfill the fermionic anticommutation relation

$$\{\gamma, \gamma^\dagger\} = 2\gamma^2 = 2\gamma^\dagger\gamma = 2 \Rightarrow \gamma^\dagger\gamma = 1 \text{ and } \gamma\gamma^\dagger = 1, \tag{6.2}$$

meaning that the level is always filled and empty at the same time. In this situation we say that the state is half-filled [77]. Then, plugging eq. (6.1) into the charge operator

$$\hat{Q} = \frac{1}{2}\int dr \left(\gamma^\dagger\gamma - \gamma\gamma^\dagger\right), \tag{6.3}$$

we find that the property that Majorana fermions have no charge, i.e. $\hat{Q} = 0$. Moreover, they do neither have spin nor mass. The combination of these lack of properties makes a very difficult task to detect them. For historical reasons, Majorana fermions were searched among the high energy particles. In this field, the neutrino is the best candidate of being a Majorana fermion. If this were the case, it could be possible to have a neutrinoless double-beta decay [69]. Nevertheless, untill now this experiment has not been yet confirmed. During the last decades the search of these particles has been extended to condensed matter, where Majorana fermions naturally occur in half-vortices of chiral p-wave superconductors [168]. In fact, Majorana Fermions (MFs) have recently been predicted to occur in a multitude of condensed-matter systems [168, 111, 129, 86, 51, 104, 118, 24]. In contrast to those expected to appear in high energy physics, Majorana fermions in condensed matter physics are not fundamental particles, its components are ordinary electrons and ions. Indeed, they can interact with the electromagnetic field even though they are neutral. This happens due to the fact that the phases of the superconducting order parameter enter into the relation between the electron operator and the Majorana fermion.

We briefly remark here that the interest in MFs stems not only from the fundamental point of view but also from the non-Abelian quantum statistics which forms the basis of topological quantum computation [111, 76, 86, 114].

Dirac equation was introduced to make the Schrödinger equation invariant under Lorentz transformations. The equation takes the form

$$\left(\sum_{i=1}^{3}\alpha_i p_i + \beta c^2 m(r)\right)\psi = i\frac{d}{dt}\psi, \tag{6.4}$$

where α and β are 4×4 Dirac matrices, p_i and m are the mass and momentum of the particle, and c is the speed of light. This first order differential equation can be assimilated as a square root of a Laplacian, and therefore it presents solutions $E > 0$ and $E < 0$. Dirac gave the interpretation of the equation in terms of a many body system. He proposed a vacuum where the solutions $E > 0$ are unfilled, while for $E < 0$ are filled. The constant m produces an energy gap between $E > 0$ and $E < 0$, and this can be seen as the mass of the excitation. When the mass has a position dependence, i.e. $m(r)$, zero energy solutions, $E = 0$, can be isolated. These solutions are known as mid-gap states and they present the peculiar property of having a half filled nature.

Linear dispersion Hamiltonians fulfill the same properties as the Dirac Hamiltonian, and for this reason they have adopted the same name. Well known examples of linear dispersion relation appear

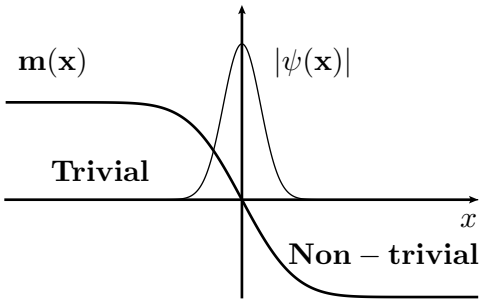

Fig. 6.1: The solid line represents the mass of a 1D system. When $m(x) > 0$ the system is trivial while the negative corresponds to a non-trivial part. When the mass is exactly equal to zero, the wave function becomes real and a Majorana fermion arises. The thinner solid line represents the absolute vale of the Majorana wave function cleaved at the domain wall of the mass.

at the low energy in condensed matter, such as graphene and topological insulators. In one dimensional systems they can be generally written as

$$H = -i\hbar v\sigma_z \frac{\partial}{\partial x} + m(x)\sigma_y, \tag{6.5}$$

where $m(x)$ represents the spatial dependent mass and v the velocity of the particle. The solution for the eigenenergy $E = 0$ of the differential equation is

$$\psi(x) = \exp\left(\sigma_x \int_{x_0}^{x} dx' \frac{m(x')}{\hbar\nu}\right)\psi(x_0) = \exp\left(\pm \int_{x_0}^{x} \frac{m(x')dx'}{\hbar\nu}\right)\begin{pmatrix}1\\ \pm 1\end{pmatrix}. \tag{6.6}$$

At most one of the solutions is normalizable, and it is only possible to find a solution if the mass has opposite signs at $x \to \pm\infty$. Consequently, when the mass term crosses zero, and the wave function turns to a Majorana bound state. Thus, the presence of this bound state depends only on the presence of the domain wall and not on the form of $m(x)$.

6.2 Majorana fermions in condensed matter

Regarding symmetry properties of the system one can obtain the minimal condition that the system needs to satisfy to be able to have a Majorana fermion. We know that the particle-hole symmetry ($\mathcal{C}$) transforms the state $|\varphi\rangle$ of energy ϵ into the state $\mathcal{C}|\varphi\rangle$ with energy $-\epsilon$. It is interesting to note that when $\epsilon = 0$, the particle-hole symmetry transforms the state into itself. Therefore, in order to host Majorana fermions, the system has to fulfill at least the particle-hole symmetry.

In the region of validity where the mean field approximation describes correctly the s-wave superconductor state, the Bogolubov-de Gennes equations can be interpreted as a one particle wave equation [29]. This non-interacting view of the BCS Hamiltonian is performed by including the hole states and therefore doubling Hilbert space of the system. For this reason, the solutions are not independent and the eigenstates of the BdG Hamiltonian come in pairs, i.e. if $(u_k, v_{-k})^T$ is the solution of the BdG equations with energy ϵ, then, $(-v_k^*, u_{-k}^*)^T$ is the solution with eigenvalue $-\epsilon$, indicating that both eigenstates represent the same quasiparticle. The creation operator is given by

$$\gamma_{k\uparrow}^\dagger = u_k c_{k\uparrow}^\dagger - v_k c_{-k\downarrow}. \tag{6.7}$$

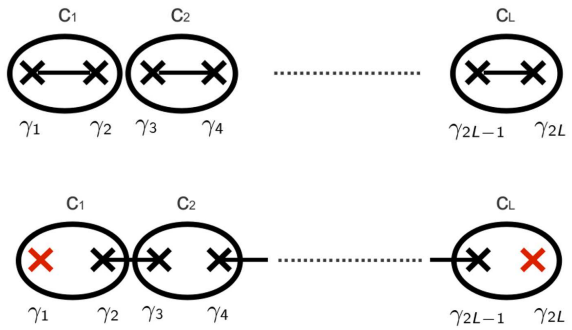

Fig. 6.2: Two different possibilities of pairing between Majorana fermions, represented by crosses. When the pairing is intra-site (top), the system presents a trivial character. On the other hand, when the pairing is inter-sites (bottom) two Majorana fermions (red crosses) become isolated at the extremes of the system.

From the form of this operator, we realize that removing spin and making $v_k^* = u_k$, the field operators γ can fulfill the Majorana fermion equation $\gamma^\dagger = \gamma$. These conditions are given when we break the time reversal and spin rotation symmetries, that is, in a spinless p-wave superconductor [167, 129, 85]. The most easy example can be found in one-dimensional Hamiltonian presenting spinless p-wave superconductivity [85]

$$H = \sum_j \left[-w(c_j^\dagger c_{j+1} + c_{j+1}^\dagger c_j) - \mu \left(c_j^\dagger c_j - \frac{1}{2} \right) + \Delta \left(c_j c_{j+1} + c_{j+1}^\dagger c_j^\dagger \right) \right], \tag{6.8}$$

where w is the hopping amplitude, μ the chemical potential and Δ is the superconducting gap, which for simplicity we have assumed here that it is a real number. In general, one can always reformulate the Hamiltonian in terms of Majorana operators, that is, operators which fulfill eq. (6.1), yielding

$$H = \frac{i}{2} \sum_j \mu \gamma_{2j-1} \gamma_{2j} + (w + \Delta) \gamma_{2j} \gamma_{2j+1} + (-w + \Delta) \gamma_{2j-1} \gamma_{2j+2}, \tag{6.9}$$

where we have used $c_j = 1/2(\gamma_{2j+1} + i\gamma_{2j})$. It can be easily verified that when the parameters w, Δ and μ fulfill some topological conditions, two Majorana fermions are isolated at the extremes of the wire. We show here the most easy example: when $\Delta = w > 0$ and $\mu = 0$, equation (6.9) yields

$$H = w \sum_j \gamma_{2j} \gamma_{2j+1}. \tag{6.10}$$

By simple substitution of the subindex j, we can easily check that the Majorana fermions placed at the extremes, i.e. γ_1 and γ_{2L}, remain unpaired. This fact resembles the nonlocal encoding of a normal fermion. An illustration of this phenomena is plotted in Fig. 6.2. The upper plot shows a 1D system where the pairing is given intra-site MFs, leading to a trivial character. In contrast, the figure at the bottom represents the non-trivial phase, where the pairing is given inter-sites, leaving the MFs at the edges unpaired (red crosses).

Despite of the simplicity of the presented model, the proposals given were left as toy models. This happened due to the doubtfully existence of the p-wave superconductivity among the current superconductor materials. Later on, in 2008 appeared the seminal work by Fu and Kane [51], where it

was shown that the p-wave superconductivity can be effectively obtained from an ordinary s-wave superconductivity by removing degeneracies, i.e. spin-rotation and time reversal, by using the spin-orbit interaction and a magnetic field. As the superconducting gap passes through zero, Majorana fermions emerge as zero modes bound to magnetic or electrostatic defects. The closing and reopening of the gap is a topological quantum phase transition, and it can be characterized by the sign of the gap ($\mathcal{Q}$). We call that the system has a trivial phase when the gap is positive ($\mathcal{Q} = 1$), while non-trivial when the gap is closed and reopened with opposite sign ($\mathcal{Q} = -1$), and therefore supports Majorana modes. Obviously, the role played by the position dependent mass in eq. 6.5. is the same as the role played by the superconducting gap in these equations. Finally in 2010, appeared the most simplified proposal in two different works [104, 118]. It is remarkable that this proposal served as a set-up for the first experimental trials of the measurement of the Majorana fermion [113, 132, 134].

6.3 Measurement

In contrast with other zero energy states, where an electric field shifts the state from the ground state, a Majorana bound state can not be removed by means of a local perturbation (topologically protected). This occurs due to the fact that the particle-hole symmetry requires the spectrum to be $\pm E$ symmetric, and in case that there is a zero energy mode it remains protected by this symmetry. Only the interaction with another Majorana fermion can move them from the zero energy. This property protects the Majorana fermion not only against decoherence but also from being measured. For this reason, a huge effort has been devoted to design experiments where signatures of Majorana fermions appear in measurable quantities of the system.

In this section we briefly present two ways of measuring the Majorana mode: tunnel spectroscopy and fractional Josephson effect. These techniques have been used for the first trials in the measurement of Majorana fermions [113] and [134] respectively. There are more ways of measuring the Majorana bound mode but it is not the purpose of this brief introduction to go into details of all the possible techniques. As mentioned above, further details can be found in the review [7]. Just to mention them, signatures of Majorana fermions appear at quantized thermal conductance [174, 1], shot-noise [1], Andreev-reflection [96, 45], and the non-local tunneling [115, 96, 50, 9].

6.3.1 Tunnel spectroscopy

Signatures of Majorana fermions could be directly read using tunnel spectroscopy. Resonant tunneling into a Majorana bound state induce resonant Andreev reflections from the lead to the grounded superconductor. At zero bias, the linear tunneling conductance is $2e^2/h$ when there is a Majorana bound mode [96], while without this state the tunneling conductance vanishes (see left pannel of Fig. 6.3). Therefore, in the presence of a Majorana mode one should observe a zero bias voltage peak [13, 96]. Indeed, very recently, first experiments appeared in the literature [113] showing conductance peak at zero bias voltage. In figure 6.4, we can see the experimental setup (left pannel) and the results of the differential conductance as a function of the bias voltage for different values of magnetic field (right pannel). At the center of the curves we can differentiate the appearance and dissapearance of a zero bias peak as a function of the magnetic field. This curve together with other experimental evidences show what it seems to be the first observed signatures of the existence of Majorana fermions. However, this zero-bias anomaly could be obscured by other zero-bias resonances at small nonzero bias voltage [45]. For this reason, different and more robust proposals were needed. One of this proposals consists

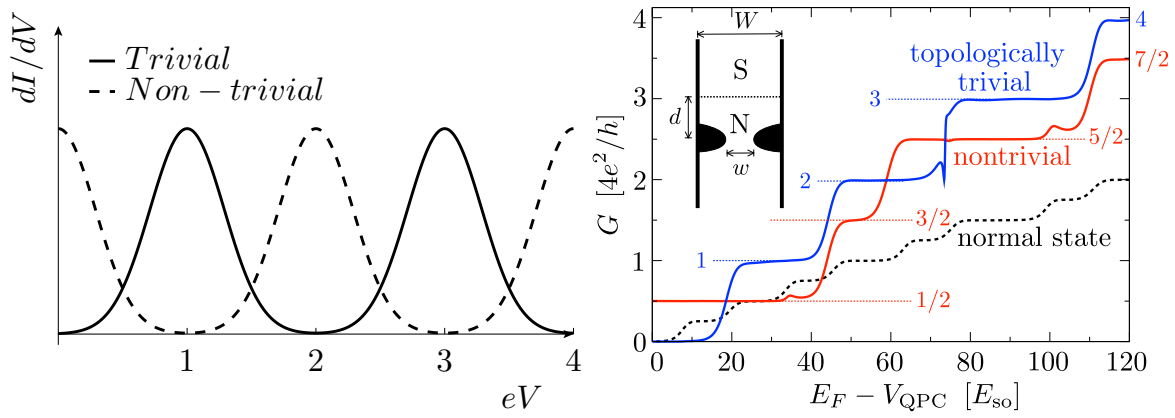

Fig. 6.3: Left pannel: dI/dV versus voltage, theoretical results in a tunnel spectroscopy experiment [96] at two different situations, in the presence (absence) of a Majorana bound mode which corresponds to the dashed (solid) curve. Right pannel: conductance of a ballistic NS junction, with the superconductor in a topologically trivial or non- trivial phase. The dotted curve is for an entirely normal system. The point contact width is varied by varying the potential V_{QPC} inside the constriction at constant Fermi energy E_F. The dotted horizontal lines indicate the shift from integer to half-integer conductance plateaus upon transition from the topologically trivial to nontrivial phase.

on measuring the quantized conductance placing a quantum point contact in a normal region attached to the topological superconductor [173]. In this situation the quantized conductance shows plateaus at values

$$G_p = \frac{4e^2}{h} \begin{cases} p & \text{if } \mathcal{Q} = 1 \\ \\ p + 1/2 & \text{if } \mathcal{Q} = -1. \end{cases} \tag{6.11}$$

where $\mathcal{Q}$ represents the sign of the topological gap (see right pannel of Fig. 6.3). It has been calculated [173] that the measurement of the plateau is rather robust against disorder.

6.3.2 Fractional Josephson effect

Signatures of Majorana fermions can be also be measured using a Josephson junction, by measuring what is called the fractional Josephson effect [85, 94, 52, 155, 104, 118, 75, 95, 163]. Physically, this effect is produced by the fact that in the presence of a Majorana bound mode, the supercurrent through a Josephson junction carries single electrons instead of the usual Cooper pairs. Thus, this fractional Cooper pairs affect the supercurrent by turning it from $\sin(\varphi)$ to $\sin(\varphi/2)$. An experiment capable of measuring the phase dependence would be able to provide a proof of the existence of a Majorana fermion. For this reason, the Shapiro experiment could be used to detect MF, due to the fact that the experiment allows the deduction of the periodicity of the current-phase relation of the junction [158, 147]. Shapiro-steps have been analyzed theoretically for voltage-biased Majorana wires [78, 139, 123]. However, the more experimentally realistic current-biased experiment [158] remains unexplored, and this is exactly what it will be analyzed theoretically in the next chapter. In fact, this year appeared the first experiments where Shapiro steps are measured in a junction which may host Majorana fermions [134]. Preliminary results

show some signatures that could point in the direction of a fractional Josephson effect. Remarkably, the results coming from the model we have used, could help in the understanding of this experiment [33].

6.4 Majorana fermions in a quantum wire

In this section we present a concrete microscopic model of a quantum wire where p-wave superconductor arises from a s-wave one. Basically, we present the derivation of the proposal given in refs. [104, 118], and constitutes the base of the effective model used in the next chapter. Therefore, we consider an important issue to know the details of the system.

The system consists of a quantum wire in contact with a s-wave superconductor. The superconductor confers a pairing gap to the wire by proximity effect. Then, Cooper pairs moving along the wire feel the spin-orbit interaction due to the wire material and an external magnetic field. The sum of these interactions break spin-rotation and time reversal symmetries, thus degeneracies are removed and Majorana modes may arise.

6.4.1 Hamiltonian and the Bogolubov-de Gennes equations

Quantum wire with spin-orbit interaction and magnetic field— The material of the wire is selected to have a strong spin-orbit interaction as it has been proposed [104, 118]. In the following we will assume that the induced occupation of the wire approaching the superconductor can be controlled by a gate voltage, so that just one band is occupied. Nevertheless, this restriction is not strong, and just serves to keep the microscopic model as simple as possible. In this situation, the wire can be represented by a 1D Hamiltonian, given by

$$H_{qw} = \int dx \sum_{\mu,\nu} \Psi^{\dagger}_{\mu}(x) \left[\frac{1}{2m} \left(\mathbf{p} - e\mathbf{A} \right)^2 \delta_{\mu,\nu} + \Delta_x \sigma_x + \alpha k \sigma_z \right] \Psi_{\nu}(x) \tag{6.12}$$

where we have used $\Psi_{\mu}(x) = \sum_k e^{ikx} c_{k,\mu}$, and $\mu, \nu = \uparrow, \downarrow$ are spin index. Besides, we have used $\Delta_x = g\mu_B B$, beeing B the magnetic field intensity. For the sake of simplicity we have chosen the first mode of the wire, the Rashba term to be in the z direction and the magnetic field in the x direction.

Proximity effect and BCS Hamiltonian— When there is a good electrical contact between a superconductor and a normal metal, Cooper pairs can diffuse into the normal region. Algebraically, this means that the pairing extends to a rather long distance ξ_N ($\xi_N \approx \hbar v_F / kT$ if N is a pure metal). This phenomena is known as proximity effect. Qualitatively the induced pairing decays exponentially with the distance as

$$\frac{\Delta(x)}{\Delta_0} = d(x) T_j \exp\left(-x/\xi_N\right), \tag{6.13}$$

where $d(x)$ is the density of states of the metal factor the density of states of the superconductor, T_j is the transmission coefficient at the boundary for an electron at the Fermi surface. The induced superconducting Hamiltonian is then given by

$$H_{BCS} = i \int dx \sum_{\mu,\nu} \Delta(x) (\sigma_y)_{\mu,\nu} \Psi^{\dagger}_{\mu}(x) \Psi^{\dagger}_{\nu}(x) + \Delta^*(x) (\sigma_y)_{\mu,\nu} \Psi_{\mu}(x) \Psi_{\nu}(x), \tag{6.14}$$

where $\Delta(x)$ is the pairing energy. The sum of both Hamiltonians lead to the description of the whole system, i.e. $H = H_{qw} + H_{BCS}$.

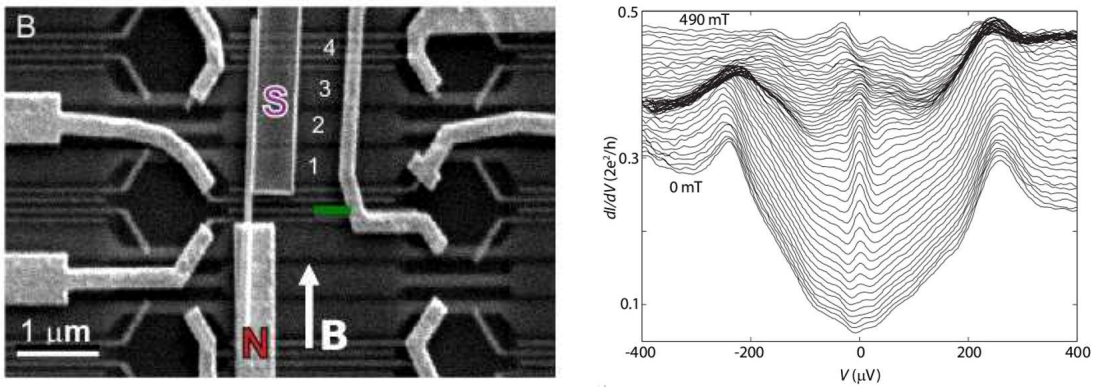

Fig. 6.4: Left pannel: Scanning tunnel microscopy image of the experimental setup. Right pannel: dI/dV vs. voltage for different values of the magnetic field intensity, going from 0 up to 490 mT.

Bogolubov-de Gennes equations— As we have mentioned above, in order to reduce the many body system to a single particle problem, it is needed to double the space by introducing the interaction between electrons and holes. The target is to diagonalize the Hamiltonian, in such a way that the Hamiltonian yields

$$H = E_g + \sum_N \epsilon_N \gamma_N^\dagger \gamma_N, \tag{6.15}$$

where E_g is the energy of the ground state and ϵ_N is the energy of the excitation N. The transformation reads

$$\Psi_\mu(x) = \sum_{N=\{n,\nu\}} \left[u_{n,\mu} \gamma_N + v_{n,\mu}^* \gamma_N^\dagger \right], \tag{6.16}$$

where the sum over N includes both the translational and spin quantum numbers, n and ν, respectively. And the operators γ and $\gamma^\dagger$ still satisfy the fermion anticommutation relations. Therefore, using eq. (6.15) we can write the anticommutation relations

$$[H, \gamma_N] = -\epsilon_N \gamma_N \text{ and} \tag{6.17}$$

$$\left[H, \gamma_N^\dagger\right] = \epsilon_N \gamma_N^\dagger. \tag{6.18}$$

To derive the equations that fix u and v, we calculate the commutator $[H, \Psi]$ by using the commutation properties of Ψ, leading to

$$[\Psi_\nu(x), H] = \frac{1}{2m} \left(\mathbf{p} - e\mathbf{A}\right)^2 \Psi_\nu(x) + \sum_\mu U_{\mu,\nu}(x) \Psi_\mu(x) + \Delta(x) \rho_{\mu,\nu} \Psi_\mu^\dagger(x). \tag{6.19}$$

Now, we replace eq. (6.16) into the rhs of eq. (6.19), and eqs. (6.18) into the lhs. Finally, comparing the coefficients of γ_N on the two sides of the equation, we obtain the Bogolubov-de Gennes equations

$$\epsilon u_\mu(x) = \frac{1}{2m} \left(\mathbf{p} - e\mathbf{A}\right)^2 u_\mu(x) + \sum_\nu U_{\mu,\nu} u_\nu(x) + \Delta(x) i(\sigma_y)_{\mu,\nu} v_\nu(x) \tag{6.20}$$

$$-\epsilon v_\mu(x) = \frac{1}{2m} \left[\left(\mathbf{p} - e\mathbf{A}\right)^2\right]^* v_\mu(x) + \sum_\nu U_{\mu,\nu}^* v_\nu(x) + \Delta^*(x) i(\sigma_y)_{\mu,\nu} u_\nu(x), \tag{6.21}$$

There are four equations, two for $u_{\uparrow\downarrow}$ and two for $v\uparrow\downarrow$. We have used the spin dependent interaction $U = \Delta_x\sigma_x + \alpha k\sigma_z$, beeing Δ_x the Zeeman splitting produced by the magnetic field and α the Rashba coupling constant. Then, substituting the former Hamiltonian into the Bogolubov-de Gennes Hamiltonian leads to

$$H = \left(\frac{p^2}{2m} - \mu\right)\tau_z + \alpha p\sigma_z\tau_z + \Delta_x\sigma_x + \Delta\tau_x \tag{6.22}$$

written in the basis $[u_\uparrow, u_\downarrow, v_\downarrow, v_\uparrow]$. As we mentioned above, the Hilbert space is doubled to take into account the interaction between electrons and holes. Mathematically this is done by introducing the tensor product between the electron and hole Pauli matrices σ and τ respectively. The tensor product is defined as

$$\sigma_i \otimes \tau_j = \begin{pmatrix} (\tau_j)_{1,1}\sigma_i & (\tau_j)_{1,2}\sigma_i \\ (\tau_j)_{2,1}\sigma_i & (\tau_j)_{2,2}\sigma_i \end{pmatrix}. \tag{6.23}$$

When just one of the matrices appear the other one is the identity.

6.4.2 Bulk spectrum

We diagonalize the BdG Hamiltonian and then, obtain the bulk spectrum for different values of μ, Δ_x, α, and Δ (see Fig. 6.5). In this figure we can observe separately the role of the different interactions. We start representing in Fig. 6.5(a) the spin degenerate dispersion relation of the first mode. We see the typical parabolic dispersion relation. Then, in Fig. 6.5(b) we switch-on the Rashba spin-orbit interaction and observe a k-spin splitting, that is, the spin-orbit interaction removes the spin-rotation symmetry. The splitting is given by the spin-orbit wave length k_{so}. Moreover, we next apply an external magnetic field perpendicular to the direction of the spin-orbit coupling, which removes the time reversal symmetry by opening a gap between the two parabolic bands (see Fig. 6.5(c)) . The strongest effect of the magnetic field is given at $k = 0$, where the spin-orbit interaction has no effect.

In the next step, we include the electron-hole symmetry by switching-on the superconducting gap provoking the interaction of electrons and holes. The main effects are given at the Fermi wave length k_F, which for $\mu = 0$ is obtained from $E(k_F) = 0$, that is

$$k_F = \sqrt{2k_{so}^2 + \sqrt{4k_{so}^4 + k_x^4}}, \tag{6.24}$$

where $k_{so} = m\alpha/\hbar^2$ and $k_x = \sqrt{2\Delta_x m/\hbar}$. There are two limiting cases depending on the relative intensities of the magnetic field and the SOI. $k_F \simeq 2k_{so}$ and $k_F \simeq k_x$.

As in the previous figure, we add the spin-orbit interaction (b) and the magnetic field (c) to the wire, this time, in the presence of superconductivity. The competition of all these interactions allow to close the gap at $k = 0$ (see fig. 6.6). As we have mentioned above, to close the excitation gap, followed by its reopening with oposite sign is a topological phase transition. Thus, the sign of the gap characterizes the topology of the system. When the sign is negative the character of the system is non-trivial, while for a positive sign the character is trivial. The size of the gap at k=0 is given by the expression,

$$E_{gap} = |\Delta_x| - \sqrt{|\Delta|^2 + \mu^2}. \tag{6.25}$$

From this expression we can extract the value at which the chemical potential closes the gap at $k = 0$, yielding a critical value

$$\mu_c = \sqrt{\Delta_x^2 - \Delta^2}. \tag{6.26}$$

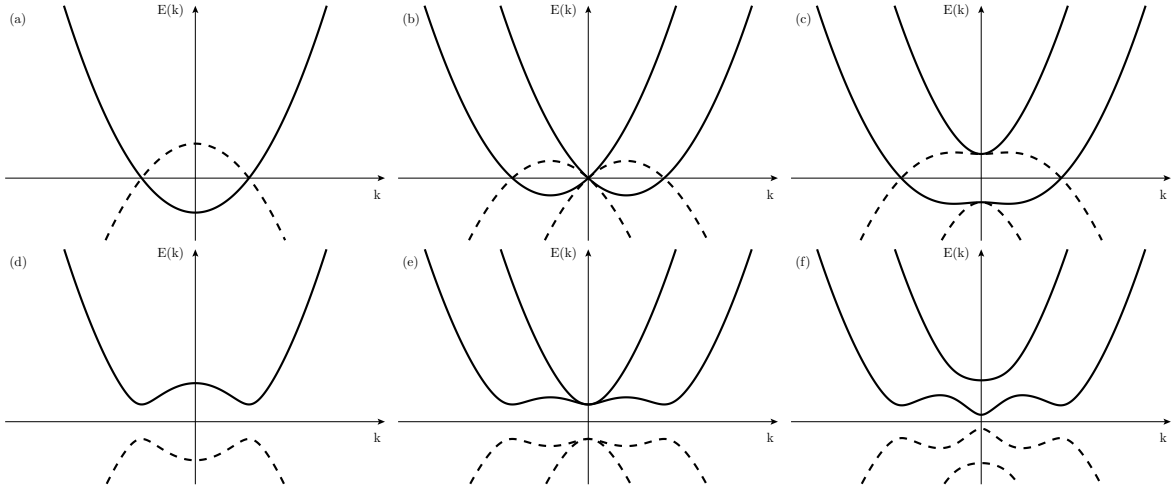

Fig. 6.5: Solid lines represent the energy dispersion relation for the electron in a quantum wire, while dashed lines represent the corresponding holes spectrum. The upper line of plots correspond to the case of no superconductivity, that is $\Delta = 0$, while the bottom line to the case of $\Delta = 0.25$. For the first columm (a and d) we use $\mu = 1/2$ and the rest of the interactions are set to zero. The second columm (b and e) $\mu = 0$, $\alpha = 1$ and $\Delta_x = 0$. Finally in the third columm $\alpha = 1$, $\Delta_x = 0.35$, and $\mu = 0$.

Loosely speaking, there will be two regions depending on the magnetic field energy Δ_x respect to the superconducting gap Δ. For $\Delta_x < \Delta$, the gap can not close for any value of μ or Δ. However, when $\Delta_x > \Delta$, at some point the gap closes for certain values of μ.

Tuning continuously any of the parameters involved in eq. (6.26), the gap can be closed and reopened. For the sake of simplicity we make $\mu = 0$, and therefore, the gap is closed for $\Delta = \Delta_x$. This is what happens in Fig. 6.6; the gap is closed and the dispersion relation becomes linear for the energy values close to zero. In this case, the magnetic field is tuned to be exactly equal to the gap, $\Delta_x = \Delta$,

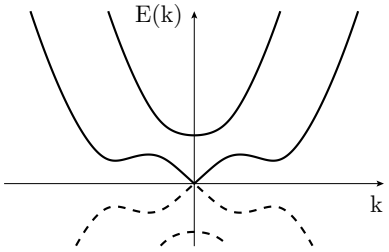

Fig. 6.6: Energy dispersion relation when the condition given by eq. 6.26 is fulfilled. The gap is closed with a linear dispersion relation. At this point it is produced the topological phase transition, that is, when the gap changes its sign. In this example we have used $\mu = 0$, and $\Delta = \Delta_x$.

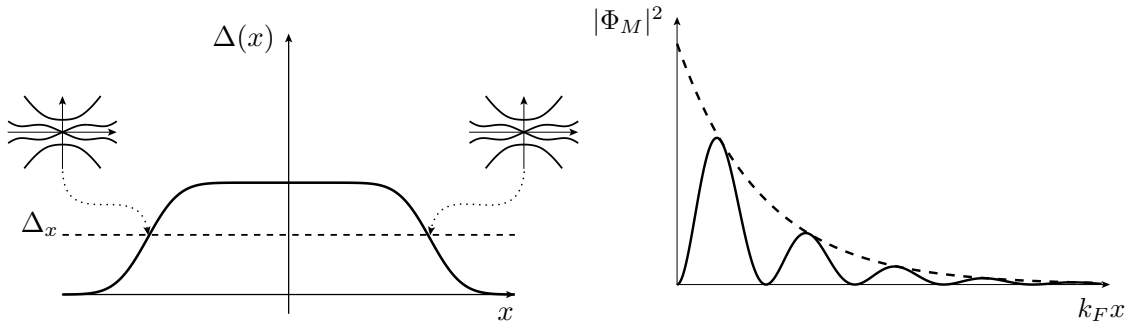

Fig. 6.7: In left pannel we represent the spatial variation of the pairing, with $\mu = 0$ and constant magnetic field. When the condition $\Delta = \Delta_x$ is fulfilled, the gap is closed and the mentioned topological phase transition is produced, due to the sign change of the gap. We can see here that the presence of the Majorana fermions are topologically protected, because any perturbation of the parameters do not destroy their presence. The right pannel shows the absolute value of the Majorana evanescent wave function given by eq. (6.35). Oscillations resemble the interference of two contributions, right and left movers.

leading to

$$\gamma_{1,k} = \frac{i}{\sqrt{2}}\left(c_{k,\downarrow} - c^\dagger_{-k,\downarrow}\right), \tag{6.27}$$

$$\gamma_{2,k} = \frac{1}{\sqrt{2}}\left(c_{k,\uparrow} + c^\dagger_{-k,\uparrow}\right), \tag{6.28}$$

$$\gamma_{3,k} = \frac{1}{2}\left(-c_{k,\uparrow} + c_{k,\downarrow} + c^\dagger_{-k,\downarrow} + c^\dagger_{-k,\uparrow}\right), \tag{6.29}$$

$$\gamma_{4,k} = \frac{1}{2}\left(c_{k,\uparrow} + c_{k,\downarrow} + c^\dagger_{-k,\downarrow} - c^\dagger_{-k,\uparrow}\right). \tag{6.30}$$

The first two modes are very interesting since at $k = 0$, they convert to Majorana modes, which means that they fulfill the property $\gamma_{0,i} = \gamma^\dagger_{0,i}$. One has to note that this relation is fulfilled because each component of the eigenstates contain the same spin. The latter two modes are not Majorana modes and correspond to the upper and lower bands, see Fig. 6.6.

6.4.3 Majorana bound states

In the previous section we have derived the condition that allows for the existence of Majorana fermions. In this way, the solutions given by eqs. (6.27-6.30) satisfy the Schrödinger equation, however, we need to take into account possible space variations of the involved parameters, i.e. $\mu(x), \Delta(x)$ and $\Delta_x(x)$. Therefore, the condition given in eq. (6.26) turns to $\mu(x) = \sqrt{\Delta_x(x)^2 + \Delta(x)^2}$ and the condition is then fulfilled at different points. A schema of the new situation can be seen in Fig. 6.7. For simplicity we assume $\mu = 0$, and a constant magnetic field, represented in Fig. 6.7 by a dashed line and a smooth variation of $\Delta(x)$. We observe that the equivalence is fulfilled at two points, where the curves cross each other, and thus two Majorana fermions are formed. This shows that the existence of a Majorana fermion is rather robust and does not depend on the shape of the potential, thus, revealing its topological nature.

In order to keep the Hamiltonian as simple as possible we make $\mu = 0$ and take into account that the relevant momenta are those placed close to $k = 0$. This allows to neglect second order terms,

yielding the Hamiltonian

$$H = \alpha p \sigma_z \tau_z + \Delta_x \sigma_x + \Delta(x)\tau_x. \tag{6.31}$$

Written in the basis $[\Psi_\uparrow, \Psi_\downarrow, \Psi_\downarrow^\dagger, -\Psi_\uparrow^\dagger]^T$ This approximation requires $\Delta_x \ll m\alpha^2$. We assume a linear behavior close to the point where the condition given by eq. (6.26) is satisfied, that is, $\Delta(x) = B + gx$. Because of particle-hole symmetry, it is usefull to square H. One has to take care due to the fact that now the spatial dependence of the pairing energy does not commute with the momentum. Therefore, terms such as $[\hat{p}, \Delta(x)]$ are different of zero. The resulting squared Hamiltonian has the form

$$H^2 = \alpha^2 p^2 + \Delta_x^2 + \Delta(x)^2 + 2\Delta(x)\Delta_x \tau_x \sigma_x - g\alpha \tau_y \sigma_z, \tag{6.32}$$

We diagonalize the Hamiltonian yielding

$$H^2 = \alpha^2 p^2 + (\Delta_x - \Delta(x))^2 \pm g\alpha, \tag{6.33}$$

the eigenvalues come from the quantum harmonic oscillator, that is

$$E^2 = 2\alpha g \left(n + \frac{1}{2}\right) \pm g\alpha \tag{6.34}$$

It has to be noted that for $n = 0$, and the appropiate sign $\pm$ the energy is equal to zero. This mode has an eigenfunction with a gaussian form

$$\varphi(x) = \left(\frac{|g|}{\alpha\pi}\right)^{1/4} e^{-|g|x^2/2\alpha}. \tag{6.35}$$

We can observe that the Majorana mode has a localization length proportional to the spin-orbit coupling α and inversely proportional to the variation of the pairing, given by g. Presenting a Majorana mode

$$\gamma = \gamma^\dagger = \int dx \varphi(x) \frac{1}{2} \begin{cases} -\Psi_\uparrow - i\Psi_\downarrow + i\Psi_\downarrow^\dagger - \Psi_\uparrow^\dagger \text{ for g¿0} \\ -\Psi_\uparrow + i\Psi_\downarrow - i\Psi_\downarrow^\dagger - \Psi_\uparrow^\dagger \text{ for g¡0} \end{cases} \tag{6.36}$$

The final solution is a superposition of left and right movers. Imposing the boundary condition $\Psi(x = 0) = 0$ the wave function becomes proportional to $2\sin(K_F x)$. In this way, the probability density $|\Psi(x)|^2$ presents oscillations as a function of the distance due to their interference [87], see Fig. 6.7. The number of oscillations will depend on the momentum and the localization length that imposes the spin-orbit interaction.

6.4.4 Majorana bound state in a Josephson junction

The next step consists on constructing a Josephson junction by placing together two superconducting slabs with a phase difference ϕ, where Majorana fermion modes are formed at the junction. The superconducting slabs present a gauge invariant phase difference ϕ. The junction is placed at $x = 0$, and for $x < 0$ we impose $\phi = 0$. In this situation, the solutions of the BdG equations for the independent

slabs are given by

$$\psi_L(x) = \sin(k_F x)\frac{\varphi(x)}{2}\begin{pmatrix}-1\\-i\\i\\-1\end{pmatrix} \quad \text{for x and g¡0} \tag{6.37}$$

(6.38)

$$\psi_R(x) = \sin(k_F x)\frac{\varphi(x)}{2}\begin{pmatrix}-e^{i\phi/2}\\ie^{i\phi/2}\\-ie^{-i\phi/2}\\-e^{-i\phi/2}\end{pmatrix} \quad \text{for x and g¡0.} \tag{6.39}$$

The tunnel between the slabs is given by

$$H_\tau = \tau\sum_\sigma\left[c^\dagger_{L,\sigma}(\bar{l})c_R(l) + h.c\right] \tag{6.40}$$

Using the solutions of the BdG equations we project the tunnel Hamiltonian onto the basis of the Majorana subspace [175], yielding

$$\mathcal{P}H_\tau = \sqrt{\frac{|g|}{\alpha\pi}}\sqrt{D}\cos(\phi/2)\left(\gamma^\dagger_L\gamma_R + \gamma^\dagger_R\gamma_L\right) \tag{6.41}$$

where $\sqrt{D} = \tau\sin^2(k_F l)/2\hbar v_F$ is the transition amplitude. Their eigenenergies are

$$E_\pm = \mp\sqrt{D}\cos(\phi/2), \tag{6.42}$$

which is 4π periodic and yields a 4π-periodic supercurrent

$$I_\pm = \pm\frac{e\sqrt{D}}{\hbar}\sin(\phi/2). \tag{6.43}$$

In the tunnel limit the transmission coefficient D is proportional to the square of the electron tunnel amplitude $D \propto \tau^2$. Remarkably, in contrast to normal Josephson junctions, where the current is proportional to τ^2, when the midgap states are involved in the transport the current becomes proportional to τ. This difference in the power of the tunnel is caused due to the fact that the transfer of electrons one by one in the presence of a Majorana bound state are allowed. However, in the absence of a Majorana bound state, there are no midgap states, so that the transfered electron is taken from below the gap and placed above the gap, at the energy cost of 2Δ. Thus, the trasnfer of a single electron is a virtual process. It must be followed by the trasnfer of another electron, so that the pair of electrons is absorbed into the condensate. This gives a current proportional to τ^2 It has to be noted that in both cases bulk supercurrent is carried by Cooper pairs. When a midgap state is present in the junction, a single transferred electron occupies a midgap state until another electron gets transferred. Then the pair of electrons becomes absorbed into the bulk condensate, the midgap state returns to the original configuration, and the cycle repeats.

Another interesting property of the Andreev energy in the presence of a Majorana bound state is the fact that the 4π-periodic current eq. (6.43) is proportional to D. In contrast, the normal Andreev energy is given by $E \propto \sqrt{1 - D\sin^2(\phi/2)}$. In figure 6.8 we represent both energy and current for two different values of D. We can observe that the 4π-periodic spectrum becomes detached from the 2π on when $D \ll 1$. It will be important to have in mind this property for the next chapter. There, we will

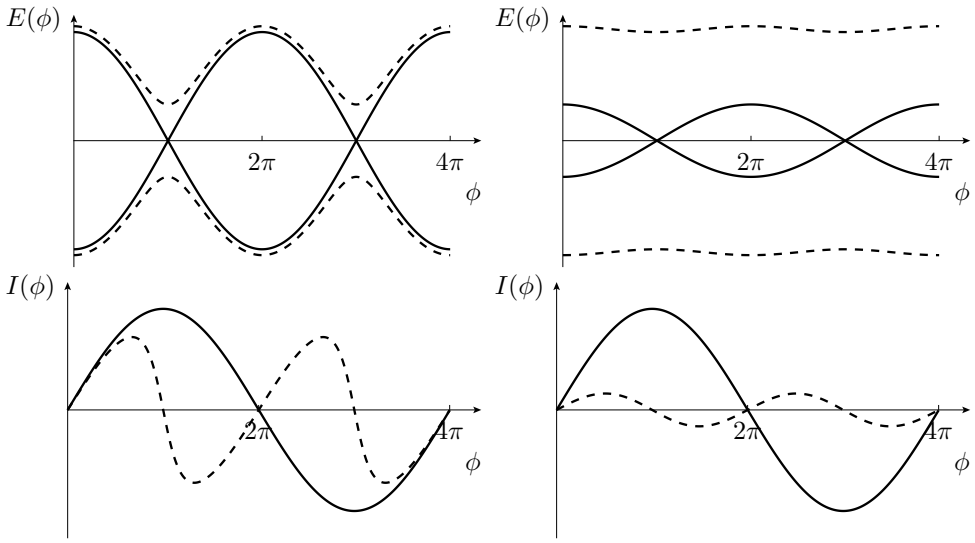

Fig. 6.8: Josephson energy (top) and current (bottom) as a function of ϕ for different values of the coefficient $D = 0.9$ (left pannels) and 0.1 (right pannels). We can observe how decreasing D, the 4π spectrum is detached from the 2π-periodic Andreev spectrum.

consider a phenomenological model where none dynamical effects between the 2π and 4π are considered. This can be only justified in the limit of $D \ll 1$, where the 4π-states are detached from the 2π-states, and no Landau-Zener transitions can be given [94, 52, 139]. This dependence will be also seen in the Josephson current since it is proportional to $\partial_\phi E(\phi)$, presenting a ratio of $I_M/I_N = 2/\sqrt{D}$.

Chapter 7

Current-biased Shapiro experiment in Majorana Josephson junctions

BEG TO INFORM YOU FRAM PROCEEDING ANTARCTIC
R. E. G. Amundsen

Summary

Our work analyzes theoretically for first time the fractional Josephson effect in a current driven configuration for a Josephson junction close to a quantum wire with SO interaction and in the presence of a magnetic field. We predict in which experimental conditions MF can be detected. On top of that recent experimental evidence by Rokhinson shows agreement with our predictions. In fact, these experiments show features which indicate the presence of MF, therefore it is of great interest to analyze the present configuration.

Our results predict a very robust behavior of the system in the presence of MF. It occurs in the strongly nonlinear dynamical regime (as in the experiment) where features indicating 4π current periodicity can unambiguously be present despite of the presence of a finite (and large) contribution of a 2π supercurrent; this is in fact the effect which is so puzzling and thus our prediction is very important for the explanation of the experimental finding; up to now it was believed that the fact of having 2π current contributions would hide the 4π periodicity in the experiment. That is what would occur in a voltage-biased Shapiro configuration but not in the present ac current biased experiment. This surprising result has not been previously explained in the literature.

Furthermore, we show that by tuning the frequency it is possible to select the junction periodicity. This result is not only important for the detection of MF but also for the analysis of non 2π periodic contributions to normal Josephson junctions.

7.1 Effective Hamiltonian of a finite Josephson junction featuring Majorana fermions

As we have seen in the last chapter, the energy of the junction can be described by the interaction between Majorana fermions at the junction. In order to describe such system, we can formulate the generic

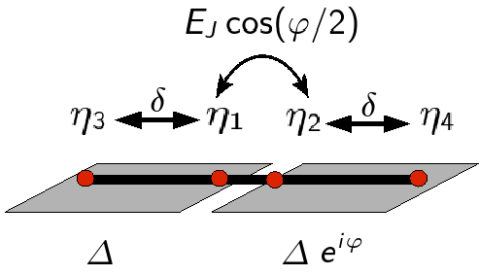

Fig. 7.1: Josephson junction with a nanowire on top. Red spots (color online) represent Majorana fermions. Double arrows represent the overlap between the Majorana fermions.

Hamiltonian

$$H_0 = iE_J \cos(\varphi/2)\, \eta_1 \eta_2, \tag{7.1}$$

where E_J is the Josephson energy of the junction, φ is the gauge invariant phase difference and the operators η_i are Hermitian $\eta_i = \eta_i^\dagger$ and they fulfill the anticommutator relation $\eta_i\eta_j + \eta_j\eta_i = 2\delta_{i,j}$. Due to the presence of MF the periodicity of the spectrum is 4π. This can be seen by the transformation $c_1 = \eta_1 + i\eta_2$, which leads to $E_\pm = \pm E_J \cos(\varphi/2)$.

7.2 Shapiro experiment

The Shapiro experiment has been proposed [85, 94, 104, 118] to detect the presence of Majorana fermions because it allows to deduce the periodicity of the current-phase relation of the junction, and therefore to distinguish between Majorana and normal modes, whose current is proportional to $\sin(\varphi/2)$, and $\sin(\varphi)$ respectively.

The physical fundament of the experiment consists of a resonance phenomena which involves the natural frequency of the Majorana (normal) Josephson junction $\omega_0 = (2)eV/\hbar$ and the frequency of an applied rf current (voltage) ω_{ac}. When the resonance is fulfilled, i.e. $V = n\hbar\omega_{ac}/(2)e$, the junction (forced system) adquires the frequency of the time dependet source. This phenomena is known as phase locked dynamics and is manifested as steps in the current/voltage. We can see an example of this in Fig. 7.2. Shapiro steps coming from a Majorana mode arise just at even multiples of the applied ac frequency, while normal modes appear at the whole spectrum of integer multiples.

In the present work we have studied the robustness of the current biased experiment versus the voltage-biased one. Before entering into the details, it seems convenient to present an introduction of both, the voltage and the current biased experiment.

7.2.1 Voltage biased Shapiro experiment

In the presence of Majorana and normal modes the Josephson current is given by

$$I(\varphi) = I_M \sin(\varphi/2) + I_c \sin(\varphi), \tag{7.2}$$

beeing $I_{N,M}$ the normal Andreev and Majorana current intensities. In principle, we assume that $I_M \ll I_c$. On the other hand, the phase difference is given by the Josephson formula

$$\frac{d}{dt}\varphi = \frac{2e}{\hbar}V(t). \tag{7.3}$$

This means that applying an external ac-voltage

$$V(t) = V_0 + V_1\cos(\omega_{ac}t), \tag{7.4}$$

we will be able to tune the phase difference, leading to

$$\varphi(t) = \varphi_0 + \omega_0 t + \frac{2eV_1}{\hbar}\sin(\omega_{ac}t). \tag{7.5}$$

Here we have used $\omega_0 \equiv 2eV_0/\hbar$. Then, we substitute eq. (7.5) into the Josephson current eq. (7.2)

$$I(t) = I_M\sum_n(-1)^n J_n\left(\frac{eV_1}{\hbar\omega_{ac}}\right)\sin\left(\frac{\varphi_0}{2} + \left(\frac{\omega_0}{2} - n\omega_{ac}\right)t\right) + I_c\sum_n(-1)^n J_n\left(\frac{2eV_1}{\hbar\omega_{ac}}\right)\sin\left(\varphi_0 + (\omega_0 - n\omega_{ac})t\right). \tag{7.6}$$

Thus, in the stationary limit just the contributions with $n\omega_{ac} = \omega_0$ survive, namely

$$\bar{I} = I_M\sum_n(-1)^n J_n\left(\frac{eV_1}{\hbar\omega_{ac}}\right)\delta\left((\omega_0/2 - n\omega_{ac})\right) + I_c\sum_n(-1)^n J_n\left(\frac{2eV_1}{\hbar\omega_{ac}}\right)\delta\left((\omega_0 - n\omega_{ac})\right). \tag{7.7}$$

with Dirac deltas placed at integer values of the radio frequency, $n\omega_{ac}$. It has to be noted that the contribution of the normal and Majorana modes are linear in $I_{c,M}$, and for this reason the height of the even steps will be sligthly modified by the presence of the Majorana mode in the case that $I_c \gg I_M$. Therefore, we can understand that the presence of the normal Andreev modes, which contributes with steps placed at all integer multiples, will difficult the separation of both contributions and thus the identification of the Majorana mode. For this reason, in the situation where $I_c \gg I_M$, the voltage biased experiment seems to be a non-sensitive method to detect the Majorana mode.

7.2.2 Current biased Shapiro experiment

When we apply an external current to the junction we have to use the Shapiro experiment by means of the resistive shunted junction model (RSJ) in the overdamped limit [158, 137]. The induced voltage on the junction can be calculated by solving the differential equation

$$I_0 + I_1\sin(\omega_{ac}t) = I(\varphi(t)) + \frac{\hbar}{2eR}\dot{\varphi}(t). \tag{7.8}$$

This equation is obtained from Kirchoff's law where an external DC I_0 and AC $I_1\sin(\omega_{ac}t)$ currents are applied to the junction. The outgoing current is modeled by a parallel circuit whose components are, $I(\varphi(t))$, given by Eq. (7.16), and a resistive current $(\hbar/2eR)\dot{\varphi}$ originated from from the current of quasiparticles. The solution of the differential equation (7.8), allows to obtain the induced voltage $V = \hbar\dot{\varphi}/2e$. In contrast to the voltage biased case, the current biased experiment is highly non-linear. As we will see below this last property turns out to be of main importance in the detection of the Majorana mode when it is accompained by several Andreev modes.

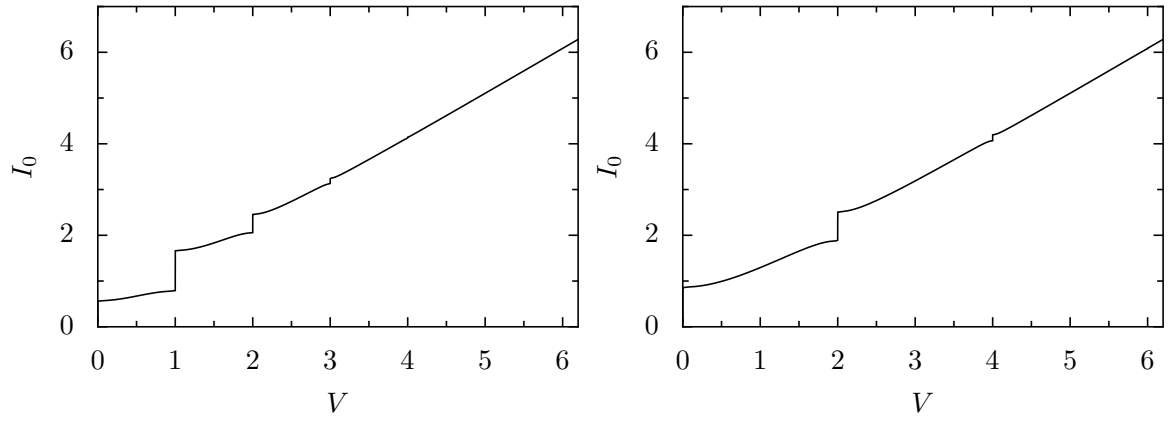

Fig. 7.2: I/V curve of a current biased Shapiro experiment in the presence of normal (left) and Majorana modes (right).

7.3 Additional effects

In practice, to distinguish the presence of a Majorana mode is expected to be more complicated due to the presence of additional effects that can turn the periodicity of the supercurrent from 4π to 2π and thus, the position of the steps. In this work we have taken into account three effects

- Finite size effects.
- Extra Andreev modes.
- Quasiparticle poisoning.

7.3.1 Finite size effects

In one-dimensional (1D) Majorana wire, Majorana fermions will appear at the end points [85]. In an ideal situation, the ends are infinitely apart from each other avoiding their recombination. In turn, when the wire is finite, the overlap, although very small, is different from zero, thus MF pair recombines and the special properties that the MF confer to the system are lost immediately [85, 124]. In order to include this phenomenon an extra term should be added, so that the total Hamiltonian becomes

$$H = iE_J \cos(\varphi/2)\eta_1\eta_2 + i\delta_R\eta_4\eta_2 + i\delta_L\eta_1\eta_3. \tag{7.9}$$

where we have introduced the parameters $\delta_{L,R}$ to account for overlap between the left and right in-phase MF which decreases exponentially with increasing distance between the Majorana modes (see Fig. 7.1). Considering that the in-phase MFs are far away compared with those on the junction we will use $\delta_i \ll E_J$. In this situation it is useful to switch to a representation where two Majorana fermions are combined to form one ordinary fermion. Thus, performing the substitutions $\eta_1 = i(l^\dagger - l)$, $\eta_2 = r^\dagger + r$, $\eta_3 = l^\dagger + l$, and $\eta_4 = i(r^\dagger - r)$, we obtain

$$H = 2\delta_R\left(r^\dagger r - \frac{1}{2}\right) + 2\delta_L\left(l^\dagger l - \frac{1}{2}\right) + \epsilon\left(-l^\dagger r^\dagger - l^\dagger r + lr^\dagger + lr\right), \tag{7.10}$$

where $l^\dagger l$ and $r^\dagger r = 0,\ 1$ counts the occupation of the corresponding state in the left and right sides respectively. We rewrite the former Hamiltonian in the occupation basis $|n_L, n_R\rangle$, that is $|0,0\rangle$, $|0,1\rangle$, $|1,0\rangle$ and $|1,1\rangle$, yielding the matrix

$$H = \begin{pmatrix} -\delta_L - \delta_R & 0 & 0 & -\epsilon \\ 0 & \delta_R - \delta_L & -\epsilon & 0 \\ 0 & -\epsilon & \delta_L - \delta_R & 0 \\ -\epsilon & 0 & 0 & \delta_L + \delta_R \end{pmatrix}. \tag{7.11}$$

We diagonalize the resulting Hamiltonian and obtain 4 eigenvalues

$$E^e_\pm = \pm\sqrt{\epsilon^2 + (\delta_L + \delta_R)^2} \text{ and} \tag{7.12}$$

$$E^o_\pm = \pm\sqrt{\epsilon^2 + (\delta_L - \delta_R)^2}. \tag{7.13}$$

where the super index denotes even (e) and odd (o) fermion parity respectively. Assuming that the parity is conserved we can choose one of the eigenvalues and make Landau-Zener transitions between the $\pm$ eigenvalues. In fact, we are only interested in the generic features which an avoided crossing has on the Shapiro steps. Thus we replace either $(\delta_L \pm \delta_R)^2$ by a characteristic/generic value 2δ which directly leads to Eq. (3). We have included a footnote in the manuscript making this explicit. Note furthermore that the signs of $\delta_{L/R}$ are random, i.e., determined by microscopic details. Thus, it is not true that the odd sector has a smaller gap than the even sector as one might naively expect when looking at the equations above. Yielding the 2π-periodic energy spectrum (see Fig. 7.3(a))

$$E^e_- = -\sqrt{\epsilon^2 + 4\delta^2} \tag{7.14}$$

It must be noted that making $\delta_L = \delta_R$ does not change qualitatively the results because δ just gives the energy scale of the splitting.

Non-adiabatic transitions: dynamical formation of Majorana fermions

As we have seen in the previous chapter, when the Majorana fermions are recombined the periodicity of the junction turns to a conventional one. Physically, one can circumvent this problem using a Josephson junction where the gauge invariant phase is tuned non-adiabatically [**?**]. In this way, transitions between the recombined fermions induce a dynamical decoupling into Majorana fermions. Since $E_J \gg \delta$, the transition probability is non-vanishing only at the anticrossings of the eigenspectrum, that is, for $\varphi = (2n+1)\pi$, where n is an integer (see red areas in Fig. 7.3(a)). Thus, as long as non-adiabatic transitions occur, the overlap between MF is effectively canceled. As a consequence, the 4π periodicity in the eigenspectrum, and also in the supercurrent ($I \propto \partial_\varphi E_\pm$), is recovered. As we will see below the new shape of the current does lead to the expected even steps and also to additional contributions of the order of δ at odd and fractional multiples of the ac frequency (see App. G).

In order to calculate the transition probability we consider the semiclassical approximation, and we make use of the fact that the velocity at the anticrossings is linear, therefore, transitions between states can be obtained by means of the Landau-Zener probability

$$P_{LZ} = \exp\left(-2\pi \frac{4\delta^2}{E_J \hbar \dot{\varphi}}\right). \tag{7.15}$$

It is important to remark that in the experiment we are analyzing, the phase φ is biased by a noisy voltage coming from fixing an external current. These voltage fluctuations are translated to phase fluctuations

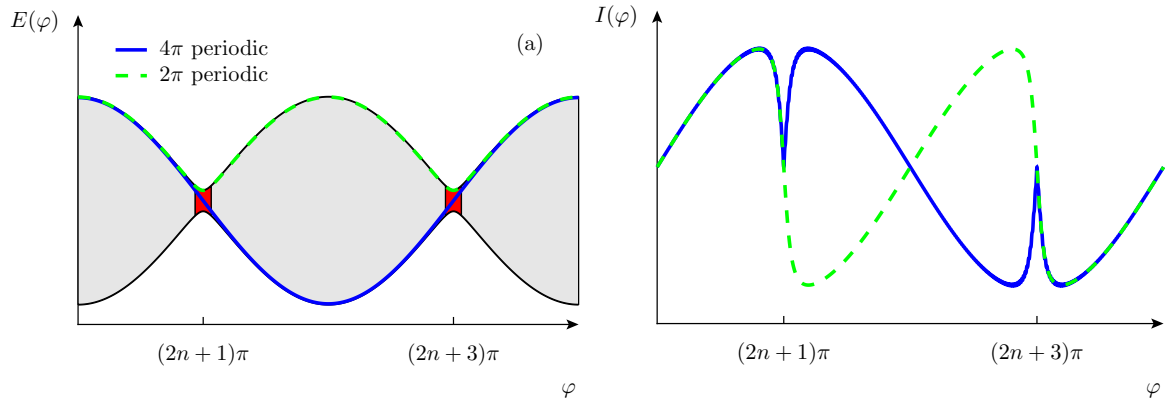

Fig. 7.3: (Color on line) Eigenspectrum (a) and Andreev current (b) vs φ, after zero (green dashed) and two (blue solid) LZT occurred. In panel (a) light and dark gray areas (gray and red) correspond to the adiabatic and non-adiabatic evolution respectively. We have represented two different limits of dynamics; the adiabatic limit (green dashed line), presenting 2π periodicity and the non-adiabatic limit (blue solid line) presenting 4π periodicity.

by the fact that $\dot{\varphi} \propto V$, and thus, dephasing enters into play. We have estimated that the dephasing time t_D is much shorter than the time needed to change the phase by $\varphi \to \varphi + 2\pi$. Therefore, we assume that interference effects can be neglected, and Landau-Zener transitions (LZT) can be considered individually. Coherences between LZTs have been recently analyzed phenomenologically [123], and in more detail [139] for the case of a voltage biased junction, where also additional Andreev levels, QP and inelastic transitions have been considered. However, we would like to stress that the current biased setup analyzed in this work for the first time has two advantages: contrary to the voltage biased case, it (1) shows a robust signal of small odd integer Shapiro steps even if the case of a multimode wire and (2) the observation is not masked by interference effects as those are absent in our case. Therefore, the current biased configuration is much more suitable to detect MF than the voltage biased one in the $D \ll 1$ case.

Model of the current

Once we have analyzed the dynamical transitions of the junction, we are ready to include their dynamical effects on the current. To this aim we introduce the function $I_M(\varphi)$ in the supercurrent

$$I(\varphi) = I_M(\varphi)\frac{2}{E_J}\frac{\partial}{\partial\varphi}E(\varphi). \tag{7.16}$$

The function, $I_M(\varphi)$, can take the constant values $\pm I_M$, where I_M is the maximum value of the supercurrent, which is of the order of nA. During the adiabatic period, the function $I_M(\varphi)$ remains constant and whenever there is a LZT, $I_M(\varphi)$ changes its sign. To understand the change of the sign we can compare in Fig. 7.3(b) the adiabatic and non-adiabatic passage through the anticrossings (solid and dashed respectively). After each anticrossing the curve coming from a LZT acquires a negative sign respect to the adiabatic passage. Thus, we describe the dynamical effects on the current produced by the LZT by changing the sign of I_M.

7.3.2 Extra Andreev modes

Up to this point we have considered the single band occupation case. Nevertheless, in order to represent a more realistic situation, it is necessary to include the occupation of several subbands.

Majorana fermions may occur in multimode nanowires as long as there is an odd-number of bands occupied [174, 127]. The extra modes contribute with the conventional 2π-periodic supercurrent, i.e. by means of adding $I_c \sin(\varphi)$ to $I(\varphi)$ in Eq. (7.16). The value I_c is a constant parameter whose contribution can be much greater than I_M, due to the possibility that several modes are occupied. Due to the linear properties of the voltage biased experiment the presence of extra modes add a dominant contribution to the odd steps, hiding the signature of the presence of the Majorana fermion. In contrast, in the current biased experiment we have found a regime where the effect of considering a dominant 2π contribution, does not modify the spectrum of even Shapiro steps.

It is worthy to mention that we have not considered dynamical effects between the Majorana and Andreev modes due to the fact that the energy difference between them is high enough compared to the phase velocity. This can be assured whenever the transparency of the junction fulfils $T \ll 1$ [52, 139].

7.3.3 Quasiparticle poisoning

As we have seen above, there are two pairs of eigenstates, each pair presents different fermion parity. The pair of eigenvalues $E^e_\pm$ correspond to the space where the states $|0,0\rangle$ and $|1,1\rangle$ are combined, while the pair $E^o_\pm$ correspond to the space where $|1,0\rangle$ and $|0,1\rangle$ are mixed. When the fermion parity is conserved these eigenvalues live in separate spaces. However, a change in the fermion parity produces a transition from one pair of eigenstates to the other [51], as relaxation or decoherence. Due to the fact that the superconductor is attached to normal contacts normal fermions can jump to the junction and thus change the fermion parity. In Josephson junctions the number of quasiparticle changes due to a phenomena known as quasiparticle poisoning. The rate estimated for this process is of the order of μs [154]. These transitions affect the current periodicity, and in principle they should appear reflected on the Shapiro steps positions. From previous experiments [154], it is known that the time scale of the quasiparticle poisoning is of the order of $t_{qp} \approx 1\mu$s. Therefore, the change on the periodicity produced by the quasiparticle poisoning can be considered negligible, since in the Shapiro experiment the dynamics of the system is ruled out by the ac frequency, which is of the order of $\omega_{ac} \approx 10^{10}$Hz.

7.4 Numerical results of the dynamical RSJ model in the presence of a Majorana mode

In this section we present numerical results of solving eq. 7.8 dynamically. By dynamically we mean that $I_M(\varphi)$ changes its sign depending on whether the LZT occurs or not. In order to include such a dynamical effect we compute P_{LZ}, on the anticrossings. Namely, when $\varphi(t) = (2n+1)\pi$ we evaluate the phase velocity $\dot{\varphi}$ and compare the resulting P_{LZ} with a random number to determine whether a LZT occurs or not.

7.4.1 Shapiro experiment with $I_c = 0$

In figure 7.4 we have plotted the I/V curves for $\omega_{ac} = 10^{10}\,\mathrm{Hz}$ and $I_1 = 0$ up to $I_1 = 4$nA with an increment of 1 nA. We can observe that the height of even Shapiro steps dominate the Shapiro spectrum. Thus, revealing clearly the resulting 4π periodicity of the junction. Moreover, there are some

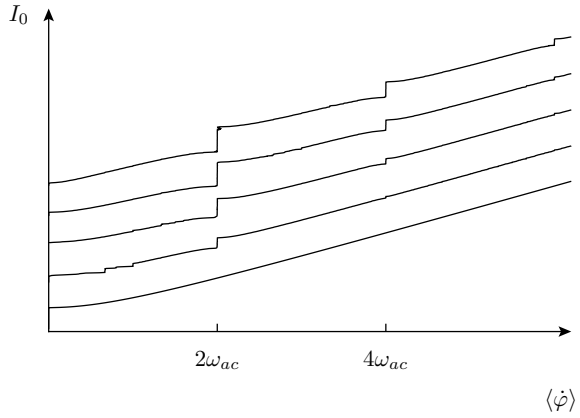

Fig. 7.4: Current-Voltage curves for $I_M = 1\,\mathrm{nA}$, $E_J/\delta = 500$, $R = 3\,\mathrm{k\Omega}$, $\omega_{ac} = 10^{10}\mathrm{Hz}$ and $I_c = 0$. I_1 takes values from 0 to 4 nA from bottom to top with a step of 1 nA. For the sake of clarity all the curves are shifted a constant amount.

contributions of δ order placed at odd and fractional multiples of ω_{ac}, coming from the new form of the supercurrent acquired by the LZT. It is worth to remind that in the ideal case, i.e. $I(\varphi) = I_M \sin(\varphi/2)$ such steps do not appear.

The main results of our calculations are shown in Figs. 7.4 and 7.6. There, we have represented current-voltage curves for $I_c = 0$ and $I_c = 10\,I_M$ respectively, using $I_M = 1\,\mathrm{nA}$ and R=3 kΩ, altogether lead to measure voltages of the order of $V \approx 10\,\mu\mathrm{V}$. We have set $E_J/\delta = 500$, making that P_{LZ} is very close to one at any value of I_0. Therefore, the supercurrent presents a 4π periodicity most of the time, whose form is given by the dashed curve of Fig. 7.3(b).

Until now the calculations we have shown were performed using the value $E_J/\delta = 500$, which leads to $P_{LZ} \simeq 1$ for the whole spectrum of I_0. Increasing the overlap δ reduces P_{LZ} making that non-LZT may occur, provoking a departure from the studied 4π periodicity of the current. The main changes are produced in the positions of the steps, where we observe that the Shapiro step splits in two (see Fig. 7.5). In order to shed some light on the numerical results we can average out the position of the non-LZT events and approximate $I_M(\varphi)$ by means of a Fourier series (see App. H). The resulting current-voltage curve behaves rather similar to the numerical results obtained by means of the stochastic model presented here. Comparing both methods we extract that the splitting is of the order of $(1 - P_{LZ})/2$. We observe that the Fourier approximation fails whenever we decrease E_J/δ up to 30.

7.4.2 Shapiro experiment in the presence of several Andreev modes: $I_c \gg I_M$

In figure 7.6 we show the I/V curves in the presence of a large 2π contribution, $I_c = 10\,I_M$. Different curves correspond to different values of ω_{ac}, in decreasing order from top to bottom. In this situation, one would expect to obtain all integer steps coming from the dominant 2π character of the supercurrent. In turn, one observes a progressive reduction of the odd steps as we decrease ω_{ac} up to $2eRI_M/\hbar$, while even steps hold. We have demonstrated that the reduction of odd steps is caused by the presence of a Majorana mode and can, in principle, be found even in the case where $I_c \gg I_M$. It is important to remark that this behavior is completely different to the voltage biased experiment, where the 2π contribution gives rise to steps at even and odd multiples, with heights proportional to I_c [78].

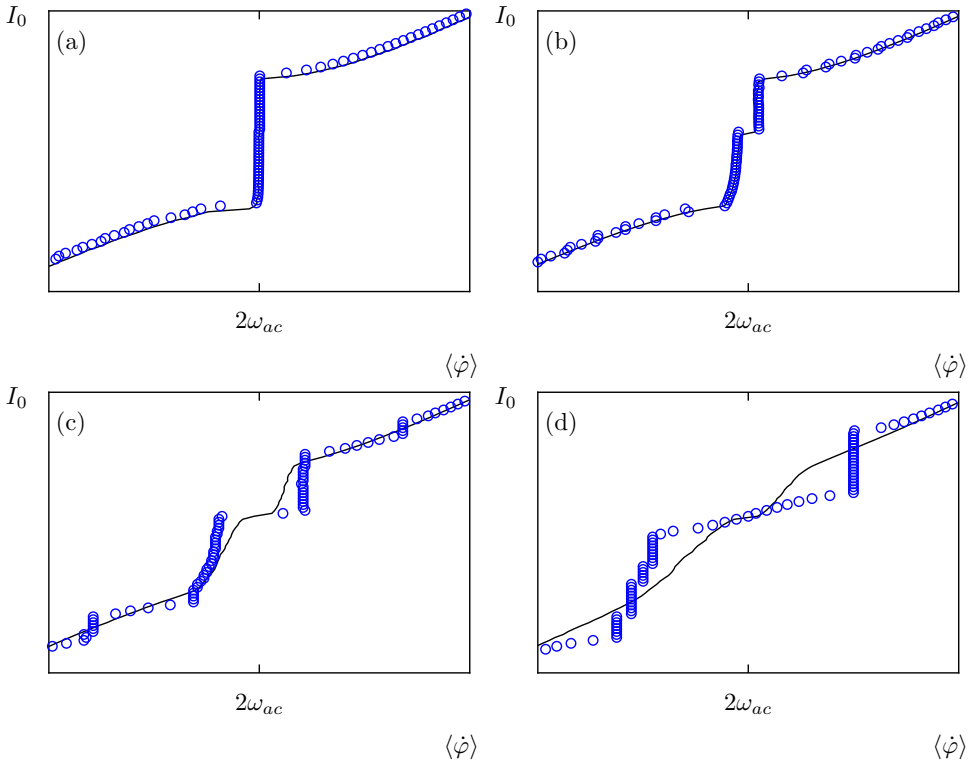

Fig. 7.5: Current/voltage curves for different values of E_J/δ: (a) 500, (b) 100, (c) 50 and (d) 30, $I_1 = 1\,\mathrm{nA}$, the rest of the parameters are taken from those used in Fig 3 in the main text. Solid lines are the values obtained by means of the stochastic model while blue circles come from the averaged model presented here.

Thus, when $I_c \gg I_M$ the detection of the Majorana mode from the Shapiro spectrum will in general complicated.

The observed behavior stands on the non-linear character of the RSJ model versus the linear one of the voltage biased experiment. In order to understand this it is necessary first to revisit the undriven case, i.e. $I_1 = 0$, where both, 2π and 4π contributions are present. In such situation, we show (see below) that due to the non-linear character of the RSJ equation, the presence of the 4π contribution imposes a strong 4π character to the junction for a range of voltages of the order of $I_M R$, even in the case when $I_c \gg I_M$. Ac currents with frequencies up to $2eRI_M/\hbar = 10^{10}\,\mathrm{Hz}$, correspond to this range of voltages and thus are expected to show predominately even Shapiro step.

We can extract additional information from the current-voltage curves. It can be demonstrated that the height of the 0-step at $I_1 = 0$, is approximately equal to $I_c + I_M/\sqrt{2}$ for $I_c \gg I_M$. Then, tuning the gate voltage one could, in principle, fill a single extra mode and measure the resulting contribution to the current. Then, one would be able to determine I_M.

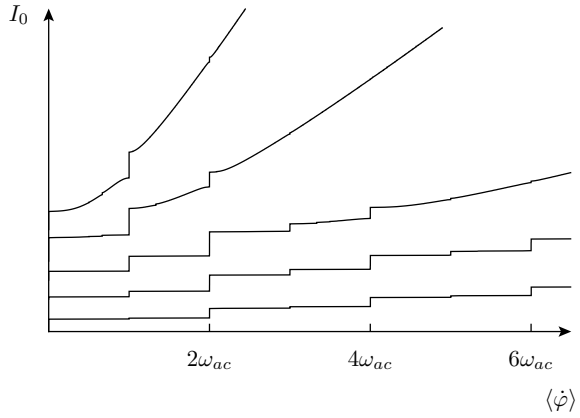

Fig. 7.6: Current-Voltage curves for $I_M = 1\,\mathrm{nA}$, $E_J/\delta = 500$, $R = 3\,\mathrm{k\Omega}$, $I_1 = 3\,\mathrm{nA}$ and $I_c = 10\,I_M$. The ac frequency ω_{ac} takes the values: 10^{11}, 5×10^{10}, 2×10^{10}, 10^{10} and $5\times10^{9}\,\mathrm{Hz}$ from top to bottom. We observe a progressive quenching of the odd steps as we decrease ω_{ac} up to $5\times10^{9}\,\mathrm{Hz}$. For the sake of clarity all the curves are shifted down a constant amount.

7.5 Analysis of the RSJ equation in the presence of extra Andreev modes: Robustness of the detection

In order to analyze the equation it results convenient to renormalize the involved parameters. Therefore, we divide the entire equation by I_c, and transform the time to a dimensionless quantity $\tau = (2eR/\hbar)t$. This results in the renormalization of the ac frequency $\xi = \hbar\omega_{ac}/2eRI_c$, leading to rewrite the equation as

$$\dot{\varphi}(\tau) = \alpha_0 + \alpha_1 \sin(\xi\tau) - \sin(\varphi) - \alpha_M \sin(\varphi/2) \tag{7.17}$$

where the renormalized intensities are given by $\alpha_i = I_i/I_c$ for $i = 1, M$. Now, the analysis of the equation is reduced to the study the parameter regime of α_1, α_M, and ξ.

The analytic solution of the equation in the absence of the Majorana mode is not known, and only approximate solutions have been obtained [4, 156, 93], although none of them are valid in the regime where we observe that odd steps vanish. Besides, the 4π term coming from the presence of the Majorana mode does the system even more complicated. For all these reasons, it is out of the scope of this appendix to try to give an analytical insigth of the differential equations. In turn, we explore the numerical solutions and explain its general behavior.

Undriven system without the Majorana term

The equation of motion of the system without neither MF nor ac current is given by

$$\dot{\varphi}(t) = \alpha_0 - \sin(\varphi(t)). \tag{7.18}$$

In Fig. 7.7 we show the dependence of $\langle\dot{\varphi}\rangle$ as a function of α_0. This case is analytically solvable, and the average of the voltage is given by

$$\bar{V} = \langle\dot{\varphi}\rangle = \sqrt{\alpha_0 - 1}. \tag{7.19}$$

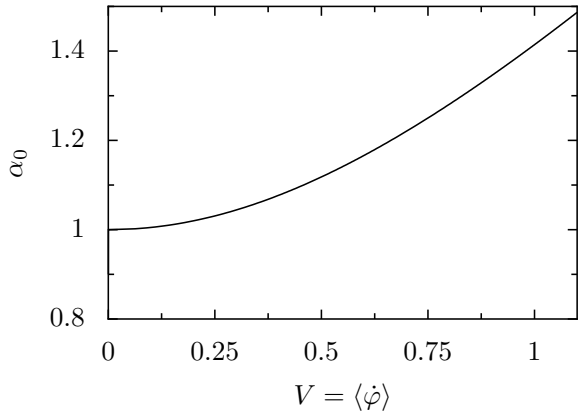

Fig. 7.7: α_0 vs $\langle\dot{\varphi}\rangle$ in the absence of the Majorana mode and without the ac current.

This equation is only valid for $\alpha_0 > 1$. The value $\alpha_0 = 1$ is called the critical value, which we denote by α_c, and is defined as the value up to which the induced voltage passes from zero to a finite value. In general, this value will change depending on whether we add the Majorana mode and/or the ac current. This value will be important in the incoming analysis.

In panel a of Figs. 7.8 and 7.9 we show numerical results of $\varphi(\tau)$ and $\dot{\varphi}(\tau)$ as a function of time for two different values of α_0. Figure 7.8 presents values of α_0 close to the critical value of each system, while Fig. 7.9 presents a higher value of α_0. As we can observe, $\varphi(\tau)$ presents two different ranges of slopes, i.e. velocities, fast and slow. The slow range is given when the term $\sin(\varphi) = 1$, so that the difference $\alpha_0 - \sin(\varphi)$ is minimum. This happens when $\varphi = (4n+1)\pi/2$ (dashed lines of panels a and b of Figs. 7.8 and 7.9). In figure 7.8 α_0 is very close to α_c, thus the difference $\alpha_0 - \sin(\varphi) \to 0$, and therefore we find a flat slope. For larger values of α_0 (see Fig. 7.9) the difference does not tend to zero and we observe an increment of the slope between stairs. In the bottom plot of Figs. 7.8 and 7.9 we show results of $\dot{\varphi}$ vs. time. There we can observe that the increment of α_0 induces a widening of the peaks. On the other hand, the fast range is given for the rest of the values of $\varphi(\tau)$, having a maximum speed when $\sin(\varphi(\tau)) = -1$ which occurs at $\varphi = (4n+3)\pi/2$. These ranges are periodically repeated with the frequency $\omega_0 = \bar{V}$ in units of $2e/\hbar$. That is, the frequency of the junction is proportional to the induced voltage. In summary, by increasing α_0 we modify the frequency of the junction ω_0, and we also provoke an increment of the slope between stairs, which produces a widening of the peaks seen in $\dot{\varphi}(\tau)$.

Undriven system with the Majorana mode

We add now the Majorana mode by including the term $\alpha_M \sin(\varphi/2)$ to the supercurrent yielding

$$\dot{\varphi}(\tau) = \alpha_0 - \sin(\varphi) - \alpha_M \sin(\varphi/2), \tag{7.20}$$

with $\alpha_M \ll 1$. In the example presented here we have used the value $\alpha_M = 1/15$, so that the sum of this term modifies slightly $\sin(\varphi)$. However, as we can observe in panel c of Fig. 7.9, the periodicity of $\varphi(\tau)$ is drastically modified for values of α_0 close to the new critical value, $\alpha_c \approx 1 + \alpha_M/\sqrt{2}$ (see panel c of Fig. 7.8). The solution $\varphi(\tau)$ turns from a 2π periodicity to a 4π for values of α_0 close to the critical value α_c (see Fig. 7.8c) and becomes 2π for larger values of α_0 (see Fig. 7.9c). This effect is non-linear and makes a difference respect to the voltage biased experiment.

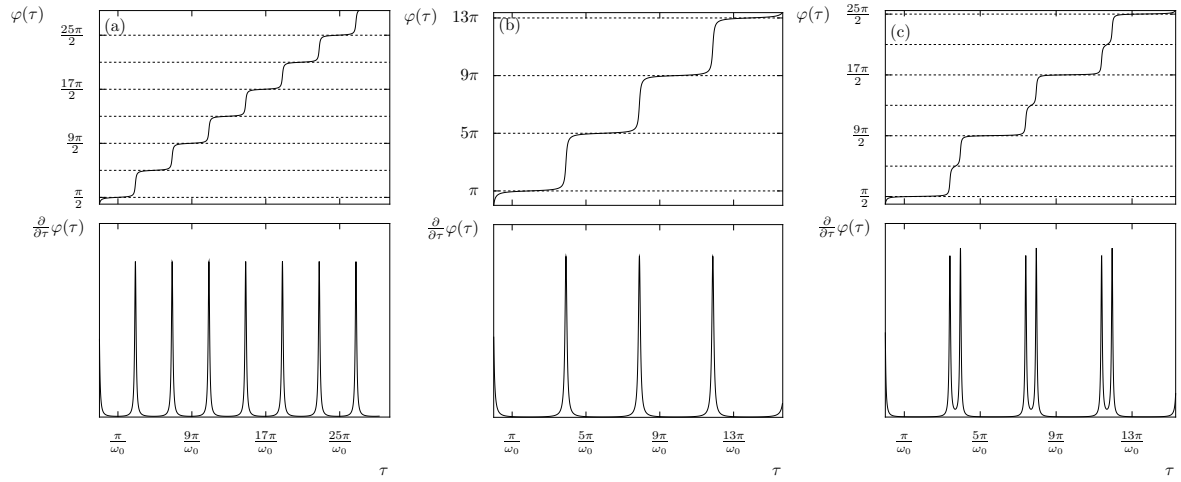

Fig. 7.8: $\varphi(\tau)$ (top row) and $\dot{\varphi}(\tau)$ (bottom row) as a function of time with a value of α_0 close to the critical value α_c in a 2π, 4π and mixed situation with $\alpha_M = 1/15$, from left to right.

The change in the periodicity can be explained by means of analogous arguments as above. The addition of the Majorana mode may increase or decrease the duration of the flat regions depending on the sign of $\sin(\varphi/2) > 0$. The time difference between the short and long periods increases as long as we are closer to the critical value α_c. Thus, the 2π periodic function turns to a 4π periodic one as $\alpha_0 \approx \alpha_c$, still with the characteristic frequency ω_0. A more visual comparison can be made just by looking the similarities with a pure 4π Josephson junction in panel b of Figs. 7.8 and 7.9.

We can study continously the transition from 4π to the 2π character of the junction calculating from numerics the largest frequency ω_M of the junction, defined by $\omega_M = 2\pi/\Delta\tau$, where $\Delta\tau$ is the dimensionless time difference between the two closest maximums of $\dot{\varphi}(\tau)$. When ω_M approaches ω_0, the junction turns to be 2π periodic. The general behavior is shown in Fig. 7.10, where we have plotted the relation ω_M/ω_0 vs. ω_0 for three different values of $\alpha_M = 1/15,\ 1/10$ and $1/5$. The curves show the tendency of the periodicity of the junction as we increase ω_0. We can observe that there is always a range of values of α_0, i.e. a range of ω_0, close to α_c where the Majorana mode imposes its 4π periodicity to the junction. Roughly speaking, this range is of the order of α_M. The dashed curve placed at $\omega_M/\omega_0 = 1$ points out the tendency of the junction to behave 2π periodically.

Driven system with the Majorana mode

Until now we have seen that the phase presents a range of voltages or frequencies where its dynamics is governed by the periodicity of the Majorana mode. The question now is that if we will be able to measure the periodicity of the phase in that range of frequencies. Typical procedure to measure the periodicity implies to drive the phase by means of an ac current, that is

$$\dot{\varphi}(\tau) = \alpha_0 + \alpha_1 \sin(\xi\tau) - \sin(\varphi(\tau)) - \alpha_M \sin(\varphi/2), \tag{7.21}$$

It is well known that the solutions $\varphi(\tau)$ at the steps are phase-locked solutions (e.g see Ref. [156]). This means that the driving force imposes its frequency to the driven system. In this way, the solutions of $\dot{\varphi}(\tau)$ change from the former frequency imposed by α_0, i.e. ω_0, to the ac frequency ξ.

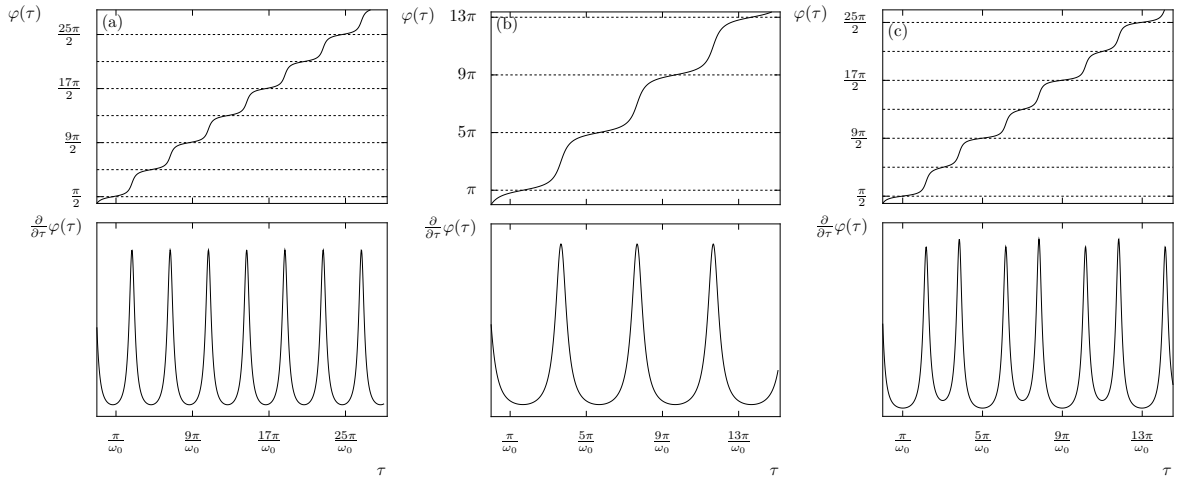

Fig. 7.9: Same plot as Fig. 7.8 for a larger value of α_0 respect to the critical value α_c. Comparing panel c of this figure and Fig. 7.8 we can appreciate the change of period when we move away from α_c, i.e. when $\alpha_0 \to \alpha_c$ (Fig. 7.9c→Fig. 7.8c) the periodicity of $\dot{\varphi}(\tau)$ approaches 4π.

This special property of the phase locked solutions is very important because it allows to access the range of frequencies where the junction behaves 4π periodically: Choosing $\alpha_M \gtrsim \xi$, that is, the order where we have seen that $\omega_M/\omega_0 \gg 1$, will lead to have a dominant 4π periodicity, which leads to an even Shapiro spectrum. We can see this behavior in the plots shown in Fig.7.11, where we have plotted the Shapiro steps for different values of α_M. We see how the odd steps tend to vanish for $\alpha_M \approx \xi$. Finally, we have plotted in Fig. 7.12 the height of the first four steps as a function of the ac intensity α_1 for $\alpha_M = 0.15$ and $\xi = 0.1$. We can observe a clear predominance of the even steps, for the whole range of α_1. Remarkably, we see that for $\alpha_1 \approx \alpha_M$, odd steps are zero. This behavior can be explained by the fact that in our reasoning we have implicitely considered that α_1, reads out the periodicity of the junction at the imposed frequencies ξ. In other words, we have considered that the effect of adding the ac current is to select the frequency of the junction, without introducing its 2π periodicity, and in such sense, it happens for α_1 of the order of α_M. We see that for larger values of α_1, odd steps coming from a 2π contribution become larger.

Summary

In this section we have explained numerically the behavior of the solutions $\varphi(\tau)$ and $\dot{\varphi}(\tau)$ of the current biased Shapiro experiment in the presence of a Majorana and several normal modes. We have given the explanation of the dominance (for a range of frequencies) of the even Shapiro steps in the presence of an, in principle, negligible 4π contribution respect to the 2π one. In order to understand this behavior we have explored the solutions of the undriven system and seen that in general there is always a region of frequencies where the 4π periodicity dominates. This region has an interval of frequencies of the order of $\omega_0 \lesssim \alpha_M$, where α_M is the dimensionless intensity of the Majorana mode. Therefore, if one wants to measure some signature of the 4π periodicity of the system, it will be needed that the measurement is performed in this frequency regime.

One of the advantages of the current biased Shapiro experiment consists on the fact that the

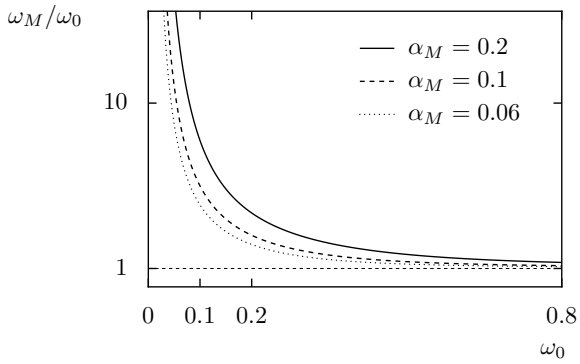

Fig. 7.10: Relation ω_M/ω_0 vs. ω_0 for $\alpha_M = 1/15,\ 1/10$ and $1/5$ (from left to right). It represents the 4π-contribution of the junction as a function of the 2π, given by ω_0. The range of values where $\omega_M/\omega_0 \gg 1$ indicates the 4π behavior of the junction. The dashed line corresponds to the value $\omega_M/\omega_0 = 1$, where is pure 2π periodic.

steps present phase locked solutions. This means that the forced system imposes its periodicity to the junction. Therefore, we can impose the ac frequency ξ to the junction ω_0 by means of biasing the junction by an ac current. And meanwhile measure the periodicity of the junction by looking at the positions of the steps. We have seen that when $\alpha_M \gtrsim \xi$ even Shapiro steps dominate, and also that this behavior is more robust when $\alpha_1 \approx \alpha_M$. Transforming back to physical units we have that taking into account that $I_M = 1\,\mathrm{nA}$ and $R = 3\,\mathrm{k\Omega}$, then $\omega_{ac} \lesssim 2eRI_M/\hbar = 10^{10}\,\mathrm{Hz}$.

7.6 Summary of results and limits of the model

We have studied the current-biased Shapiro experiment in a finite 1D Josephson junction. We have seen that the effects coming from the finiteness of the 1D system are dynamically decoupled driving the phase by means of an external current. For that purpose, we have analyzed the periodicity of the junction by solving an equation of motion coming from the resistive shunted junction model. We have calculated two different cases, when there are no extra 2π modes, i.e. $I_c = 0$, we have obtained that we can always determine the presence of the Majorana mode due to the appearance of steps at even multiples of the ac frequency ω_{ac} (see Fig. 7.4). In turn, when $I_c \gg I_M$, we have found that due to the non-linear effects coming from the dynamics of RSJ, the junction behaves 4π periodically for a range of voltages of the order $I_M R$. We have found that it is possible to match this range, and therefore its 4π behavior, by using ac frequencies of the order of $\omega_{ac} \lesssim 2eRI_M/\hbar = 10^{10}$Hz (see Fig. 7.6). The resulting Shapiro steps are thus placed at even multiples of the frequency ω_{ac}. In addition, we have seen that the effects of QP on the current are negligible at the typical estimated timescales. From our results, we believe that performing the current-biased Shapiro experiment is a strong tool to prove the existence of Majorana fermions in finite nanowires.

We now summarize the limitations of having represented the current by means of the presented model.

- $T \ll 1$: In order to avoid jumps between the Majorana mode and the normal Andreev modes we have assumed that the tunnel probability is $T \ll 1$, since the level spacing goes with $1/D$ (see previous chapter).

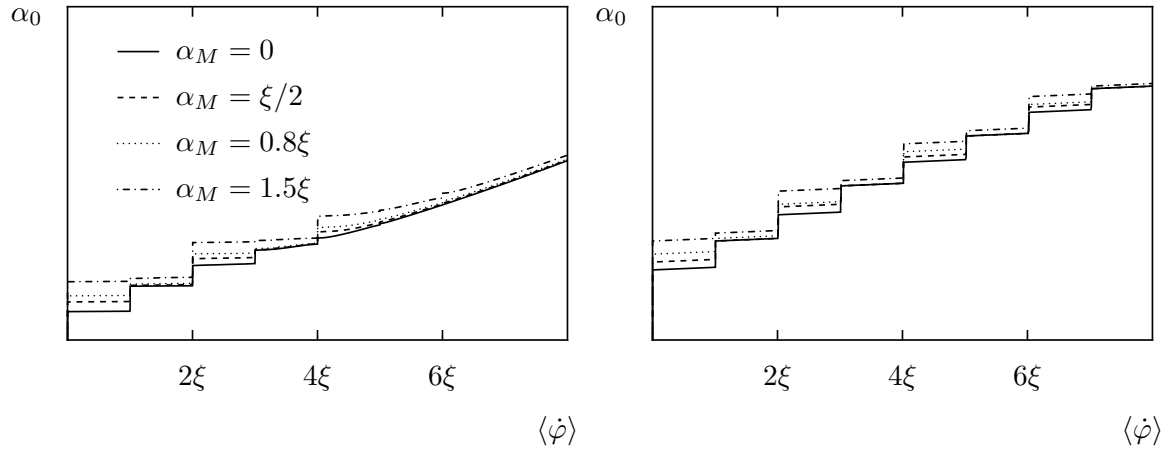

Fig. 7.11: Shapiro I-V curves for $\alpha_1 = 0.3$, and $\xi = 1/5$ for the left plot and $\xi = 1/20$ for the right plot. The value of α_M is increased from 0 to 1.5ξ in both plots. We can appreciate the reduction of the odd steps as long as $\alpha_M \gtrsim \xi$.

- RSJ: We have assumed that the capacitance of the junction is negligible, otherwise a second order derivative should be added. This is the topic of our present work.
- In the derivation of the robustness of the measurement of the Majorana mode we have assumed a perturbative α_1, so that just the frequency of the junction changes but not the periodicity of the undriven system does not change by the addition of the driving current. For higher α_1 the height of the steps behave as pseudo Bessel functions [137] with the peculiarity that the height of the odd steps present plateaus of zero height, as if it were a repetition of what happens at low α_1. This is also a matter of current investigation.

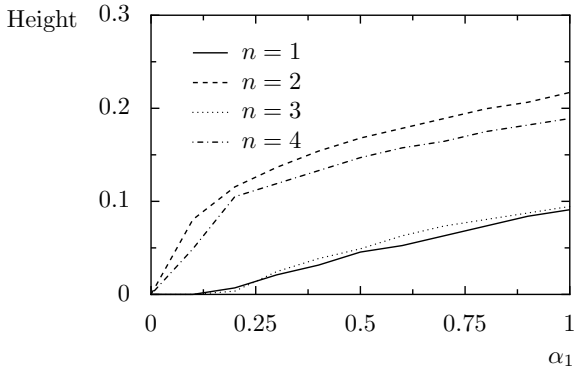

Fig. 7.12: Height of the first four steps as a function of α_1 for $\alpha_M = 0.15$ and $\xi = 0.1$.

Appendices

Apendix A

Rayleigh-Schrödinger perturbation theory

A.1 Rayleigh-Schrödinger perturbation theory

In most textbooks on quantum mechanics, perturbation theory is formulated for a perturbation linear in the small parameter, while the augmented Liouvillian $\mathcal{L}_\chi$ contains arbitrarily high powers of χ; see Eq. (2.15). In this appendix we derive a recursive scheme for the representation of an eigenvalue as a Taylor series in a perturbation parameter. Our calculation is inspired by Chap. 5 of Ref. [138], for an alternative derivation see Ref. [6]. Despite the fact that we formulate the problem in terms of a quantum mechanical energy eigenvalue problem, our derivation is not restricted to Hermitian operators.

We consider a "Hamiltonian" $H = H_0 + V(\alpha)$ for which the perturbation $V(\alpha)$ is an analytical function of the perturbation parameter α and vanishes in the limit $\alpha \to 0$. Thus, it can be decomposed into the series

$$V(\alpha) = \sum_{k=1}^{\infty} \alpha^k V_k. \tag{A.1}$$

Our goal is to find a series for the eigenvalue $E(\alpha)$ of H that fulfills $\lim_{\alpha\to 0} E(\alpha) = E_0$, where E_0 is the eigenvalue of H_0 corresponding to a particular eigenvector $|\phi_0\rangle$, i.e., $H_0|\phi_0\rangle = E_0|\phi_0\rangle$. A central assumption is that both the eigenvalue and the corresponding eigenvector $|\phi(\alpha)\rangle$ can be decomposed into a series in α as well, such that we can employ the ansatz

$$E(\alpha) = E_0 + \sum_{k=1}^{\infty} \alpha^k E_k \,, \tag{A.2}$$

$$|\phi(\alpha)\rangle = |\phi_0\rangle + \sum_{k=1}^{\infty} \alpha^k |\phi_k\rangle \,. \tag{A.3}$$

For the present purpose, it is sufficient to consider only the case of non-degenerate E_0. Note that for non-Hermitian H_0, $\langle\phi_0|$ is generally not the Hermitian adjoint of $|\phi_0\rangle$, but rather the corresponding left eigenvector, i.e., the solution of $\langle\phi_0|H_0 = E_0\langle\phi_0|$. We choose the normalization such that $\langle\phi_0|\phi_0\rangle = 1$.

We start by writing the eigenvalue equation $H|\phi(\alpha)\rangle = E(\alpha)|\phi(\alpha)\rangle$ in the form

$$(H_0 - E_0)|\phi(\alpha)\rangle = \{E(\alpha) - E_0 - V(\alpha)\}|\phi(\alpha)\rangle, \tag{A.4}$$

which is convenient for the derivation of a formal solution and subsequent iteration. Since $(H_0-E_0)|\phi_0\rangle = 0$, Eq. (A.4) defines $|\phi(\alpha)\rangle$ only up to a component proportional to $|\phi_0\rangle$. Moreover, it implies that the inverse of $H_0 - E_0$ does not exist. It is however possible to define the pseudo-inverse $Q(H_0 - E_0)^{-1}Q$ [or in short: $Q/(H_0 - E_0)$], where Q is the projector on the subspace spanned by the eigenvectors of H_0 with non-zero eigenvalue. In the present case of non-degenerate E_0, it reads $Q = \mathbf{1} - |\phi_0\rangle\langle\phi_0|$.

The pseudo-inverse allows one to cast Eq. (A.4) into the form

$$|\phi(\alpha)\rangle = |\phi_0\rangle + \frac{Q}{H_0 - E_0}\{E(\alpha) - E_0 - V(\alpha)\}|\phi(\alpha)\rangle. \tag{A.5}$$

The first term on the right-hand side can be multiplied by any factor without violating Eq. (A.4). We have chosen it such that $\lim_{\alpha\to 0}|\phi(\alpha)\rangle = |\phi_0\rangle$. Moreover, since $\langle\phi_0|Q = 0$, the relation $\langle\phi_0|\phi(\alpha)\rangle = \langle\phi_0|\phi_0\rangle = 1$ holds. An important feature of Eq. (A.5) is that the second term on the right-hand side is of first order in α. Therefore, it can be solved iteratively in the following way.

Multiplying Eq. (A.4) by $\langle\phi_0|$, we find that the left-hand-side vanishes owing to $\langle\phi_0|H_0 = E_0\langle\phi_0|$. Thus we obtain $E(\alpha)-E_0 = \langle\phi_0|V(\alpha)|\phi(\alpha)\rangle$. We then insert for $E(\alpha)$, $V(\alpha)$, and $|\phi(\alpha)\rangle$ the series (A.1)–(A.3) and compare coefficients to obtain the kth-order energy shift

$$E_k = \sum_{k'=1}^{k}\langle\phi_0|V_{k'}|\phi_{k-k'}\rangle. \tag{A.6}$$

It depends on the still unknown correction of the eigenvector, $|\phi_{k-k'}\rangle$, which we determine from Eq. (A.5). We again insert Eqs. (A.1)–(A.3) and compare coefficients to find

$$|\phi_k\rangle = \frac{Q}{H_0 - E_0}\Big\{\sum_{k'=1}^{k-1}E_{k'}|\phi_{k-k'}\rangle - \sum_{k'=1}^{k}V_{k'}|\phi_{k-k'}\rangle\Big\}. \tag{A.7}$$

Equations (A.6) and (A.7) allow the recursive computation of the series (A.2) for the eigenvalue shift $E(\alpha)$.

Apendix B

Average over the phonon operators in the Liouville space: Quantum regression theorem [23]

In this appendix we evaluate the formal expression of average over two general operators of the phonon mode at two different times, namely

$$\langle O_1(t)O_2(t')\rangle = \mathrm{Tr}_{\,\mathrm{R}\,\otimes\,\mathrm{S}}\left\{\xi(0)O_1(t)O_2(t')\right\}. \tag{B.1}$$

These averages appear in the Liouvillian $\mathcal{L}$corr, in our case R refers to the bath of oscillators and S to the phonon mode. The operators O_i act on the space S, and they satisfy the Heisenberg equation of motion

$$\frac{d}{dt}O_i = -\frac{i}{\hbar}\left[H, O_i\right] \tag{B.2}$$

Being H the total Hamiltonian of the phonon, bath and coupling among each other. It presents the formal solution

$$O_i(t) = e^{iHt/\hbar}O_i(0)e^{-iHt/\hbar} \tag{B.3}$$

giving also the formal solution for the density matrix

$$\xi(0) = e^{-iHt}\xi(t)e^{iHt} \tag{B.4}$$

substituting these formal solutions into eq. (B.1) and use the cyclic property of the trace to obtain

$$\begin{aligned}\langle O_1(t)O_2(t')\rangle &= \mathrm{Tr}_{\,\mathrm{R}\,\otimes\,\mathrm{S}}\left\{e^{-iHt}\xi(t)O_1(0)e^{iH(t'-t)}O_2(0)e^{-iH(t')}\right\}\\ &= \mathrm{Tr}_{\,\mathrm{R}\otimes\,\mathrm{S}}\left\{O_2(0)e^{-iH(t'-t)}\xi(t)O_1(0)e^{iH(t'-t)}\right\}\\ &= \mathrm{Tr}_{\,\mathrm{S}}\left\{O_2(0)\mathrm{Tr}_{\,\mathrm{R}}\left\{e^{-iH(t'-t)}\xi(t)O_1(0)e^{iH(t'-t)}\right\}\right\}.\end{aligned} \tag{B.5}$$

Let us make the assumption that $t' > t$ and define $\tau = t' - t$, and $\xi_O(\tau) = e^{-iH\tau}\xi(t)O_1(0)e^{iH\tau}$. Meaning that $\xi_O(\tau)$ also satisfies the Heisenberg equation of motion

$$\frac{d}{d\tau}\xi_O(\tau) = -\frac{i}{\hbar}\left[H, O_1\right] \tag{B.6}$$

with $\xi_O(0) = \xi(t)O_1(0)$ and we define $\rho_O(0) = \mathrm{Tr_R}\left\{\xi(t)O_1(0)\right\} = \rho(t)O_1(0)$. Since $\xi_O(\tau)$ fulfills equations of the Born-Markov approximation, we arrive to the expression

$$\frac{d}{d\tau}\xi_O = \mathcal{L}\xi_O \tag{B.7}$$

with formal solution

$$\xi_O(\tau) = e^{\mathcal{L}\tau}\left[\rho(t)O_1(0)\right] \tag{B.8}$$

then, we substitute this solution into eq. (B.5)

$$\langle O_1(t)O_2(t')\rangle = \mathrm{Tr_S}\left\{O_2(0)e^{\mathcal{L}\tau}\left[\rho(t)O_1(0)\right]\right\}. \tag{B.9}$$

so that the operator O_1 is finally written in the Heisenberg picture $O_{1,H}(\tau)$

$$\langle O_1(t)O_2(t')\rangle = \mathrm{Tr_S}\left\{O_{1,H}(\tau)O_2(0)\right\}. \tag{B.10}$$

Apendix C

Model of a lateral double quantum dot

In essence these references propose the Hamiltonian of two Coulomb interacting electrons embeded in a magnetic field having the Hamiltonian $H = H_{\rm orb} + H_Z = \sum_{i=1,2} h_i + C + H_Z$, where the single-particle Hamiltonian h_i describes the electron dynamics confined to the xy-plane[1] and

$$h_i = \frac{1}{2m}\left(\mathbf{p}_i - \frac{e}{c}\mathbf{A}(\mathbf{r}_i)\right)^2 + ex_iE + V(\mathbf{r}_i), \tag{C.1}$$

$$C = \frac{e^2}{\kappa|\mathbf{r}_1 - \mathbf{r}_2|}, \tag{C.2}$$

$$H_z = g\mu_B \sum_i \mathbf{B}_i \cdot \mathbf{S_i} \tag{C.3}$$

The coupling of the dots is modeled by a quatic potential [18]

$$V(x,y) = \frac{m\omega_0^2}{2}\left[\frac{1}{4a^2}(x^2-a^2)^2 + y^2\right], \tag{C.4}$$

which separates one dot from each other a distance $2a$, into two harmonic wells of frequency ω_0, and therefore the Bohr radius of each dot is given by $a_B = \sqrt{\hbar/m\omega_0}$. The choice of the potential is motivated by the experimental fact that for single dots the dots can be described by a parabolic confinement potential of $\hbar\omega_0 = 3$meV.

The single-dot orbitals for harmonic confinement in two dimensions in a perpendicular magnetic field are the Fock-Darwin states, which are the usual harmonic oscillator states, magnetically compressed by a factor $b = \omega/\omega_0 = \sqrt{1 + \omega_{\rm L}^2/\omega_0^2}$, where $\omega_{\rm L} = eB/2mc$ denotes the Larmor frequency. The ground state (energy $\hbar\omega = b\hbar\omega_0$) centered at the origin is

$$\varphi(x,y) = \sqrt{\frac{m\omega}{\pi\hbar}}e^{-m\omega\left(x^2+y^2\right)/2\hbar}. \tag{C.5}$$

Shifting the single particle orbitals to $(\pm a, 0)$ in the presence of a magnetic field we obtain $\varphi_{\pm a}(x,y) = \exp(\pm iya/2l_B^2)\varphi(x \mp a, y)$. The phase factor involving the magnetic length $l_B = \sqrt{\hbar c/eB}$ is due to the gauge transformation $\mathbf{A}_{\pm a} = B(-y, x \mp a, 0)/2 \rightarrow \mathbf{A} = B(-y, x, 0)/2$. The matrix elements of

[1] The electrons have the effective mass $m = 0.067m_e$, $g = -0.44$, μ_B is the Bohr magneton and $\kappa = 13.1$.

$H_{\rm orb}$ needed to calculate J are found by adding and subtracting the harmonic potential centered at $x = -(+)\,a$ for electron 1(2) in $H_{\rm orb}$, which then takes the form $H_{\rm orb} = h^0_{-a}(\mathbf{r}_1) + h^0_{+a}(\mathbf{r}_2) + W + C$, where $h^0_{\pm a}(\mathbf{r}_i) = (\mathbf{p}_i - e\mathbf{A}(\mathbf{r}_i)/c)^2/2m + m\omega^2((x_i \mp a)^2 + y_i^2)/2$ is the Fock-Darwin Hamiltonian shifted to $(\pm a, 0)$, and $W(x,y) = V(x,y) - m\omega^2((x_1+a)^2 + (x_2-a)^2)/2$. We obtain

$$J = \frac{2S^2}{1-S^4}\left(\langle 12|C+W|12\rangle - \frac{\mathrm{Re}\langle 12|C+W|21\rangle}{S^2}\right), \tag{C.6}$$

where the overlap becomes $S = \exp(-m\omega a^2/\hbar - a^2\hbar/4l_B^4 m\omega)$. Evaluation of the matrix elements of C and W yields

$$J = \frac{\hbar\omega_0}{\sinh\left(2d^2(2b-1/b)\right)}\left[c\sqrt{b}\left(e^{-bd^2}\mathrm{I}_0(bd^2) - e^{d^2(b-1/b)}\mathrm{I}_0(d^2(b-1/b))\right) + \frac{3}{4b}\left(1+bd^2\right)\right], \tag{C.7}$$

where we introduce the dimensionless distance $d = a/a_{\rm B}$, and I_0 is the zeroth order Bessel function. The first and second terms in Eq. (C.7) are due to the Coulomb interaction C, where the exchange term enters with a minus sign. The parameter $c = \sqrt{\pi/2}(e^2/\kappa a_{\rm B})/\hbar\omega_0$ (≈ 2.4, for $\hbar\omega_0 = 3\,\mathrm{meV}$) is the ratio between Coulomb and confining energy. The last term comes from the confinement potential W.

Apendix D

Polaron transformation and the interacting picture in the triple quantum dot

D.1 Polaron transformation

As it was sketched in the main text, we transform the operators by means of

$$\overline{O} = e^{S} O e^{-S}, \quad \text{where} \quad S = \frac{\lambda}{\hbar\omega_0} n_2 (a^\dagger - a). \tag{D.1}$$

Then, using the Baker-Hausdorff formula

$$\overline{O} = O + [S, O] + \frac{1}{2!}[S, [S, O]] + \frac{1}{3!}[S, [S, [S, O]]] + \cdots, \tag{D.2}$$

one can obtain the exact transformation of the total Hamiltonian. Lets do it for each operator appearing in the master equation.

Triple quantum dot

Lets start from the dot Hamiltonian, since

$$[S, n_2] = 0 \Rightarrow \Big[S, \big[S, \ldots [S, n2]\big] \ldots\Big] = 0 \tag{D.3}$$

it means that $\overline{n}_2 = n_2$. Then, proceding in the same way for the tunnel dots p_{ij}

$$[S, p_{12}] = -\frac{\lambda}{\hbar\omega_0}(a^\dagger - a) p_{12} \tag{D.4}$$

$$\big[S, [S, p_{12}]\big] = \left(-\frac{\lambda}{\hbar\omega_0}(a^\dagger - a)\right)^2 p_{12} \tag{D.5}$$

$$\Rightarrow \Big[S, \big[S, \ldots [S, p_{12}]\big] \ldots\Big] = \left(-\frac{\lambda}{\hbar\omega_0}(a^\dagger - a)\right)^n p_{12} \tag{D.6}$$

then it is straightforward to deduce that

$$\overline{p}_{13} = p_{13} \tag{D.7}$$

$$\overline{p}_{12} = e^{-\frac{\lambda}{\hbar\omega_0}(a^\dagger - a)} p_{12} \tag{D.8}$$

$$\overline{p}_{23} = e^{\frac{\lambda}{\hbar\omega_0}(a^\dagger - a)} p_{23} \tag{D.9}$$

Phonon Hamiltonian

On the other hand, the transformation on the phonon operators leads to

$$[S, a^\dagger] = -\frac{\lambda}{\hbar\omega_0} n_2 \tag{D.10}$$

$$\left[S, [S, a^\dagger]\right] = 0 \tag{D.11}$$

which leads to a displacement of the phonon operator,

$$\overline{H}_{ph} = \hbar\omega_0 \left(a^\dagger a - \frac{\lambda}{\hbar\omega_0} n_2 (a^\dagger + a) + \left(\frac{\lambda}{\hbar\omega_0}\right)^2 n_2 \right). \tag{D.12}$$

D.1.1 Interaction Picture

Once we have done the polaron transformation we take the interaction picture respect to the Hamiltonian

$$\epsilon n_2 + \tau \left(p_{13} + p_{13}^\dagger \right) \tag{D.13}$$

The interaction picture of a generic operator is given by the unitary transformation

$$\tilde{O}(t) = exp\left[\frac{iH_0 t}{\hbar}\right] \overline{O} exp\left[-\frac{iH_0 t}{\hbar}\right]. \tag{D.14}$$

Using the Baker-Hausdorff formula:

$$\tilde{O}(t) = \overline{O} + \kappa[H_0, \overline{O}] + \frac{\kappa^2}{2!}[H_0, [H_0, \overline{O}]] + \frac{\kappa^3}{3!}[H_0, [H_0, [H_0, \overline{O}]]] + \cdots \tag{D.15}$$

where H_0 is given by the Hamiltonian (D.13), and $\kappa = it/\hbar$

Dot operators

The best way to obtain the interaction picture of

$$\begin{aligned} \tilde{H}_T(t) &= e^{iH_0 t/\hbar} \bar{H}_T e^{-iH_0 t/\hbar} = e^{iH_0 t/\hbar} \sum_{i,j} |\Psi_i\rangle\langle\Psi_i|\bar{H}_T|\Psi_j\rangle\langle\Psi_j| e^{-iH_0 t/\hbar} \\ &= \sum_{i,j} e^{i(\epsilon_i - \epsilon_j)t/\hbar} |\Psi_i\rangle\langle\Psi_j| \langle\Psi_i|\bar{H}_T|\Psi_j\rangle \end{aligned} \tag{D.16}$$

where we have used $|\Psi_i\rangle$ and ϵ_i as the eigenfunctions and the eigenenergy of $\bar{H}_0$, given by

$$|\Psi_1\rangle = (0,1,0)^T \rightarrow \epsilon_1 = \epsilon \tag{D.17}$$

$$|\Psi_2\rangle = 2^{-1/2}(-1,0,1)^T \rightarrow \epsilon_2 = -\tau \tag{D.18}$$

$$|\Psi_3\rangle = 2^{-1/2}(1,0,1)^T \rightarrow \epsilon_3 = \tau \tag{D.19}$$

Damped phonon mode

Since we are dealing with a damped harmonic oscillator which master equation is given by

$$\frac{d}{dt}\rho_B = -i\hbar\omega_0\left[a^\dagger a, \rho_B\right] - \frac{\gamma_b}{2}\left(2a\rho_B a^\dagger - a^\dagger a\rho_B - \rho_B a^\dagger a\right). \tag{D.20}$$

the interaction picture will be a bit different, instead of that picture we will write the time evolution operators in the Heisenberg picture, namely

$$a_H(t) = ae^{-(i\hbar\omega_0+\gamma/2)t} \tag{D.21}$$

$$a_H^\dagger(t) = a^\dagger e^{(i\hbar\omega_0-\gamma/2)t} \tag{D.22}$$

leading to the final Hamiltonian

$$\tilde{H}_T(t) = \tau\left(p_{12}e^{-i(\epsilon+\tau)}X_t^\dagger + p_{23}e^{i(\epsilon-\tau)}X_t + h.c.\right) \tag{D.23}$$

where we have used the Heisenberg picture of the displacement operators

$$X_t = \exp\left(\frac{\lambda}{\hbar\omega_0}\left(-ae^{-(i\hbar\omega_0+\gamma/2)t} + a^\dagger e^{(i\hbar\omega_0-\gamma/2)t}\right)\right) \tag{D.24}$$

Apendix E

Explicit calculation of the phonon renormalized tunnels and the correlation functions

In this appendix we evaluate the average over one and two operators at different times which appear in the obtained Liouvillian eq. (**??**).

E.1 Renormalized tunnel

The first term we treat is the term which gives rise to the coherent renormalization of the tunnel, namely

$$\frac{\tau_{\rm renorm}}{\tau} = \langle X_t \rangle = \langle X_t^\dagger \rangle = \mathrm{Tr}_{\,\mathrm{R}\,\otimes\,\mathrm{S}}\{X_t \rho(0)\} = \mathrm{Tr}_{\,\mathrm{S}}\{X \mathrm{Tr}_{\,\mathrm{R}}\ \{\rho(t)\}\} = \mathrm{Tr}_{\,\mathrm{S}}\{X \rho_S(t)\} \tag{E.1}$$

Considering that S behaves Markovianly we obtain,

$$\frac{\tau_{\rm renorm}}{\tau} = \sum_n^\infty \langle n|X\rho_S|n\rangle = e^{\left(\frac{\lambda}{\hbar\omega_0}\right)^2\left(\frac{1}{2}-Z\right)} \tag{E.2}$$

E.1.1 Correlation functions

The correlation functions

$$C(t) = \langle X^\dagger(0)X(t)\rangle_{\rm eq} = \mathrm{tr}\{X^\dagger(0)X(t)\rho_{\rm ph,eq}\}, \tag{E.3}$$

of the dissipative harmonic oscillator, where $X = \exp\{(\lambda/\omega_0)(a^\dagger - a)\}$ is the displacement operator used for the polaron transformation in Sec. 4.4. The time evolution is determined by the master equation

$$\begin{aligned}\frac{d}{dt}\rho =& -i\omega_0[a^\dagger a, \rho] \\ &+ \frac{\gamma}{2}(\bar{n}+1)(2a\rho a^\dagger - a^\dagger a\rho - \rho a^\dagger a) \\ &+ \frac{\gamma}{2}\bar{n}(2a^\dagger\rho a - aa^\dagger\rho - \rho aa^\dagger),\end{aligned} \tag{E.4}$$

whose stationary state is the equilibrium density matrix

$$\rho_{\rm ph,eq} = \frac{1}{Z}\exp(-\hbar\omega_0 a^\dagger a/k_B T), \tag{E.5}$$

where we have used $Z = [1-\exp(-\hbar\omega_0/k_B T)]^{-1}$.

The time evolution is conveniently computed from the Heisenberg equation of motion for the annihilation operator, $\dot{a}_H = -(i\omega_0 + \gamma/2)a_H$, with the solution

$$a_H = a e^{-(i\omega_0+\gamma/2)t}, \tag{E.6}$$

such that

$$X_H(t) = \exp\left[\frac{\lambda}{\omega_0}\left(a^\dagger e^{(i\omega_0-\gamma/2)t} - \text{h.c.}\right)\right] \tag{E.7}$$

Zero temperature

At zero temperature the initial density matrix state of the damped single mode is given by $\rho_b(0) = |0\rangle\langle 0|$, we calculate the correlation function

$$\begin{aligned}
C(t) =& \text{Tr}_{\rm ph}\left\{\rho_b(0)X_H(t)X^\dagger(t=0)\right\} = \langle 0|X_H(t)X^\dagger(t=0)|0\rangle = \\
=& \exp\left[-\frac{1}{2}\left|\frac{\lambda}{\hbar\omega_0}\right|^2 e^{-\gamma t}\right]\exp\left[-\frac{1}{2}\left|\frac{\lambda}{\hbar\omega_0}\right|^2\right]\langle 0|e^{-\frac{\lambda}{\hbar\omega_0}a\exp(-i\hbar\omega_0-\gamma/2)t)}e^{-\frac{\lambda}{\hbar\omega_0}a^\dagger}|0\rangle \\
=& \exp\left[-\frac{1}{2}\left|\frac{\lambda}{\hbar\omega_0}\right|^2\left(e^{-\gamma t}+1\right)\right]\sum_{n=0}^{\infty}\left|\frac{\lambda}{\hbar\omega_0}\right|^{2n}\frac{e^{-n(i\hbar\omega_0+\gamma/2)t}}{n!} \\
=& \exp\left[-\frac{1}{2}\left|\frac{\lambda}{\hbar\omega_0}\right|^2\left(e^{-\gamma t}+1\right)\right]\exp\left[\left|\frac{\lambda}{\omega_0}\right|^2 e^{-(i\hbar\omega_0+\gamma/2)t}\right] \\
=& \exp\left[-\left|\frac{\lambda}{\hbar\omega_0}\right|^2\left(\frac{1}{2}+\frac{e^{-\gamma t}}{2}-e^{-(i\hbar\omega_0+\gamma)t}\right)\right]
\end{aligned} \tag{E.8}$$

Finite temperature

In this case the algebra is not so simple as in the above case and extra calculations must be done. First of all the initial density matrix is not the vacuum state, but a thermal bath, i.e.

$$\rho_b = Z^{-1}\exp(-\hbar\omega_0\beta a^\dagger a) \tag{E.9}$$

where $\beta = K_B T$ and $Z = (1-\exp(-\omega_0\beta))$. Introducing this density state in the correlation function, we obtain,

$$C(t) = Z^{-1}\sum_{n=0}^{\infty} e^{-n\hbar\omega_0\beta}\langle n|X_H(t)X^\dagger(t=0)|n\rangle \tag{E.10}$$

making use once again of the Haussdorf-Baker formula we join the exponents of each operator in a common one, i.e. $\exp(A)\exp(B) = \exp(A+B)\exp\left(\left[A,B\right]/2\right)$, being this time $A = X_H(t)$ and $B = X^\dagger(t=0)$, then we call the commutator as

$$K_1 = \left[A,B\right] = \left(\frac{\lambda}{\hbar\omega_0}\right)^2\left[a^\dagger e^{(i\hbar\omega_0-\gamma/2)t} - a e^{-(i\hbar\omega_0+\gamma/2)t}, a-a^\dagger\right] = \left(\frac{\lambda}{\hbar\omega_0}\right)^2\left(-2i\sin(\hbar\omega_0 t)\right)e^{-\gamma/2t}. \tag{E.11}$$

Then,

$$X_H(t)X^\dagger(t=0) = e^{K_1/2}\exp(\delta a^\dagger - \delta^* a) \tag{E.12}$$

$$= e^{K_1/2}e^{-K_2/2}\exp(-\delta^* a)\exp(\delta a^\dagger) = \tag{E.13}$$

where we have used

$$\delta = \frac{\lambda}{\hbar\omega_0}\left(e^{(i\hbar\omega_0-\gamma/2)t}-1\right) \tag{E.14}$$

$$K_2 = \left|\delta\right|^2 = -\left|\frac{\lambda}{\hbar\omega_0}\right|^2\left(1+e^{-\gamma t}-2e^{-\gamma/2t}\cos(\omega_0 t)\right) \tag{E.15}$$

We are now ready to perform in an easy way the sum

$$C(t) = \langle X_H(t)X^\dagger(t=0)\rangle = \frac{e^{(K_1-K_2)/2}}{Z}\sum_{n=0}^{\infty} e^{-n\hbar\omega_0\beta}\langle n|e^{\delta^* a}e^{\delta a^\dagger}|n\rangle = \frac{e^{(K_1-K_2)/2}}{Z}\sum_{n=0}^{\infty} e^{-n\hbar\omega_0\beta}F_n \tag{E.16}$$

where $F_n = \langle n|e^{\delta^* a}e^{\delta a^\dagger}|n\rangle$. Taking the series expansion of the operators and performing the corresponding operations on the bra and ket's states we arrive to

$$F_n = \langle n|e^{\delta^* a}e^{\delta a^\dagger}|n\rangle = \sum_{i=0}^{\infty}\langle n+i|\frac{(-\delta^*)^i}{i!}\sqrt{\frac{n+i!}{n!}}\sum_{j=0}^{\infty}\frac{\delta^j}{j!}\sqrt{\frac{n+j!}{n!}}|n+j\rangle = \sum_{i=0}^{\infty}(-1)^i\frac{|\delta|^{2i}}{i!^2}\frac{(n+i)!}{n!} \tag{E.17}$$

substituing this result into the sum we obtain

$$C(t) = \frac{e^{(K_1-K_2)/2}}{Z}\sum_{n,i=0}^{\infty} e^{-n\beta\hbar\omega_0}(-1)^i\frac{|\delta|^{2i}(n+i)!}{i!^2 n!} \tag{E.18}$$

which is in fact easy to calculate knowing that

$$\frac{1}{(1-x)^{s+1}} = 1+(s+1)x+\frac{(s+1)(s+2)}{2!}x^2+\cdots = \sum_{n=0}^{\infty}\frac{(s+n)!}{s!n!}x^n \tag{E.19}$$

we obtain

$$C(t) = \frac{e^{(K_1-K_2)/2}}{Z}\sum_{i=0}^{\infty}\frac{1}{\left(1-e^{-\beta\hbar\omega_0}\right)^{i+1}}\frac{(-1)^i|\delta|^{2i}}{i!} = \frac{e^{(K_1-K_2)/2}}{Z\left(1-e^{-\beta\hbar\omega_0}\right)}\exp\left(-\frac{|\delta|^2}{1-e^{-\beta\hbar\omega_0}}\right) \tag{E.20}$$

yielding the final result

$$C(t) = \exp\left[\left(\frac{\lambda}{\hbar\omega_0}\right)^2\left(-ie^{-\gamma/2t}\sin(\omega_0 t)+\left(\frac{1}{2}-Z\right)\left(1+e^{-\gamma t}-2e^{-\gamma/2t}\cos(\omega_0 t)\right)\right)\right] \tag{E.21}$$

Finally, in the Liouvillian we use the Laplace transform of these correlation functions, namely

$$C_\epsilon = \int_0^\infty C(t')e^{i\epsilon t'} = \sum_{l,m,n=0}^{\infty}\frac{e^{\left(\frac{\lambda}{\omega}\left(\left(\frac{1}{2}-Z\right)\right)\right)^2}}{l!\;n!\;m!}\left(\frac{\lambda}{\omega}\right)^{l+m+n}\frac{\left(\frac{1}{2}-Z\right)^l(Z-1)^m Z^n}{z-i\epsilon+\gamma l-(-\gamma/2+i\omega)m+(\gamma/2+i\omega)n} \tag{E.22}$$

E.1.2 Negligible terms dropped in the derivation of the effective Liouvillian

The two following terms are negligible for different reasons. Although these terms are very similar to those which arise from eq. (4.28). However if we look carefuly, we will notice that the phases involved coming from different tunnels (p_{12} and p_{23}) have opposite signs for ϵ, that is, they have terms as $e^{i\epsilon(t-s)}$, as in the case of the terms arising from eq. (4.28). However, and here comes the difference, we notice that the sign behind τ is equal for both times giving rise to phases of the form $e^{i\tau(t+s)}$. Then, knowing that since these terms come by pairs of the form

$$\int_0^t ds \left(p_{12}(t)\rho(t)p_{23}(s)\langle X_s X_t^\dagger\rangle + p_{12}(s)\rho(t)p_{23}(t)\langle X_t X_s^\dagger\rangle \right), \tag{E.23}$$

the sum of these terms (after performing the intergal over time) is proportional to the tunnel interdot

$$\begin{aligned} & p_{12}\rho(t)p_{23}\sum_n J_n\left(\frac{-1}{-(i\omega_0+\gamma/2)n+i(\epsilon-\tau)}+\frac{-1}{(i\omega_0+\gamma/2)n-i(\epsilon+\tau)}\right) \\ & = p_{12}\rho(t)p_{23}\sum_n J_n\left(\frac{-2i\tau}{\left(-(i\omega_0+\gamma/2)n+i\epsilon\right)^2+\tau^2}\right), \end{aligned} \tag{E.24}$$

meaning that the contribution is negligible compared to the second order terms.

On the other hand, we assume negligible the terms coming from eq. (4.29) containing products of the same operators, such as

$$\mathrm{Tr}_{\mathrm{ph}}\left\{X_t p_{i,j}(t)\rho_e(0)\rho_B(0)p_{i,j}(s)X_s\right\} \tag{E.25}$$

have phases $e^{i(\epsilon+\tau)(t+s)}$, which are rotating very rapidly respect to the rest of the terms. For this reason, we apply the rotating wave approximation and we consider them negligible.

Apendix F

Decoherence of a superposition of coherent states coupled to a bath of oscillators

We consider the interference produced by a superposition of two coherent states in a harmonic oscillator [169]. Let us suppose that we initially prepare the system

$$|\Psi\rangle = |\alpha_1\rangle + |\alpha_2\rangle \tag{F.1}$$

where the states $|\alpha_i\rangle$ The density of states at time t is given by

$$\rho(t) = \sum_{i,j=1}^{2} |\alpha_i(t)\rangle\langle\alpha_j(t)|, \tag{F.2}$$

where $|\alpha(t)\rangle = e^{-i\omega t}|\alpha_i\rangle$.

Now, let us assume that the system is coupled to a bath of harmonic oscillators, which at the end of the day will lead to damping. This may be described by the hamiltonian

$$H = \hbar\omega a^\dagger a + a\Gamma^\dagger + a^\dagger\Gamma, \tag{F.3}$$

and leads to the known equatiation which describes the evolution of the reduced density operator

$$\frac{\partial\rho(t)}{\partial t} = \frac{\gamma}{2}\left(2a\rho(t)a^\dagger - a^\dagger a\rho(t) - \rho(t)a^\dagger a\right), \tag{F.4}$$

in the rotating wave approximation. We have used γ to denote the damping constant, as in the main text. The solution of $\rho(t)$ is given by

$$\rho(t)\sum_{n=0}^{\infty} N_t(m)\rho(0) \tag{F.5}$$

where $N_t(m)$ is the superoperator

$$N_t(m) = \int_0^t dt_m \int_0^{t_m} dt_{m-1}\cdots\int_0^{t_2} dt_1 S_{t-t_m} J S_{t_m-t_{m-1}} \times \cdots J S_{t_1}, \tag{F.6}$$

and

$$J\rho(t) = \gamma a \rho(t) a^\dagger \tag{F.7}$$

$$S_t\rho(t) = \exp\left[-\frac{\gamma t}{2}a^\dagger a\right]\rho(t)\exp\left[-\frac{\gamma t}{2}a^\dagger a\right]. \tag{F.8}$$

Then, using the property

$$e^{-\gamma a^\dagger a/2}|\alpha\rangle = \exp\left[-\frac{|\alpha|^2}{2}(1-e^{-\gamma t})\right]|\alpha e^{-\gamma t/2} \tag{F.9}$$

one can show

$$S_t|\alpha\rangle\langle\beta| = \exp\left[-\frac{|\alpha|^2}{2}(1-e^{-\gamma t/2}) - \frac{|\beta|^2}{2}(1-e^{-\gamma t/2})\right]|\alpha e^{-\gamma t/2}\rangle\langle\beta e^{-\gamma t/2}|. \tag{F.10}$$

The time developmment of an arbitrary initial element $|\alpha\rangle\langle\beta|$ is

$$(|\alpha\rangle\langle\beta|)_t = \exp\left[-\frac{|\alpha|^2}{2}(1-e^{-\gamma t/2}) - \frac{|\beta|^2}{2}(1-e^{-\gamma t/2})\right]|\alpha e^{-\gamma t/2}\rangle\langle\beta e^{-\gamma t/2}| \tag{F.11}$$

$$\times \sum_{m=0}^{\infty}(\gamma\alpha\beta^*)^m \int_0^t e^{-\gamma t_m}dt_m \int_0^{t_m} e^{-\gamma t_{m-1}}dt_{m-1}\cdots\int_0^{t_2} e^{-\gamma t_1}dt_1 \tag{F.12}$$

Using time ordering

$$(|\alpha\rangle\langle\beta|)_t = \exp\left[-\frac{|\alpha|^2}{2}(1-e^{-\gamma t/2}) - \frac{|\beta|^2}{2}(1-e^{-\gamma t/2})\right]|\alpha e^{-\gamma t/2}\rangle\langle\beta e^{-\gamma t/2}| \tag{F.13}$$

$$\times \sum_{m=0}^{\infty}\frac{(\gamma\alpha\beta^*)^m}{m!}\left[\int_0^t e^{-\gamma t'}dt'\right]^m = \langle\alpha|\beta\rangle^{1-e^{-\gamma t}}|\alpha e^{-\gamma t/2}\rangle\langle\beta e^{-\gamma t/2}| \tag{F.14}$$

Thus, for an initial density operator

$$\rho(0) = N\left(|\alpha\rangle\langle\alpha| + |\beta\rangle\langle\beta| + |\alpha\rangle\langle\beta| + |\beta\rangle\langle\alpha|\right) \tag{F.15}$$

Then applying the sueroperator N_t, one sees that the off-diagonal elements of the density matrix are dephased by the factor $\langle\alpha|\beta\rangle^{1-e^{\gamma t}}$. The greater the distance between the initial α and β coherent states, the more rapidly the off-diagonal elements are dephased. A physical explanation may be given by a consideration of the state of the coupled system plus environment before and after one quantum is lost from the system to the environment.

Apendix G

Dephasing produced biasing the phase by means of a noisy voltage

In the main text we have used the approximation of neglecting interference effects coming from having two or more non-adiabatic transitions [148]. In this appendix we justify this approximation and estimate the dephasing rate produced by biasing the phase difference by means of a fluctuating voltage. For the sake of simplicity we restrict the analysis to the infinite length 1D Josephson junction which in the pseudo-spin basis is given by

$$H = \frac{E_J}{2}\cos(\varphi/2)\sigma_z, \tag{G.1}$$

where σ_z denotes the z-Pauli matrix. As we have explained, the effect of fixing the current produces thermal fluctuations in the voltage, therefore fluctuations on the phase difference arise around some fixed value φ_0, namely $\varphi(t) = \varphi_0 + \delta\varphi(t)$. Then, we assume that these fluctuations are small compared with φ_0, so we can rewrite the Hamiltonian approximately

$$H \approx \frac{E_J}{2}\left(\cos(\varphi_0/2)\sigma_z - \delta\varphi(t)\sin(\varphi_0)\sigma_z\right). \tag{G.2}$$

Thus, the energy difference between the states fluctuates in time. In order to see the effects of these fluctuations one can take a coherent superposition such as

$$\frac{1}{\sqrt{2}}\left(|+\rangle + |-\rangle\right), \tag{G.3}$$

where $|\pm\rangle$ are the eigenstates of σ_z. The state at time t is given by

$$\frac{1}{\sqrt{2}}\left(e^{-i(\Delta t+\phi(t))}|+\rangle + e^{i(\Delta t+\phi(t))}|-\rangle\right). \tag{G.4}$$

Where we have used Δ to denote the constant energy difference between the states $|\pm\rangle$. The phase $\phi(t)$ accounts the time integral over the fluctuating component of the energy difference

$$\phi(t) = \frac{E_J\sin(\varphi_0)}{\hbar}\int_0^t d\tau\delta\varphi(\tau). \tag{G.5}$$

These fluctuations are seen in the expectation value

$$\langle\sigma_x\rangle(t) = \cos(\Delta t + \phi(t)). \tag{G.6}$$

Taking the average over the fluctuating phase we observe a decay of the oscillations

$$\langle\langle\sigma_x\rangle(t)\rangle = \cos(\Delta t)e^{-\frac{1}{2}\langle\phi(t)^2\rangle}. \tag{G.7}$$

where

$$\langle\phi(t)^2\rangle = \int_0^t dt_1 \int_0^t dt_2 \langle\delta\varphi(t_1)\delta\varphi(t_2)\rangle, \tag{G.8}$$

is the time integral of the autocorrelation function. Obtaining this integral allows us to determine lifetime of the coherences. In order to calculate it we have first to relate phase and voltage autocorrelation functions through the Josephson formula

$$\frac{d}{dt}\varphi(t) = \frac{2e}{\hbar}V. \tag{G.9}$$

So that we can express the phase correlation function in terms of the voltage correlation function can be written as

$$\langle\phi(t)^2\rangle = \left(\frac{2e}{\hbar}\right)^2 \int_0^t dt_1 \int_0^t dt_2 \int_0^{t_1} dt' \int_0^{t_2} dt'' \langle V(t')V(t'')\rangle. \tag{G.10}$$

Since the voltage fluctuations fulfill the Nyquist theorem, we can write

$$R = \frac{1}{k_B T}\int_{-\infty}^{\infty} \langle V(t)V(t+\tau)\rangle d\tau, \tag{G.11}$$

where T is the temperature that affects to the external circuit, and R is its corresponding resistance. Leading to the result

$$\langle\langle\sigma_x\rangle(t)\rangle = \cos(\Delta t)e^{-\frac{1}{2}\gamma_D t^3}, \tag{G.12}$$

where we have used

$$\gamma_D = \frac{1}{2}\left(\frac{E_J}{\hbar}\right)^2 \left(\frac{2e}{\hbar}\right)^2 R k_B T. \tag{G.13}$$

Due to the fact that the time needed to vary the phase by $\varphi \to \varphi + 2\pi$ is of the order of $1/\omega_{ac}$ and $\omega_{ac} = 10^{10}$Hz, and taking into account that for the parameters that we have considered (see caption of Fig. 3 in the main text) $\gamma_D/\omega_{ac}^3 \gg 1$, coherences become rapidly quenched.

Apendix H

Splitting of the Shapiro steps as a function of P_{LZ}

H.1 Fourier decomposition of the 4π-periodic current

The current that results of having LZT has the form of the continuous line shown in Fig. 7.3(b). However, from time to time the LZT does not occur, thus, the current suffers changes in its periodicity. The consequences of varying the periodicity of the current is reflected on the Shapiro steps pattern. It leads to the splitting of the steps see Fig 7.5. In order to have some analytical insight to this phenomena, we use a Fourier expansion of the current and of the non-LZT.

We begin calculating the Fourier components of the current when LZT are always given. We make an odd expansion leading to the terms

$$I_F(\varphi) = \sum_{n=0}^{\infty} b_n \sin\left(\frac{n}{2}\varphi\right) \tag{H.1}$$

where the Fourier components are given by

$$b_n = \frac{1}{\pi}\int_0^{2\pi} d\varphi I(\varphi)\mathrm{Sgn}\left[\cos(\varphi/2)\right]\sin\left(\frac{n}{2}\varphi\right), \tag{H.2}$$

here Sgn denotes the sign function and the current $I(\varphi)$ is given by

$$I(\varphi) = \frac{\partial}{\partial\varphi}E(\varphi) = \frac{E_J^2\sin(\varphi)}{8\sqrt{4\delta^2 + E_J^2\cos^2(\varphi/2)}}. \tag{H.3}$$

where δ is the overlap between the in-phase MF and E_J is the Josephson energy. The integral is zero for $n = \dot{2}$ yielding just the odd Fourier contributions. Taking into account that $\delta \ll E_J$, we take the first order (Taylor) expanssion in δ, yielding

$$b_0 = \frac{E_J}{4} - \frac{2\delta}{\pi} \tag{H.4}$$

$$b_n = (-1)^{n+1}\frac{2\delta}{\pi}. \tag{H.5}$$

This leads to write the current as,

$$I_F(\varphi) = \frac{E_J}{4}\sin(\varphi/2) + \frac{2\delta}{\pi}\sum_{n=0}^{\infty}(-1)^{n+1}\sin\left(\frac{2n+1}{2}\varphi\right). \tag{H.6}$$

As expected, the current has a 4π contribution proportional to E_J perturbed by a sum of extra terms which are of the order of δ.

H.1.1 Non-Landau Zener Transitions

We represent the phenomenon of not having LZT in a different way as it is presented in the main text. There, having a LZT was simulated by a change of sign. Indeed, this has been already included in the Fourier expansion above eq. H.6, and for this reason here having a non-LZT will be simulated by changing as well the sign of the current. To this aim we will use a unit-step that changes its sign after a certain period, which depends on the average of the LZ probability.

In the calculations we perform in the main text, this effect is estimated stochastically. In turn, here we consider the average of a given LZT and non-LZT. Since a LZT is not affected by a previous phase, this approximation will be in principle accurate. Thus, we consider the averaged LZ probability P_{LZ}, namely, in average after a number LZT there is a non-LZT. The next approximation will be to consider that these non-LZT are distributed homogenously in time. This approximation, is a bit more fragile, due to the fact that we are measuring the periodicity of the current by the position of the Shapiro steps. Thus, to consider a homogeneous distribution or an inhomogeneous one will lead to different results in the experiment. In principle, the homogeneous distribution will be only appropiated when the non-LZT are separated enough in time, so that the periodicity of the 4π current (eq. H.6) dominates.

In addition, the function has to include the fact that the change of sign can only come at certain values of the phase, i.e. when $\varphi = (2n+1)\pi$. Then, it is straightforward to obtain the period as

$$T = 2\pi(2P) \tag{H.7}$$

where

$$P = \text{Integer}\left[\frac{1}{1-P_{LZ}}\right] \tag{H.8}$$

and therefore the Fourier expansion becomes

$$\text{NLZ}(\varphi) = \sum_{i=0}^{\infty}\frac{4}{(2i+1)\pi}\sin\left(\frac{2i+1}{2P}(\varphi+\pi)\right) \tag{H.9}$$

H.1.2 Total current

Then, taking the product of the Fourier expansions of the current and the change of sign and we arrive to the expression

$$\begin{aligned} I(\varphi) = &\sum_{i=0}^{\infty}\frac{E_J}{2(2i+1)\pi}\left\{\cos\left(\left(\frac{1}{2}-\frac{2i+1}{2P}\right)\varphi\right) - \cos\left(\left(\frac{1}{2}+\frac{2i+1}{2P}\right)\varphi\right)\right\} \\ &+ \frac{\delta}{\pi}\sum_{i=0}^{\infty}\frac{4}{(2i+1)\pi}\sum_{n=0}^{\infty}\left\{(-1)^{n+1}\left[\cos\left(\left(\frac{2n+1}{2}-\frac{2i+1}{2P}\right)\varphi\right) - \cos\left(\left(\frac{2n+1}{2}+\frac{2i+1}{2P}\right)\varphi\right)\right]\right\}. \end{aligned} \tag{H.10}$$

We can observe that due to the new periodicity the former 4π and the rest of the Fourier components, are splitted in two by a quantity proportional to $2(1-P_{LZ})$, as occurs in the numerics (see Fig. 7.5). We can also see that the average model deviates from the stochastic calculations as we increase δ. This is caused because increasing δ, the number of non-LZT increases so that non-LZT may not occur isoletely, changing thus the periodicity. Therefore, for lower LZ probabilities the average between the pure 2π and 4π currents weighted by P_{LZ} give more accurate results.

It is worthy to remark that the Fourier current presented above, has been developed to show analyticaly the splitting, however, numerical results of the averaged model have been obtained from the current given by

$$I(\varphi) = I_M \frac{2}{E_J} \frac{\partial}{\partial \varphi} E(\varphi) \mathrm{S}gn\left\{\cos(\varphi/2)\right\} \mathrm{S}gn\left\{\cos\left(\frac{\varphi-(P-1)\pi}{2P}\right)\right\} \tag{H.11}$$

Bibliography

[1] A. R. Akhmerov, J. P. Dahlhaus, F. Hassler, M. Wimmer, and C. W. J. Beenakker. Quantized conductance at the majorana phase transition in a disordered superconducting wire. *Phys. Rev. Lett.*, 106:057001, 2011.

[2] Jason Alicea. New directions in the pursuit of majorana fermions in solid state systems. *Rep. Prog. Phys.*, 75:076501, 2012.

[3] A. D. Armour and A. MacKinnon. Transport via a quantum shuttle. *Phys. Rev. B*, 66:035333, 2002.

[4] L. G. Aslamazov and A. I. Larkin. Josephson effect in superconducting point contacts. *JETP*, 9:87, 1969.

[5] D. A. Bagrets and Yu. V. Nazarov. Full counting statistics of charge transfer in coulomb blockade systems. *Phys. Rev. B*, 67:085316, 2003.

[6] Marco Baiesi, Christian Maes, and Karel Netočný. Computation of current cumulants for small nonequilibrium systems. *J. Stat. Phys.*, 135:57, 2009.

[7] C. W. J. Beenakker. Search of majorana fermions in superconductors. *ArXiv*, 1112.1950, 2011.

[8] W. Belzig. Full counting statistics of super-poissonian shot noise in multilevel quantum dots. *Phys. Rev. B*, 71:161301(R), 2005.

[9] Colin Benjamin and Jiannis K. Pachos. Detecting majorana bound states. *Phys. Rev. B*, 81:085101, 2010.

[10] M. T. Björk, A. Fuhrer, A. E. Hansen, M. W. Larsson, L. E. Fröberg, and L. Samuelson. Tunable effective g factor in inas nanowire quantum dots. *Phys. Rev. B*, 72:201307, Nov 2005.

[11] R. H. Blick, R. J. Haug, J. Weis, D. Pfannkuche, K. von Klitzing, and K. Eberl. Single-electron tunneling through a double quantum dot: The artificial molecule. *Phys. Rev. B*, 53:7899, 1996.

[12] Karl Blum. *Density Matrix Theory and Applications*. Springer, New York, 2nd edition, 1996.

[13] C.J. Bolech and E. Demler. Observing Majorana bound states in p-wave superconductors using noise measurements in tunneling experiments. *Phys. Rev. Lett.*, 98:237002, 2007.

[14] Tobias Brandes. Coherent and collective quantum optical effects in mesoscopic systems. *Phys. Rep.*, 408:315, 2005.

[15] Tobias Brandes and Bernhard Kramer. Spontaneous emission of phonons by coupled quantum dots. *Phys. Rev. Lett.*, 83:3021, 1999.

[16] Tobias Brandes and Neil Lambert. Steering of a bosonic mode with a double quantum dot. *Phys. Rev. B*, 67:125323, 2003.

[17] H.-P. Breuer and F. Petruccione. *Theory of open quantum systems.* Oxford University Press, Oxford, 2003.

[18] Guido Burkard, Daniel Loss, and David P. DiVincenzo. Coupled quantum dots as quantum gates. *Phys. Rev. B*, 59:2070, 1999.

[19] Maria Busl, Rafael Sánchez, and Gloria Platero. Control of spin blockade by ac magnetic fields in triple quantum dots. *Phys. Rev. B*, 81:121306(R), 2010.

[20] A. O. Caldeira and A. J. Leggett. Influence of damping on quantum interference: An exactly soluble model. *Phys. Rev. A*, 31:1059, 1985.

[21] A. O. Caldeira and A. L. Leggett. Quantum tunnelling in a dissipative system. *Ann. Phys. (N.Y.)*, 149:374, 1983.

[22] Sébastien Camalet, Jörg Lehmann, Sigmund Kohler, and Peter Hänggi. Current noise in ac-driven nanoscale conductors. *Phys. Rev. Lett.*, 90:210602, 2003.

[23] H. J. Carmichael. *Statistical Methods in Quantum Optics.* Springer, Berlin, 1999.

[24] T.-P. Choy, J. M. Edge, A. R. Akhmerov, and C. W. J. Beenakker. Majorana fermions emerging from magnetic nanoparticles on a superconductor without spin-orbit coupling. *Phys. Rev. B*, 84:195442, 2011.

[25] Cohen-Tannoudji, B. Diu, and F. Laloë. *Quantum mechanics.* Wiley, New York, 1977.

[26] W. A. Coish, Daniel Loss, E. A. Yuzbashyan, and B. L. Altshuler. Quantum versus classical hyperfine-induced dynamics in a quantum dot. *J. App. Phys*, 101:081715, 2007.

[27] Charles E. Creffield and Gloria Platero. ac-driven localization in a two-electron quantum dot molecule. *Phys. Rev. B*, 65:113304, 2002.

[28] G. Cuniberti, G. Fagas, and K. Richter, editors. *Molecular Electronics.* Lecture Notes in Physics. Springer, Berlin, 2005.

[29] S. Datta and P. F. Bagwell. Can the bogoliubov-de gennes equation be interpreted as a one-particle equation? *Superlattices and Microstructures*, 25:051233, 1999.

[30] Rogerio de Sousa, Xuedong Hu, and S. Das Sarma. Effect of an inhomogeneous external magnetic field on a quantum-dot quantum computer. *Phys. Rev. A*, 64:042307, 2001.

[31] H. Dekker. Dynamics of the dissipative two-state system: the non-interacting-blip approximation. *Physica A*, 141:570, 1987.

[32] H. Dekker. Noninteracting-blip approximation for a two-level system coupled to a heat bath. *Phys. Rev. A*, 35:1436, 1987.

[33] Fernando Domínguez, Fabian Hassler, and Gloria Platero. On the dynamical detection of majorana fermions in current-biased nanowires. *ArXiv*, 1202.0642, 2012.

[34] Fernando Domínguez, Sigmund Kohler, and Gloria Platero. Phonon-mediated decoherence in triple quantum dots interferometers. *Phys. Rev. B*, 83:235319, 2011.

[35] Fernando Domínguez, Gloria Platero, and Sigmund Kohler. Electron bunching in triple quantum dots interferometers. *Chem. Phys.*, 375:284, 2010.

[36] James C. Ellenbogen and J. C. Love. Architectures for molecular electronic computers. *Proc. IEEE*, 88:386, 2000.

[37] C. Emary. Dark states in the magnetotransport through triple quantum dots. *Phys. Rev. B*, 76:245319, 2007.

[38] C. Emary, D. Marcos, R. Aguado, and T. Brandes. Frequency-dependent counting statistics in interacting nanoscale conductors. *Phys. Rev. B*, 76(16):161404, 2007.

[39] Sigurdur I. Erlingsson, Yuli V. Nazarov, and Vladimir I. Fal'ko. Nucleus-mediated spin-flip transitions in gaas quantum dots. *Phys. Rev. B*, 64:195306, 2001.

[40] U. Fano. Ionization yield of radiations. II. The fluctuations of the number of ions. *Phys. Rev.*, 72:26, 1947.

[41] C. Fasth, A. Fuhrer, M. T. Björk, and L. Samuelson. Tunable double quantum dots in inas nanowires defined by local gate electrodes. *Nano Lett.*, 5:1487, 2005.

[42] R. P. Feynman, R. B. Leighton, and M. Sands. *The Feynman Lectures on Physics*, volume 1. Addison Wesley, Reading MA, 1963.

[43] R. P. Feynman and F. L. Vernon. The theory of a general quantum system interacting with a linear dissipative system. *Ann. Phys. (N.Y.)*, 24:118, 1963.

[44] Richard P. Feynman. There's plenty of room at the bottom. *Eng. Sci.*, 23:22, 1960. Lecture given at the APS meeting 1959, see `http://www.its.caltech.edu/~feynman/plenty.html`.

[45] K. Flensberg. Tunneling characteristic of a chain of Majorana bound states. *Phys. Rev. B*, 82:180516(R), 2010.

[46] C. Flindt, C. Fricke, F. Hohls, T. Novotný, K. Netočný, T. Brandes, and R. J. Haug. Universal oscillations in counting statistics. *Proc. Natl. Acad. Sci. USA*, 106:10116, 2009.

[47] Christian Flindt, Tomás Novotný, Alessandro Braggio, and Antti-Pekka Jauho. Counting statistics of transport through coulomb blockade nanostructures: High-order cumulants and non-markovian effects. arXiv:1002.4506 [cond-mat].

[48] Christian Flindt, Tomás Novotný, Alessandro Braggio, Maura Sassetti, and Antti-Pekka Jauho. Counting statistics of non-markovian quantum stochastic processes. *Phys. Rev. Lett.*, 100:150601, 2008.

[49] Christian Flindt, Tomás Novotný, and Antti-Pekka Jauho. Current noise in a vibrating quantum dot array. *Phys. Rev. B*, 70:205334, 2004.

[50] L. Fu. Electron teleportation via Majorana bound states in a mesoscopic superconductor. *Phys. Rev. Lett.*, 104:056402, 2010.

[51] L. Fu and C. L. Kane. Superconducting proximity effect and majorana fermions at the surface of a topological insulators. *Phys. Rev. Lett.*, 100:096407, 2008.

[52] Liang Fu and C. L. Kane. Josephson current and noise at a superconductor quantum spin hall insulator fsuperconductor junction. *Phys. Rev. B*, 79:161408(R), 2009.

[53] T. A. Fulton and G. J. Dolan. Observation of single-electron charging effects in small tunnel junctions. *Phys. Rev. Lett.*, 59:109–112, Jul 1987.

[54] J. Gabelli and B. Reulet. Full counting statistics of avalanche transport: An experiment. *Phys. Rev. B*, 80:161203(R), 2009.

[55] C. W. Gardiner and P. Zoller. *Quantum Noise*. Springer, Berlin and Heidelberg, 3rd edition, 2004.

[56] L. Gaudreau, S. A. Studenikin, A. S. Sachrajda, P. Zawadzki, A. Kam, J. Lapointe, M. Korkusinski, and P. Hawrylak. Stability diagram of a few-electron triple dot. *Phys. Rev. Lett.*, 97:036807, 2006.

[57] M. C. Goorden, M. Thorwart, and M. Grifoni. Entanglement spectroscopy of a driven solid-state qubit and its detector. *Phys. Rev. Lett.*, 93:267005, 2004.

[58] H. Grabert and M. H. Devoret, editors. *Charge Tunneling Rates in Ultrasmall Junctions*, volume 294 of *NATO ASI Series B*. Plenum, New York, 1992.

[59] Frank Grossmann, Thomas Dittrich, Peter Jung, and Peter Hänggi. Coherent destruction of tunneling. *Phys. Rev. Lett.*, 67:516, 1991.

[60] S. A. Gurvitz and Ya. S. Prager. Microscopic derivation of rate equations for quantum transport. *Phys. Rev. B*, 53:15932, 1996.

[61] S. Gustavsson, M. Studer, R. Leturcq, T. Ihn, K. Ensslin, D. C. Driscoll, and A. C. Gossard. Frequency-selective single-photon detection using a double quantum dot. *Phys. Rev. Lett.*, 99:206804, 2007.

[62] Vincent Hakim and Vinay Ambegaokar. Quantum theory of a free particle interacting with a linearly dissipative environment. *Phys. Rev. A*, 32:423, 1985.

[63] Peter Hänggi, Mark Ratner, and Sophia Yaliraki. Special issue: Processes in molecular wires. *Chem. Phys.*, 281:111–502, 2002.

[64] Peter Hänggi, Peter Talkner, and Michal Borkovec. Reaction-rate theory: fifty years after kramers. *Rev. Mod. Phys.*, 62:251, 1990.

[65] A. E. Hansen, M. T. Björk, C. Fasth, C. Thelander, and L. Samuelson. Spin relaxation in inas nanowires studied by tunable weak antilocalization. *Phys. Rev. B*, 71:205328, May 2005.

[66] R. Hanson, L. P. Kouwenhoven, J. R. Petta, S. Tarucha, and L. M. K. Vandersypen. Spins in few-electron quantum dots. *Rev. Mod. Phys.*, 79:1217, 2007.

[67] R. A. Harris and R. Silbey. Variational calculation of the tunneling system interacting with a heat bath ii. dynamics of an asymmetric tunneling system. *J. Chem. Phys.*, 83:1069, 1985.

[68] T. Hatano, M. Stopa, and S. Tarucha. Single-electron delocalization in hybrid vertical-lateral double quantum dots. *Science*, 309:268, 2005.

[69] http://en.wikipedia.org/wiki/Double beta decay.

[70] Xuedong Hu, Rogerio de Sousa, and S. Das Sarma. Interplay between zeeman coupling and swap action in spin-based quantum computer models: Error correction in inhomogeneous magnetic fields. *Phys. Rev. Lett.*, 86:918, 2001.

[71] Jesús Iñarrea, C. Lopez-Monis, Allan H. MacDonald, and Gloria Platero. Hysteretic behavior in weakly coupled double-dot transport in the spin blockade regime. *Appl. Phys. Lett.*, 91:252112, 2007.

[72] Jesús Iñarrea, C. Lopez-Monis, and Gloria Platero. Tunable nuclear polarization with external stationary fields in weakly coupled double quantum dots. *Appl. Phys. Lett.*, 94:252106, 2009.

[73] Jesús Iñarrea, Gloria Platero, and Allan H. MacDonald. Electronic transport through a double quantum dot in the spin-blockade regime: Theoretical models. *Phys. Rev. B*, 76:085329, 2007.

[74] G.-L. Ingold and Yu. V. Nazarov. *Charge Tunneling Rates in Ultrasmall Junctions*, volume 294 of *NATO ASI Series B*, pages 21–107. Plenum, New York, 1992.

[75] P. A. Ioselevich and M. V. Feigel'man. Anomalous josephson current via Majorana bound states in topological insulators. *Phys. Rev. Lett.*, 106:077003, 2011.

[76] D. A. Ivanov. Non-abelian statistics of half-quantum vortices in p-wave superconductors. *Phys. Rev. Lett.*, 86:268–271, 2001.

[77] R. Jackiw and C. Rebbi. Solitons with fractional charge. *Phys. Rev. D*, 13:3398, 1976.

[78] Liang Jiang, David Pekker, Jason Alicea, Gil Refael, Yuval Oreg, and Felix von Oppen. Unconventional josephson signatures of majorana bound states. *Phys. Rev. Lett.*, 107:236401, 2011.

[79] A. C. Johnson, J. R. Petta, J. M. Taylor, A. Yacoby, M. D. Lukin, C. M. Marcus, M. P. Hanson, and A. C. Gossard. Tripletsinglet spin relaxation via nuclei in a double quantum dot. *Nature*, 435:925, 2005.

[80] Oleg N. Jouravlev and Yuli V. Nazarov. Electron transport in a double quantum dot governed by a nuclear magnetic field. *Phys. Rev. Lett.*, 96:176804, 2006.

[81] Franz J. Kaiser and Sigmund Kohler. Shot noise in non-adiabatically driven nanoscale conductors. *Ann. Phys. (Leipzig)*, 16:702, 2007.

[82] M. A. Kastner. Artificial atoms. *Physics Today*, 46:24, 1993.

[83] A. Khaetskii, D. Loss, and L. Glazman. Electron spin decoherence in quantum dots due to interaction with nuclei. *Phys. Rev. Lett.*, 88:186802, 2002.

[84] A. Khaetskii, D. Loss, and L. Glazman. Electron spin evolution induced by interaction with nuclei in a quantum dot. *Phys. Rev. B*, 67:195329s, 2003.

[85] A. Yu Kitaev. Unpaired majorana fermions in quantum wires. *Phys. Usp.*, 44:131, 2001.

[86] A. Yu Kitaev. Fault-tolerant quantum computation by anyons. *Ann. Phys.*, 303:2, 2003.

[87] J. Klinovaja and D. Loss. Composite majorana fermion wavefunctions in nanowires. *ArXiv*, 1205.7054v1, 2012.

[88] Jens Koch and Felix von Oppen. Franck-condon blockade and giant fano factors in transport through single molecules. *Phys. Rev. Lett.*, 94:206804, 2005.

[89] Sigmund Kohler, Jörg Lehmann, and Peter Hänggi. Driven transport on the nanoscale. *Phys. Rep.*, 406:379, 2005.

[90] F. H. L. Koppens, J. A. Folk, J. M. Elzerman, R. Hanson, L. H. Willems van Beveren, I. T. Vink, H. P. Tranitz, W. Wegscheider, L. P. Kouwenhoven, and L. M. K. Vandersypen. Control and detection of singlet-triplet mixing in a random nuclear field. *Science*, 309:1346, 2005.

[91] L. P. Kouwenhoven, D. G. Austing, and S. Tarucha. Few-electron quantum dots. *Rep. Prog. Phys.*, 64:701, 2001.

[92] L. P. Kouwenhoven, C. M. Marcus, P. L. McEuen, S. Tarucha, R. M. Westervelt, and N. S. Wingreen. *Electron Transport in Quantum Dots.* Proc. Nato ASI "Mesoscopic Electron Transport". Kluwer, Dordrecht, 1997.

[93] Mark Kvale, S. E. Hebboul, and J. C. Garland. Theory of even-odd step suppression in the rsj model. *Physica B*, 165:1585, 1990.

[94] H. J. Kwon, K. Sengupta, and V. M. Yakovenko. Fractional ac josephson effect in p- and d-wave superconductors. *Eur. Phys. J. B*, 37:349, 2004.

[95] K. T. Law and P. A. Lee. Robustness of Majorana fermion induced fractional josephson effect. *Phys. Rev. B*, 84:081304, 2011.

[96] K. T. Law, P. A. Lee, and T. K. Ng. Majorana fermion induced resonant andreev reflection. *Phys. Rev. Lett.*, 103:237001, 2009.

[97] A. J. Leggett, S. Chakravarty, A. T. Dorsey, M. P. A. Fisher, A. Garg, and W. Zwerger. Dynamics of the dissipative two-state system. *Rev. Mod. Phys.*, 59:1, 1987.

[98] Jörg Lehmann, Sébastien Camalet, Sigmund Kohler, and Peter Hänggi. Laser controlled molecular switches and transistors. *Chem. Phys. Lett.*, 368:282, 2003.

[99] M. Leijnse and K. Flensberg. Introduction to topological superconductivity and majorana fermions. *Arxiv*, 1206.1736, 2012.

[100] G. B. Lesovik and L. S. Levitov. Noise in an ac biased junction: Nonstationary aharonov-bohm effect. *Phys. Rev. Lett.*, 72:538, 1994.

[101] R. Leturcq, C. Stampfer, K. Inderbitzin, L. Durrer, C. Hierold, E. Mariani, M. G. Schultz, F. von Oppen, and K. Ensslin. Franck-condon blockade in suspended carbon nanotube quantum dots. *Nature Phys.*, 5:327, 2009.

[102] L. S. Levitov and M. Reznikov. Counting statistics of tunneling current. *Phys. Rev. B*, 70:115305, 2004.

[103] Feng Li, HuJun Jiao, JuYan Luo, Xin-Qi Li, and S.A. Gurvitz. Coulomb blockade double-dot aharonov-bohm interferometer: Giant fluctuations. *Physica E*, 41:1707, 2009.

[104] R. M. Lutchyn, J. D. Sau, and S. Das Sarma. Majorana fermions and a topological phase transition in semiconductor-superconductor heterostructures. *Phys. Rev. Lett.*, 105:077001, 2010.

[105] V. B. Magalinskiĭ. Dynamical model in the theory of the brownian motion. *Zh. Eksp. Teor. Fiz.*, 36:1942, 1959. [Sov. Phys. JETP **9**, 1381 (1959)].

[106] Gerald D. Mahan. *Many-Particle Physics*. Plenum Press, New York, 2nd edition, 1990.

[107] Ettore Majorana. Teoria simmetrica dell'elettrone e del positrone. *Nuovo Cimento*, 5:171, 1937.

[108] F. Marquardt and C. Bruder. Dephasing in sequential tunneling through a double-dot interferometer. *Phys. Rev. B*, 68:195305, 2003.

[109] I. A. Merkulov, A. Efros, and M. Rosen. Electron spin relaxation by nuclei in semiconductor quantum dots. *Phys. Rev. B*, 65:205309, 2002.

[110] B. Michaelis, C. Emary, and C. W. J. Beenakker. All-electronic coherent population trapping in quantum dots. *Europhys. Lett.*, 73:677, 2006.

[111] Gregory Moore and Nicholas Read. Nonabelions in the fractional quantum hall effect. *Nuc. Phys. B*, 360:362, 1991.

[112] M. Morillo and R. I. Cukier. Control of proton-transfer reactions with external fields. *J. Chem. Phys.*, 98:4548, 1993.

[113] V. Mourik, K. Zuo1, S. M. Frolov, S. R. Plissard, E. P. A. M. Bakkers, and L. P. Kouwenhoven. Signatures of majorana fermions in hybrid superconductor-semiconductor nanowire devices. *Science*, 336:1003, 2012.

[114] A. Nayak, S. H. Simon, A. Stern, M. Friedman, and S. Das Sarma. Non-abelian anyons and topological quantum computation. *Phys. Rev. Mod.*, 80:1083, 2008.

[115] J. Nilsson, A. R. Akhmerov, and C. W. J. Beenakker. Splitting of a cooper pair by a pair of Majorana bound states. *Phys. Rev. Lett.*, 101:120403, 2008.

[116] T. Novotný, Andrea Donarini, Christian Flindt, and Antti-Pekka Jauho. Shot noise of a quantum shuttle. *Phys. Rev. Lett.*, 92:248302, 2004.

[117] K. Ono, D. G. Austing, Y. Tokura, and S. Tarucha. Current rectification by pauli exclusion in a weakly coupled double quantum dot system. *Science*, 297:1313, 2002.

[118] Y. Oreg, G. Refael, and F. von Oppen. Helical liquids and Majorana bound states in quantum wires. *Phys. Rev. Lett.*, 105:177002, 2010.

[119] P. E. Parris and R. Silbey. Variational treatment of a harmonic oscillator coupled to a dissipative heat bath. *J. Chem. Phys.*, 86:6381, 1987.

[120] Elmar G. Petrov and Peter Hänggi. Nonlinear electron current through a short molecular wire. *Phys. Rev. Lett.*, 86:2862, 2001.

[121] J. R. Petta, A. C. Johnson, J. M. Taylor, E. A. Laird, A. Yacoby, M. D. Lukin, C. M. Marcus, M. P. Hanson, and A. C. Gossard. Coherent manipulation of coupled electron spins in semiconductor quantum dots. *Science*, 309:2180, 2005.

[122] A. Pfund, I. Shorubalko, K. Ensslin, and R. Leturcq. Suppression of spin relaxation in an inas nanowire double quantum dot. *Phys. Rev. Lett.*, 99:036801, 2007.

[123] D. I. Pikulin and Yuli V. Nazarov. Phenomenology and dynamics of Majorana josephson junction. *Arxiv*, 1112.6368, 2011.

[124] D. I. Pikulin and Yuli V. Nazarov. Topological properties of superconducting junctions. *JETP Lett.*, 94:752, 2011.

[125] Gloria Platero and Ramón Aguado. Photon-assisted transport in semiconductor nanostructures. *Phys. Rep.*, 395:1, 2004.

[126] Christina Pöltl, Clive Emary, and Tobias Brandes. Two-particle dark state in the transport through a triple quantum dot. *Phys. Rev. B*, 80:115313, 2009.

[127] A. C. Potter and P. A. Lee. Multichannel generalization of kitaev's Majorana end states and a practical route to realize them in thin films. *Phys. Rev. Lett.*, 105:227003, 2010.

[128] N. V. Prokof'ev and P. C. E. Stamp. Theory of the spin bath. *Rep. Prog. Phys.*, 63:669–726, 2000.

[129] N. Read and Dmitry Green. Paired states of fermions in two dimensions with breaking of parity and time-reversal symmetries and the fractional quantum hall effect. *Phys. Rev. B*, 61:10267, 2000.

[130] A. Relaño, J. Dukelsky, and R. A. Molina. Decoherence induced by an interacting spin environment in the transition from integrability to chaos. *Phys. Rev. E*, 76:046223, 2007.

[131] H. I. Jørgensen, K. Grove-Rasmussen, J. R. Hauptmann, and P. E.Lindelof. Single wall carbon nanotube double quantum dot. *Appl. Phys. Lett.*, 89:232113, 2006.

[132] J. G. Rodrigo, V. Crespo, H. Suderow, S. Vieira, and F. Guinea. Topological superconductivity in lead nanowires. *ArXiv*, 1203.5265v1, 2012.

[133] M. C. Rogge and R. J. Haug. Two-path transport measurements on a triple quantum dot. *Phys. Rev. B*, 77:193306, 2008.

[134] Leonid P. Rokhinson, Xinyu Liu, and Jacek K. Furdyna. Two-path transport measurements on a triple quantum dot. *ArXiv*, 1204.4212v1, 2012.

[135] P. Roulleau, S. Baer, T. Choi, F. Molitor, J. Güttinger, T. Müller, S. Dröscher, K. Ensslin, and T. Ihn. Coherent electron-phonon coupling in tailored quantum systems. *Nature Comm.*, 2:239, 2011.

[136] M. S. Rudner and L. S. Levitov. Self-polarization and dynamical cooling of nuclear spins in double quantum dots. *Phys. Rev. Lett.*, 99:036602, 2007.

[137] P. Russer. Influence of microwave radiation on curren-voltage characteristic of superconducting weak links. *J. App. Phys.*, 43:2008, 1972.

[138] Jun John Sakurai. *Modern Quantum Mechanics*. Addison-Wesley, Reading, 2nd edition, 1995.

[139] Pablo San-Jose, Elsa Prada, and Ramon Aguado. Ac josephson effect in finite-length nanowire junctions with Majorana modes. *Phys. Rev. Lett.*, 108:257001, 2012.

[140] Rafael Sánchez, Ernesto Cota, Ramón Aguado, and Gloria Platero. Spin-filtering through excited states in double-quantum-dot pumps. *Phys. Rev. B*, 74:035326, 2006.

[141] Rafael Sánchez, Sigmund Kohler, and Gloria Platero. Spin correlatoins in spin blockade. *New J. Phys.*, 10:115013, 2008.

[142] S. Sapmaz, C. Meyer, P. Beliczynski, P. Jarillo-Herrero, and L. P.Kouwenhoven. Excited state spectroscopy in carbon nanotube double quantum dots. *Nano Lett.*, 6:1350, 2006.

[143] Gernot Schaller, Gerold Kießlich, and Tobias Brandes. Transport statistics of interacting double dot systems: Coherent and non-markovian effects. *Phys. Rev. B*, 80:245107, 2009.

[144] D. Schröer, A. D. Greentree, L. Gaudreau, K. Eberl, L. C. L. Hollenberg, J. P. Kotthaus, and S. Ludwig. Electrostatically defined serial triple quantum dot charged with few electrons. *Phys. Rev. B*, 76:075306, 2007.

[145] J. H. F. Scott-Thomas, Stuart B. Field, M. A. Kastner, Henry I. Smith, and D. A. Antoniadis. Conductance oscillations periodic in the density of a one-dimensional electron gas. *Phys. Rev. Lett.*, 62:583, 1989.

[146] Jiushu Shao and Peter Hänggi. Decoherent dynamics of a two-level system coupled to a sea of spins. *Phys. Rev. Lett.*, 81(26):5710–5713, 1998.

[147] S. Shapiro. Josephson currents in superconducting tunneling: The effect of microwaves and other observations. *Phys. Rev. Lett.*, 11:80, 1963.

[148] S. N. Shevchenko, S. Ashhabb, and Franco Nori. Landau-Zener-Stückelberg interferometry. *Phys. Rep.*, 492:1, 2010.

[149] I. Shorubalko, A. Pfund, R. Leturcq, M. T. Borgström, F. Gramm, E. Möller, E. Gini, and K. Ensslin. Tunable few-electron quantum dots in inas nanowires. *Nanotech.*, 18:44014, 2007.

[150] R. Silbey and R. A. Harris. Variational calculation of the dynamics of a two level system interacting with a bath. *J. Chem. Phys.*, 80:2615, 1984.

[151] Charles P. Slichter. *Principles of Magnetic Resonance*, volume 1 of *Springer Series in Solid State Sciences*. Springer, Berlin, 3 edition, 1990.

[152] P. C. E. Stamp. Influence of paramagnetic and kondo impurities on macroscopic quantum tunneling in squid's. *Phys. Rev. Lett.*, 61:2905, 1988.

[153] P. C. E. Stamp. The decoherence puzzle. *Stud. Hist. Phil. Mod. Phys.*, 37:467, 2006.

[154] L. Sun, L. DiCarlo, M. D. Reed, G. Catelani, Lev S. Bishop, D. I. Schuster, B. R. Johnson, Ge A. Yang, L. I. Glazman L. Frunzio, M. H. Devoret, and R. J. Schoelkopf. Measurements of quasiparticle tunneling dynamics in a bandgap-engineered transmon qubit. *ArXiv*, 1112.2621, 2011.

[155] Yukio Tanaka, Takehito Yokoyama, and Naoto Nagaosa. Manipulation of the majorana fermion, andreev reflection, and josephson current on topological insulators. *Phys. Rev. Lett.*, 103:107002, 2009.

[156] E. D. Thompson. Perturbation theory for a resistivity shunted josephson element. *J. Appl. Phys.*, 44:5587, 1973.

[157] M. Thorwart, E. Paladino, and M. Grifoni. Dynamics of the spin-boson model with a structured environment. *Chem. Phys.*, 296:333, 2004.

[158] Michael Tinkham. *Introduction to superconductivity.* International series in pure and applied physics. McGraw-Hill, Inc, New York, 1996.

[159] Daniel Urban and Jürgen König. Tunable dynamical channel blockade in double-dot aharonov-bohm interferometers. *Phys. Rev. B*, 79:165319, 2009.

[160] Daniel Urban, Jürgen König, and Rosario Fazio. Coulomb-interaction effects in full counting statistics of a quantum-dot aharonov-bohm interferometer. *Phys. Rev. B*, 78:075318, 2008.

[161] N. C. van der Vaart, S. F. Godijn, Y. V. Nazarov, C. J. P. M. Harmans, and J. E. Mooij. Resonant tunneling through two discrete energy states. *Phys. Rev. Lett.*, 74:4702, 1995.

[162] W. G. van der Wiel, S. De Franceschi, J. M. Elzerman, T. Fujisawa, S. Tarucha, and L. P. Kouwenhoven. Electron transport through double quantum dots. *Rev. Mod. Phys.*, 75:1, 2003.

[163] B. van Heck, F. Hassler, A. R. Akhmerov, and C. W. J. Beenakker. Coulomb stability of the 4π-periodic josephson effect of Majorana fermions. *Phys. Rev. B*, 84:180502(R), 2011.

[164] N. G. van Kampen. *Stochastic processes in physics and chemistry.* North-Holland, Amsterdam, 1992.

[165] E. Vernek, C. A. Büsser, G. B. Martins, E. V. Anda, N. Sandler, and S. E. Ulloa. Kondo regime in triangular arrangements of quantum dots: Molecular orbitals, interference, and contact effects. *Phys. Rev. B*, 80:035119, 2009.

[166] Carmen Vierheilig, Johannes Hausinger, and Milena Grifoni. Dissipative dynamics of a qubit coupled to a nonlinear oscillator. *Phys. Rev. A*, 80:069901, 2009.

[167] G E Volovik. Fermion zero modes on vortices in chiral superconductors. *JETP Lett.*, 70:609, 1999.

[168] G E Volovik and V M Yakovenko. Fractional charge, spin and statistics of solitons in superfluid 3he film. *J. Phys.*, 1:5263, 1989.

[169] D. F. Walls and G. J. Milburn. Effect of dissipation on quantum coherence. *Phys. Rev. A*, 31:2403, 1985.

[170] C. Weber, A. Fuhrer, C. Fasth, G. Lindwall, L. Samuelson, and A. Wacker. Probing confined phonon modes by transport through a nanowire double quantum dot. *Phys. Rev. Lett.*, 104:036801, 2010.

[171] E. M. Weig, R. H. Blick, T. Brandes, J. Kirschbaum, W. Wegscheider, M. Bichler, and J. P. Kotthaus. Single-electron-phonon interaction in a suspended quantum dot phonon cavity. *Phys. Rev. Lett.*, 92:046804, 2004.

[172] F. K. Wilhelm, S. Kleff, and J. von Delft. The spin-boson model with a structured environment: a comparison of approaches. *Chem. Phys.*, 296:345, 2004.

[173] M. Wimmer, A. R. Akhmerov, J. P. Dahlhaus, and C. W. J. Beenakker. Quantum point contact as a probe of a topological superconductor. *New J. Phys.*, 13:053016, 2011.

[174] M. Wimmer, A. R. Akhmerov, M. V. Medvedyeva, J. Tworzydlo, and C. W. J. Beenakker. Majorana bound states without vortices in topological superconductors with electrostatic defects. *Phys. Rev. Lett.*, 105:046803, 2010.

[175] A.M. Zagoskin. *Quantum theory of Many Body Systems.* Springer, New York, 1998.

Conclusions

This thesis contains two differentiated parts; in the first part we study transport through triple and double quantum dots, while in the second part we analyze an experiment directly related with the existence of Majorana fermions.

In chapter 3 we have studied the current and the shot-noise of the electrons traveling through a triple quantum dot in a ring configuration when one of the dots is far away from resonance. In this regime, the shot noise properties are most interesting and strong electron bunching occurs. Thus, quantum dots in ring configuration may serve not only for the observation of interference effects, but also for the creation of currents with widely tunable super-Poissonian fluctuations.

Then, in chapter 4 we have studied the decoherence mechanism that a damped phonon mode exerts in the dark state. A qualitative understanding of these effects has been achieved by an analytical approximation after a polaron transformation leading to a reduced master equation for only the dot electrons. Within a standard treatment similar to the non-interacting blip approximation, we have obtained an effective master equation for the electron transport. Then it became possible to analytically obtain the current from the resulting master equation also close to destructive interference. The results agree well with the full numerical results, provided that the oscillator frequency is sufficiently large and the intra-dot tunneling is small. In turn, we can conclude that our reduced master equation faithfully describes transport effects entailed by a dissipative mode. Moreover, this picture provide evidence that the decoherence of an oscillator cat state directly turns into decoherence of the dark state.

In chapter 5 we have presented a microscopic model to describe the triplet-singlet and triplet-triplet transition probabilities mediated by the HF interaction in a DQD. We have stressed the importance of the local character and the nuclear flip-flop process of the HF interaction. These characteristics lead to a partial cancellation of the interference pattern, which can be intuitively seen by means of an analogy between the triplet-singlet transition and the double-slit experiment. With this picture in mind, we have shown the fundamental difference between the transition mediated by the hyperfine interaction and an anisotropic magnetic field. The transition under study turned out to be relevant in the spin blockade regime. The obtained results will serve as a basis to study transport accounting for the nuclear spin dynamical polarization and will open the possibility to explain experiments covering different tunneling coupling regimes.

In the second part of this thesis we have studied numerically the stability of the current-biased Shapiro step experiment. We have seen that the effects coming from the finiteness of the 1D system are dynamically decoupled driving the phase by means of an external current. We have calculated two different cases, when there are no extra 2π modes, i.e. $I_c = 0$, we have obtained that we can always determine the presence of the Majorana mode due to the appearance of steps at even multiples of the ac frequency ω_{ac} (see Fig. 7.4). In turn, when $I_c \gg I_M$, we have found that due to the non-linear effects coming from the dynamics of RSJ, the junction behaves 4π periodically for a range of voltages of the

order $I_M R$. We have found that it is possible to match this range, and therefore its 4π behavior, by using ac frequencies of the order of $\omega_{ac} \lesssim 2eRI_M/\hbar = 10^{10}$Hz (see Fig. 7.6). The resulting Shapiro steps are thus placed at even multiples of the frequency ω_{ac}. In addition, we have seen that the effects of QP on the current are negligible at the typical estimated timescales. From our results, we believe that performing the current-biased Shapiro experiment is a strong tool to prove the existence of Majorana fermions in finite nanowires.

Publications

1. F. Domínguez, F. Hassler and G. Platero, *On the Dynamical detection of Majorana fermions in current-biased nanowires*, ArXiv, **1202:0642**.

2. F. Domínguez, S. Kohler and G. Platero, *Phonon-mediated decoherence in triple quantum dot interferometers*, Phys. Rev. B, **83** , 235319 (2011).

3. F. Domínguez, G. Platero and S. Kohler, *Electron bunching in triple quantum dot interferometers*, Chem. Phys. **375**, 284 (2010).

4. F. Domínguez, G. Platero, *Hyperfine mediated triplet-singlet transition probability in a double-quantum-dot system: Analogy with the double-slit experiment* , Phys. Rev. B (R) **80**, 201301 (2009).

5. F. Domínguez, C. Esebbag, J. Dukelsky, *Solving the Richardson equations close to the critical points*, J. Phys. A **4**, 11349 (2006).